Spectroscopic characterization of optically trapped nanoparticles

Aashutosh Kumar

THÈSE

Pour obtenir le grade de

DOCTEUR DE L'UNIVERSITE GRENOBLE ALPES

Spécialité : NANOPHYSIQUE

Arrêté ministériel : 25 mai 2016

Présentée par

Aashutosh KUMAR

Thèse dirigée par **Jochen FICK,**

préparée au sein de l'**Institut Néel, CNRS**
dans **l'École Doctorale de Physique**

Caractérisation spectroscopique de nanoparticules piégées optiquement

Spectroscopic characterization of optically trapped nanoparticles

Thèse soutenue publiquement le **3 Novembre 2020**
devant le jury composé de :

Prof. Gérard COLAS DES FRANCS
Professeur, Université de Bourgogne, Dijon, Rapporteur

Dr. Francesco PEDACI
Chargé de Recherche, Centre de Biologie Structurale, CNRS, Montpellier, Rapporteur

Dr. Jean-Philippe POIZAT
Directeur de recherche, Institut Néel, CNRS, Grenoble, Président

Dr. Hervé GUILLOU
Maître de Conférences, Institut Néel, CNRS, Grenoble, Examinateur

"लहरों से डरकर नौका पार नहीं होती,
कोशिश करने वालों की कभी हार नहीं होती।"

(You cannot take your boat across the sea if you are afraid of the waves, the one who tries never fails.)

–Harivansh Rai Bachchan

In memory of my beloved father

Acknowledgement

I am grateful to Institut Néel, for providing me a wonderful platform for conducting my Ph.D. research in a great scientific environment. During my doctoral thesis coursework, I got a great opportunity to meet several scientists and researchers for discussing my ideas, curiosity, and research challenges. Without their kind support and encouragement, this work wouldn't have been possible.

First and foremost, I wish to dedicate my deepest gratitude to my supervisor Dr. Jochen Fick for his guidance and generous support during my doctoral studies at Institut Néel. I feel fortunate for doing my master's internship under his guidance and continuing further to my Ph.D. in Nano-optics and forces group. His supervision, deep knowledge, and experience have taught me the way to become an experimentalist and carry out a productive research by inspiring and stimulating my caliber. I appreciate him for his responsible character and availability in my training and very fruitful discussions. I have learned from him to be punctual in life as well as taking responsibility and initiative in work. I would always remember his saying that "you are doing science, so you have to always think about new ideas".

I also wish to express my appreciation to Prof. Síle Nic Chormaic from OIST Graduate University, Okinawa, Japan for her scientific advice and support during her sabbatical stay at Institut Néel. It has been my wonderful experience to share my office with a very inspiring and enthusiastic lady who taught me to do my best even when surrounded by difficulties. Never kneel to the problems.

I want to extend my gratitude to Gwénaëlle Julie for assisting me in the fabrication of optical fiber tips. I would like to thank Jean Francois Motte and Joel Balay for providing the equipments for my experimental setup. I also acknowledge my lab colleagues Rashmi, Umesh, Carlos, Baptiste, and Maxime for their discussions and cooperation on trapping experiments.

I am very thankful to my Nano-optics and forces group. Thanks to Serge Huant, Guillaume Bachelier, Aurélien Drezet, Olivier Arcizet, Benjamin Pigeau, and Herman Sellier for the scientific discussions and also for their sharing good humor during lunches. I also appreciate the company from doctoral and post-doc members from my group: Nicolas, Guillaume, Maeliss, Aline, Francesco, Antoine, and Philip.

I would also like to thank all the poles and services, administrative or technical from the Néel Institute. Thanks to Muriel, Florence, Elodie, Aurélie, and Yohan for their

help and availability for my administrative file work. I also extend my thanks to Patrick and Julien from the IT department for computer and software assistant, Cécile from the reprography department, Isabelle, Fabrice, and Nicolas from purchase store.

With utmost gratitude I would like to thank my defense committee members: Prof. Gérard Colas des Francs, Dr. Francesco Pedaci, Dr. Jean-Philippe Poizat, and Dr. Hervé Guillou for their interest in my doctoral dissertation and their thoughtful remarks and suggestions. I also extend the same gratitude for Dr. Géraldine Dantelle (CSI committee member) for her solicitous remarks and advice in Ph.D. studies.

Also, my doctoral thesis is a part of the national research project "SPECTRA" which has been very fruitful for my research perspectives. It has allowed me to meet many researchers involved in this collaborative project and sharing my experimental results, thoughts, and suggestions. I thank Prof. Thierry Gacoin, Khalil Lahlil, Jong-Wook Kim, Jeongmo Kim, Yannis Cheref from Laboratoire de Physique de la Matière Condensée (PMC), Palaiseau for providing me nanoparticles for the experimental measurements and followed by nice productive discussions. I also thank Prof. Gérard Colas des Francs, Aymeric Leray, and Reinaldo A. Chacon from Laboratoire Interdisciplinaire Carnot de Bourgogne, Dijon for their availability and theoretical discussions in project meetings.

I also had the chance to work with international collaborators and sharing the fruitful results. Thanks to Prof. Harald Giessen and Dr. Asa Asadollahbaik from the University of Stuttgart, Germany, for providing 3D printed fibers and discussions for experiments and interpretation. I extend my thanks to Samir K. Mondal from CSIO, Chandigarh, India, for his collaboration to provide us the axicon fibers.

I wish to thank my office mate Hugo and Philippe for providing a friendly environment and having nice discussions of science and politics. I would also like to thank Nitika and Vivek for the gossips and for sharing lunch. I thank my other colleagues too for sharing a wonderful memory at Institut Néel.

I extend my heartiest thanks to Prof. Claude Leroy, Université de Bourgogne for his guidance and suggestions during my master's and doctoral studies. I appreciate his politeness and generosity to his students. Being a foreigner, I feel very lucky to have such a great mentor.

I feel fortunate to find Indian friends in a foreign land, those who made my Grenoble life cherished and memorable. I would like to particularly thank Preeti and Siddhartha for inspiring and helping me to get out of the depression box when my experiments were not working properly. I am thankful to Akanksha, Akshay, and Sameer for correcting my thesis and listening to my defense presentations and having appropriate remarks which really helped me in my Ph.D. defense. I also extend my appreciation to Mahendra, Amit, Shweta, Vikas, Sandeep, and Saransh for a memorable company and joyful life in Grenoble.

Back in India, I wish to express my heartfelt gratitude to my mentors Prof. N. Satyanarayana, Dr. Alok Sharan, and Prof. Nalini J. Thumpi for their suggestions and for enlightening my career. I also would like to thank my friends, Parmeet, Abhay, and Kamalesh for their motivation and discussions in my tough days.

Finally, I express my deep appreciation to my family members for their blessings and unconditional love. I have succeeded in my life because of their guidance, dedication, and trust. I really don't know how to say thank to my mother and Papa for their inspiration and wholehearted support, any words will be remain insufficient. Especially for Papa, even though he is no more now with us but he will be always remain my legend. I also wish to appreciate the efforts and dedication of my brothers and sisters for making my life beautiful and memorable. At last, I would like to thank Shradha, my fiance for her immense support and adorning my life.

Contents

General introduction

Optical tweezers are a standard and non-invasive technique, in which a laser beam is employed for trapping or manipulating a microscopic particle or molecule without any mechanical contact. Since its introduction by Ashkin (1986) [1], it has been established as a powerful and precise technique in scientific measurements for its applications in physics, chemistry, biology, and atmospheric sciences.

This technique allows tweezing the particles by exploiting a small optical force, typically in the pico or femtonewton range, resulting from an interaction between light and matter. Based on the dipolar approximation, the optical force experienced by a trapped particle can be seen as the sum of two forces: scattering and gradient forces. The first one pushes the particle in the direction of light propagation while the second one attracts the particle towards a region of high intensity along the beam gradient. Thus, to create a stable optical trap, a higher gradient force is required compared to the scattering force. In conventional optical tweezers, an optical trap can be produced by exerting a tightly focused laser beam through a high numerical aperture microscope objective. The optical force experienced by trapped particles is proportional to the applied light power. A light beam with a very high light power can generate a very high trapping effect. In contrast, the use of highly intense light can lead to thermal heating of the trapped particles and can also lead to thermal convection of the trapping medium. In the case of biological specimens, it can destroy their identity. Thus, it is a challenge to enhance the trapping stability by increasing gradient force and reducing the scattering force with low light power.

The recent technological advancements in optical tweezers have improved trapping performances, precision, and integration of other experimental tools such as microfluidic channels, fluorescent microscopy, and spectroscopy. Nowadays, a wide range of microscope-integrated optical tweezers are commercially available in the market. These tweezers have been widely implemented to study nanoparticles, quantum dots, biological specimens such as living cells in biophysics. Also, the scientific community is using this technique to explore various fundamental research activities due to their non-destructive and non-invasive features.

The fiber optics technology has attracted optical tweezers scientific community's attention due to the efficient mode for light transmission. The implementation of fiber optics has miniaturized conventional tweezers' scale and provided a compact structure and flexibility to realize the particle trapping easily. The fibered optical tweezers do not

require a bulky or expensive microscope objective. The use of micro or nanostructured optical fibers allows transforming the light beam configuration from fundamental mode to advance modes very easily. For this application, the structured fibers can be designed and fabricated to allow transforming the fundamental Gaussian beam, guided mode into complex beams, e.g., Laguerre-Gaussian (LG) beams, quasi-Bessel beams, or optical vortexes. Also, an optical element or a microlens can be deposited on the fiber end, allowing converging the light beams to a focal point for particle trapping.

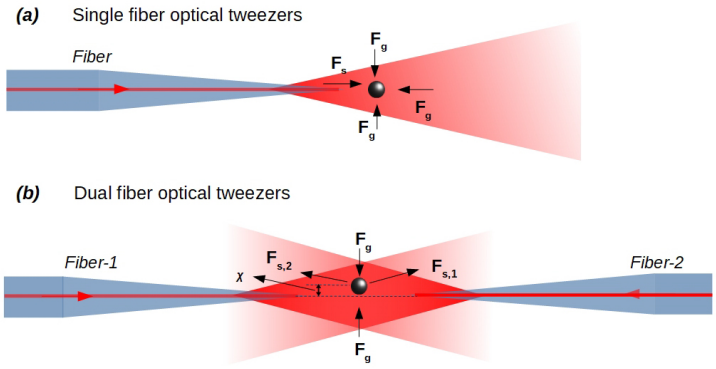

Figure 1: Schemes of fibered optical tweezers with two geometries, namely, (a) single fiber and (b) dual fibers geometries for tweezing a particle.

Our recent research activities at Institut Néel are focused on the optical trapping using the fibered optical tweezers. Our group has demonstrated the optical trapping of dielectric particles in suspension, using two nanostructured fibers tips [2], [3]. There are two ways to realize the particle trapping using fibered tweezers; single and dual fibers geometries (Figure 1). A single fiber geometry uses a similar technique as of the conventional optical tweezers for trapping a particle. In case of our tweezers setup, we use a tapered fiber tip which produce a diverging light beam, and it allows trapping of a particle near to fiber contact or a few micrometers away from the tip at the region of maximum intensity. In dual fibers geometry of two tapered fiber tips, the counter-propagating beams balance their radiation pressure at an equilibrium position, enabling a stable and efficient optical trap at relatively low intensities. Moreover, we have also integrated a spectroscopic technique to our experimental setup that allows characterizing the photoluminescence emission of optically trapped luminescent nanoparticles [4].

This Ph.D. thesis is a part of the ANR project “SpecTra” in collaboration with the T. Gacoin’s group from Laboratoire de Physique de la Matière Condensée (PMC) of Ecole Polytechnique, Palaiseau for nanoparticle elaboration and spectroscopic investigations and the G. Colas des Francs’s group from Laboratoire Interdisciplinaire Carnot de Bourgogne (ICB) of Université de Bourgogne for complementary trapping, spectroscopic studies, and theoretical support. The main objective of this thesis is the spectroscopic investigation of optically trapped luminescent nanoparticles and trapping of plasmonic oxides nanoparticles. These experimental characterizations have been proposed to be performed in water (suspension) and air. These objectives motivate us to develop a new fibered optical tweezers setup dedicated to particle trapping in air. We have also considered enhancing the trapping efficiency of existing tweezers setup using the 3D printed lens fibers, which have been developed in collaboration with the H. Giessen’s group from

4^{th} Physics Institute, University of Stuttgart, Germany. In collaboration with S. Mondal's group from Central Scientific Instruments Organisation, Chandigarh, India, we have developed and investigated optical trapping with non-Gaussiens beams fibers.

In this thesis work, we have dedicated a significant effort to develop a fibered tweezers setup for the optical trapping of nanoparticles in air. In early stage of experimental development, we have first studied the optical manipulation of water droplets and later, the microparticles. Further, we have considered improving the optical trapping approach in suspension tweezers using two different 3D printed lens fibers; Fresnel lens fibers and TIR-probe fiber. The Fresnel lens fibers have allowed an extremely stable optical trap for particles in counter-propagating geometry, while TIR-probe shows its great potential to produce an optical trap in single fiber geometry.

With our fiber tweezers application, we have studied optical trapping of Eu^{3+}-doped $NaYF_4$ nanorods. The paramount interest of these trapping measurements is to study the anisotropic PL feature of Eu^{3+} using the fluorescent spectroscopy, which has been made possible by integrating a spectrometer to the experimental setup. These measurements are facilitated using the tapered fiber tip and Fresnel lens fibers. In this series, we use these tweezers for characterizing a new type of particles called plasmonic oxide or Cs_xWO_3 nanoparticles, which are being developed for biosensing and photothermal application.

The experimental work carried out in this thesis is organized into four chapters:

- In chapter 1, we will briefly introduce the concept of the optical trapping technique. First, we will present a concise history of optical tweezers. Afterward, we will briefly describe the optical trapping principles, followed by the discussion of the optical forces using the theoretical models. Further, we will highlight the recent developments in optical trapping techniques and their applications, including the fibered optical tweezers. Finally, we will conclude this chapter by describing the approach of our experimental studies.

- In chapter 2, we will introduce our two distinct experimental tweezers setups and trapping analysis techniques. First, we will present a short description of an optical tweezers setup dedicated to trapping in air. We will then introduce the working process of suspension tweezers and the spectroscopic technique that allows measuring the emission properties of trapped particles. Afterward, we will introduce the micro and nanostructured optical fibers used for the experimental measurements. Finally, we will discuss our data analysis techniques for characterizing the optical trap. In this context, we will discuss the two different complementary methods to quantify the optical trap.

- Chapter 3 will focus on the optical manipulation experiments that have been carried out using the air-tweezers setup. First, we will discuss the manipulation of aerosol droplets by a diverging beam of a tapered fiber tip, and later, the manipulation of the polystyrene particles with the same tip. Further, we will present the experimental measurements observed using the negative axicon and positive axicon fibers. Finally, we will discuss a numerical simulation performed to understand

the experimental measurements obtained using this setup.

- In Chapter 4, we will present the optical trapping of dielectric particles, which is performed using the suspension tweezers. This chapter will be presented in three parts based on the used particles. In the first part, we will present the trapping of polystyrene particles using Fresnel lens fibers and a TIR-probe fiber. In a further part, we will discuss the optical trapping and spectroscopy of Eu^{3+} doped $NaYF_4$ nanorods implementing the tapered fiber tip and Fresnel lens fibers. Finally, we will discuss the optical trapping of plasmonic oxides nanoparticles using the Fresnel lens fibers.

Chapter 1

Introduction to optical trapping

Introduction

In this chapter, we will present a brief introduction of optical tweezers. First, we will discuss the historical development of optical trapping, including how to build an optical tweezers. Further, the fundamentals of optical forces involved in trapping will be discussed. Finally, we will present the state of the art on optical tweezers, which includes the different optical trapping approaches.

1.1 Fundamental

1.1.1 History

The mystery of light has consistently been a global fascination for scientific research and developments, leading to the invention of various optical devices and experimental techniques by discovering extraordinary ideas. For example, today, we are able to observe a world beyond the visual limitations of humans, thanks to the great discovery of the microscopy technique during the 17^{th} century. It has indeed been one of the finest inventions ever in optical sciences.

The roadmap of optical trapping started early in 17^{th} century, from a German astronomer J. Kepler's explanation of comet tails formation due to the solar radiation pressure [5]. Two centuries later, in 1862, J. C. Maxwell formulated the electromagnetic theory of light and suggested that light could exert a radiation pressure [5]. In the 1960s, the invention of laser was considered as a significant breakthrough that allowed accessing a coherent light beam for several investigations, including light-matter interactions [6]. In particular, the laser made it possible to use the presence of light for tweezing a microscopic object without any mechanical contact.

A. Ashkin first observed this event in 1970s by accelerating freely suspended, mi-

croparticles in water and gas using the laser radiation pressure (Figure 1.1 (a)) [7]. He accurately described the optical forces experienced by a particle in terms of a scattering force in the forward direction and a gradient force towards the beam waist. In the same experiment, he also demonstrated the first three dimensional optical trapping using the counter–propagating beams of two diverging laser, so that their radiation pressure cancelled each other (Figure 1.1 (b)).

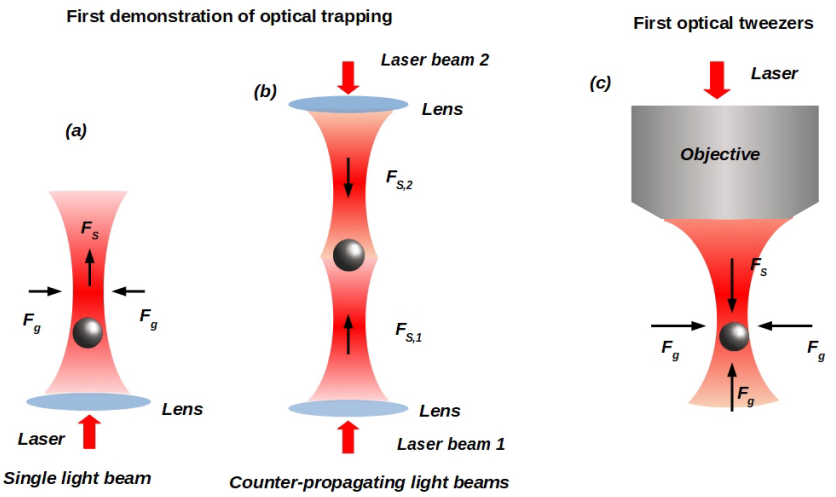

Figure 1.1: Schematics of early optical manipulation experiments for microparticle levitation using (a) single and (b) counter-propagating light beam. (c) A scheme of optical tweezers. These schematics are inspired by the reported works of Ashkin [1], [7]. F_s represent the scattering force and F_g is the gradient force.

In the consecutive years, Ashkin et al. implemented this tweezing technique for levitating the airborne particles vertically against the gravitational force[8]. In 1986, his team demonstrated optical trapping using a laser beam tightly focused by a microscope objective lens having a high numerical aperture (N.A.) and demonstrated stable trapping of dielectric particles (10-25 μm) in water [1]. This work was the first introduction of optical tweezers and later used as a reference for the scientific community working in this field (Figure 1.1 (c)). We have referred to the presented optical tweezers approach, as the classical or beam focusing approach. A year later, his team reported the first non-invasive trapping of biological objects such as bacteria, viruses, and cells with a green argon-ion laser and an Nd:YAG laser [9]. For his extraordinary work, he was thus rewarded the Nobel Prize in 2018.

1.1.2 How to realize stable optical trapping

From the above mentioned work, we have learned how to produce optical tweezers by focusing a light beam to a minimum beam spot using a high N.A. objective lens [10]. It is straightforward to build an optical tweezers setup by following previously demonstrated works [11]–[14]. A simple optical tweezers setup can be build without using any expensive instruments. For building such a setup, we require a laser source, a white light

source, an objective lens, a camera for image acquisition, a few optical elements for beam shaping, a translation stage to place sample volume, and trapping objects (samples). The objective lens should be a multi-element lens (aberration-corrected) with a high N.A. It is used for two different purposes: first to enable an optical trap by focusing the light beam to diffraction-limited spot and, secondly, making a resolved image of the microscopic samples.

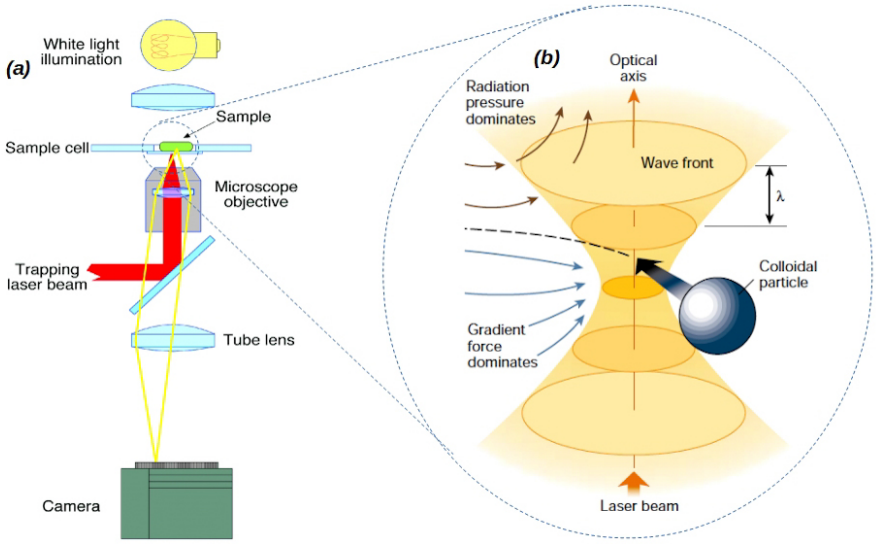

Figure 1.2: (a) A schematic illustration for building an optical tweezers setup [11]. (b) A particle is stably trapped by focused beam at focal point of the microscope objective [12].

Firstly, the objective lens should be focused on the sample chamber to visualize particles moving randomly within the chamber. The white light source should be aligned to produce the scattered light on the camera for imaging. The laser source must be aligned parallel to the axis of the objective lens using the optical elements. This procedure allows observing the trapping events (Figure 1.2 (a)).

The tightly focused light beam produces an optical trap near the beam waist. Due to the influence of light beam, the particles experience a repulsive force, also known as the scattering force, which pushes them in the direction of light beam propagation. At the same time, they also experience a gradient force, which attracts them towards the beam waist where light has a maximum field gradient. Thus, the particles get trapped slightly above the beam waist (Figure 1.2 (b)), and the total optical force experienced by them can be seen as the sum of these two forces (which we will be discuss later in this chapter). The following points influence the stable optical trapping of a particle:

- The gradient force must be higher than the scattering force.
- The trapping objects must have a higher refractive index than the surrounding medium.
- It requires an adequate light power depending on the trapped sample. The excess power may damage the sample's identity, or it may lead to thermal fluctuation by heating effects and convection.

- The laser should be chosen according to the sample of optical trapping, e.g., biological samples are sensitive to UV light, and can be damaged by absorption of light.

1.2 Theory of optical force

The principle of optical tweezers is based on the conservation of momentum and energy of the electromagnetic waves [13]. The light wave, which is considered as an electromagnetic wave, is composed of photons. The photons are also known as quanta of light and are considered as massless particles. They are carriers of the electromagnetic energy, which carries the light energy ($u = hc/\lambda$, where h is the Planck's constant, λ is the light wavelength, and c is the light speed in vacuum) with a momentum ($p = h/\lambda$). When an electromagnetic wave interacts or strikes with a dielectric particle or object, it gets scattered or transmitted (absorbed in case of absorptive particles) by the particle [15]. Any change in the direction of light propagation caused by scattering leads to change its momentum. According to Newton's third law of force, this process leads to equal and opposite momentum exchange between photons and the particle. This exchange results in an optical force that acts on the particle [11].

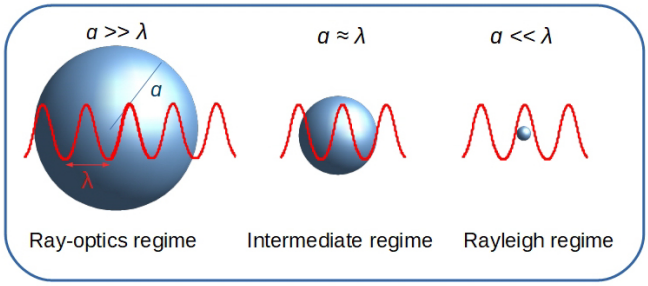

Figure 1.3: Schematic illustration of the particle size compared with the wavelength of laser (λ). (i) Mie regime (ray-optics), (ii) intermediate regime, and (iii) Rayleigh regime.

The optical force acting on the particles can be described using two well-developed models depending the validity of regimes based on the particle's size. (Figure 1.3) [10]. These two models are Mie scattering regime and Rayleigh regimes. If the particle size is significantly larger than the wavelength ($a >> \lambda$), the forces are accounted using Mie scattering (ray-optics) regimes, while Rayleigh regime accounts for significantly smaller size particles compared to wave wavelength ($a << \lambda$). Besides these two models, an intermediate regime, which is a theoretical model, is used for the exact calculation of optical force based on the electromagnetic theory of light (Figure 1.3) [16]. This regime considers a particle size equivalent to the used trapping wavelength ($a \approx \lambda$).

1.2.1 Ray-optic regime

A brief description of optical force in the ray optics regime can be presented for the large particle size using ref [13]. In this regime, the particle scattering becomes independent of the incident wavelength. It provides optical force calculation considering incident beam composition of individual rays carrying a certain light power ($P = N \cdot u$, where N is number of photons per second and u is photon energy).

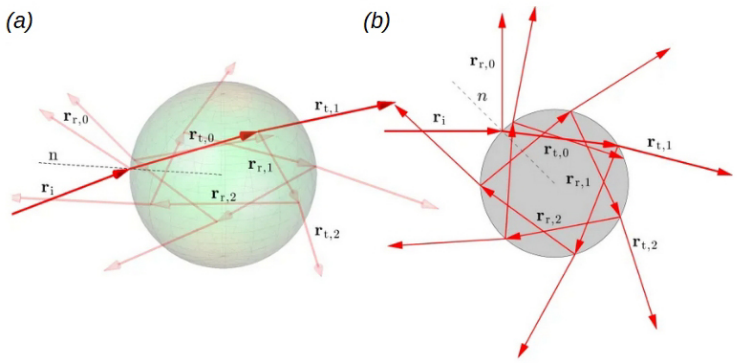

Figure 1.4: A scheme which describe the multiple scattering of beam through a sphere. The reflection and transmission of light beam in a (a) 3D view and (b) in the incidence plane [13].

Considering a transparent spherical particle of the higher refractive index than the suspending medium has been placed near a tightly focused light beam (Figure 1.4). When the light beam incidents on the particle, a small amount of incident light gets partly reflected, while remaining transmits inside the particle. The transmitted light reaches the other opposite surface of the particle transmitting from inside to outside the spherical surface.

Due to this incident light, a momentum exchange takes place between light and the particle. The total change of momentum per unit time is given by $-nN\mathbf{p} = (P/u)(h/\lambda) = -nP/c$. Using Newton's third law, the optical force for the reflected ray by the surface is given by $\mathbf{F}_r = nP/c$. This reflected ray undergoes another scattering at the boundary of the sphere. This process continues until all rays get escaped from the spherical surface. For each scattering event, the total optical force acted on the particle can be calculated as [17],

$$\mathbf{F}_{ray} = \left(\frac{n_i P_i}{c}\right)\hat{\mathbf{r}}_i - \left(\frac{n_r P_r}{c}\right)\hat{\mathbf{r}}_{r,0} - \sum_{n=1}^{+\infty} \frac{n_t P_t}{c}\hat{\mathbf{r}}_{t,0} \tag{1.1}$$

Here $\hat{\mathbf{r}}_i$, $\hat{\mathbf{r}}_r$ and $\hat{\mathbf{r}}_t$ are unit vectors which represents the direction of the incident, reflected and transmitted light ray, respectively. In particular, the incidence light on the sphere produces the two effects: pushes the particle into the direction of the light beam and pulls back the particle at the area of highest intensity in the direction perpendicular to the light. The optical force accounts for pushing the particle in the axial direction, known as the scattering force. The other attractive force which pulls back the particle into the optical trap is known as gradient force. Hence, the total optical force can be represented

as,

$$\mathbf{F}_{\text{ray}} = \mathbf{F}_{\text{ray,s}} + \mathbf{F}_{\text{ray,g}} \tag{1.2}$$

This regime is useful to understand the optical tweezers and found appropriate for the qualitative optical force.

1.2.2 Rayleigh regime

This regime is also known as dipolar approximation in which a trapped particle is treated as a point-like dipole. This model discusses the interaction of the electromagnetic field with the dipole. For discussing this regime, we have followed these refs. [5], [10], [16].

When the light beam is exerted on the particle, it induces a local polarization. This induced polarization gives rise to a current on which the electromagnetic field is acting through the Lorentz force. The Lorentz force acting on the particle can be calculated as [16],

$$\langle \mathbf{f} \rangle = \frac{1}{2} \Re\mathfrak{e}[(\mathbf{P} \cdot \nabla)\mathbf{E}^* + \partial_t \mathbf{P} \times \mu_0 \mathbf{H}^*] \tag{1.3}$$

where, $\mathbf{P}$ ($= (\epsilon_n - \epsilon_h)\mathbf{E}$, where, ϵ_n and ϵ_h are the permittivity of particle and host medium and $\mathbf{E}$ is the external electric field of the light beam) is the relative polarization which induced in particle with respect to host medium. Now introducing the Rayleigh scattering effect on this particle, an induced microscopic polarizability can be calculated which depends on the incident field. In this case the induced polarization can be defined as as $\mathbf{p} = \epsilon_n \epsilon_h \alpha \mathbf{E}$ using the term atomic polarizability (α). The α can be deduce using the relation [16],

$$\alpha = \frac{\alpha_0}{1 - ik^3\alpha_0/(6\pi)} \tag{1.4}$$

where α_0 is the polarizability considered as the radiative correction of particle and k ($= k_0 n_h = 2\pi n_h/\ \lambda$, where n_h refractive index of host medium, k_0 is wavenumber in vacuum) is wavenumber. The α_0 can be deduced using the Clausius–Mossotti relation for a dielectric spherical particle having size a,

$$\alpha_0 = 4\pi a^3 \frac{\epsilon_n - \epsilon_h}{\epsilon_n + 2\epsilon_h} \tag{1.5}$$

A more general expression called Rayleigh force formula can be obtained in terms of the electric field using the induced polarizability for the restriction of a slowly varying amplitude by deducing the eq. 1.3. Also, introducing the vector calculus identity for the electric field $(\nabla \cdot \mathbf{E})\mathbf{E}^* = \frac{1}{2}\nabla(\mathbf{E} \cdot \mathbf{E}^*) + \mathbf{E} \times (\nabla \times \mathbf{E})$ and the Maxwell's equation $\nabla \times \mathbf{E} = -\mu_0 \partial_t \mathbf{H}$, the eq. 1.3 can be written as

$$\langle \mathbf{F_i} \rangle_{Rayleigh} = \frac{\epsilon_n \epsilon_h}{2} \Re\mathfrak{e}(\alpha E_j \partial_i E_j^*) \tag{1.6}$$

The complex polarizability originates due to dephasing of nanorods dipole oscillation (after absorption of incident field) with respect to oscillating incident field. In this scenario the microscopic polarizability becomes important and considering it for the $\alpha = \alpha' + i\alpha''$.

The Rayleigh force be can directly from eq. 1.6 can be expressed as [16],

$$\langle \mathbf{F_i} \rangle_{Rayleigh} = \frac{\epsilon_n \epsilon_h \alpha'}{4} \partial_i (E_j E_j^*) + \frac{\epsilon_n \epsilon_h \alpha''}{2} \mathfrak{Im}(E_j \partial_i E_j^*) \tag{1.7}$$

Thus, this optical force experience by the dielectric particle can be separated into the two components: gradient and scattering force. The first term in eq. 1.7 corresponds to the gradient force, which is a purely real component and hence known as a conservative force. It is obtained using the first-order differential equation and can be deduced as [18]

$$\langle \mathbf{F} \rangle_{grad} = \pi \epsilon_0 \epsilon_h a^3 \left(\frac{\epsilon_n - \epsilon_h}{\epsilon_n + 2\epsilon_h} \right) \nabla \left| E_0^2 \right| \tag{1.8}$$

where, ϵ_0 are the permittivity of vacuum. The gradient force is an outcome of the zeroth order of the optical force experienced by the particle, which means that it depends on the incident optical intensity. The last term of the eq. 1.7 is the scattering force and obtained by the second-order differential equation required for the optical force and can be deduced as [18],

$$\langle \mathbf{F} \rangle_{scat} = \frac{4}{3} \pi \epsilon_0 \epsilon_h k^4 a^6 \left(\frac{\epsilon_n - \epsilon_h}{\epsilon_n + 2\epsilon_h} \right)^2 \left| E_0^2 \right| \tag{1.9}$$

This term is an imaginary component of the optical force, and hence it is known as the non-conservative force. This term accounts the scattering force, which arises due to transfer or loss of photonic momentum occurred by the particle with incident light.

In particular, we notice that the optical forces are directly related to the particle size as $F_{grad} \propto a^3$ while $F_{scat} \propto a^6$. It suggests that, the smaller the particle, the more gradient force will rise as compared to the scattering force.

1.2.3 Intermediate regime

The exact solution of the force is described using the Maxwell stress tensor, which is also known as energy momentum tensor of the electromagnetic field. This exact calculation of the optical force is first deduced by Mie, who computed the interaction of a monochromatic light electromagnetic field with a spherical particle [19]. The time average optical force which is acting on the spherical particle can be expressed in terms of the Maxwell's stress tensor T as [16],

$$\langle \mathbf{F_i} \rangle = \frac{1}{2} \mathfrak{Re} \left\langle \int_s T_{ij} . n_j ds \right\rangle \tag{1.10}$$

where $\mathfrak{Re}$ is the real part of a complex number, n_j is the outward normal unit vector to the surface enclosed by the particle, and i, j are representing the tensor components. The Maxwell stress tensor represents the flux of the electromagnetic field momentum across an area and can be expressed as [16],

$$T_{ij} = \epsilon_h \epsilon_n E_i {E_j}^* + \mu_h \mu_n H_i H_j^* - \frac{1}{2} \delta_{ij} (\epsilon_h \epsilon_n E_k {E_k}^* + \mu_h \mu_n H_k H_k^*) \tag{1.11}$$

where ϵ_n and ϵ_h are the electric permittivity and μ_n and μ_h are the magnetic permeability of the particle and host medium, respectively. Optical force calculation using this method is applicable for all particles size but it requires a rigorous calculation to deduce the derivation of all six electromagnetic components at the particle's surface [20]. In general, this method allows an exact calculation of optical force to understand a complete picture of trapping events especially for the intermediate regime colloidal particles.

1.3 State of art

1.3.1 Beam focusing optical tweezers

Since the early development of optical tweezers, researchers have started implementing it in various disciplines from atomic and molecular physics to soft-matter physics. Especially in bio-physics, it has found exciting application as a non-invasive trapping and manipulation tool for biological microparticles such as tissues, living cells, and bacteria suspended in liquid medium [21], [22]. Some of the research groups have implemented this technique to investigate light-matter interaction with different types of even smaller particles by implementing the considerable effort to improve in trapping technique [11], [16], [23]–[26]. In addition, numerous techniques have been developed to achieve high trapping performance and therefore expanding its application. For example, holographic optical tweezers setup is one of the popular instrument developed by Curtis et al. (Figure 1.5) [12], [27]. This tweezers setup allows trapping of array particle using the holographic light beams produced using spatial light modulators [12], [28]. This technique is capable of trapping multiple particles, simultaneously with specific computer generated holograms. Therefore, it has provided a versatile interface in studying the dynamics of complex biological specimens [29]–[31].

The other popular alternative to historical or conventional approaches is plasmonic optical tweezers. It has made it possible to use an evanescent field generated as a result of the total internal reflection of light at dielectric-metal interface [5], [10]. Using the evanescent field, the surface plasmonic resonance (the collective oscillations of free electrons) has been in the metallic surface (Figure 1.6) [32]. This approach allows confining light well below the sub-wavelength region, and therefore, significantly increases the gradient strengths while limiting scattering forces for the optical trapping [5]. Also, this technique can be easily integrated with microfluidics systems via a lab-on-a-chip platform [33]–[35].

Besides, the integration of the photoluminescence (PL) technique to the optical tweezers has provided enhancing the high-resolution imaging, and it is possible to measure the PL of trapped particles using spectroscopy. Due to its ability to distinguish a molecule or cell precisely, fluorescence microscopy has become undoubtedly the most useful tool for studying the dynamical changes in cells or other biological molecules [36]–[38]. The recent work on integration of fluorescent microscopy technique has allowed high resolution imaging of single molecules to track and manipulate them with a high precision [39]–[43].

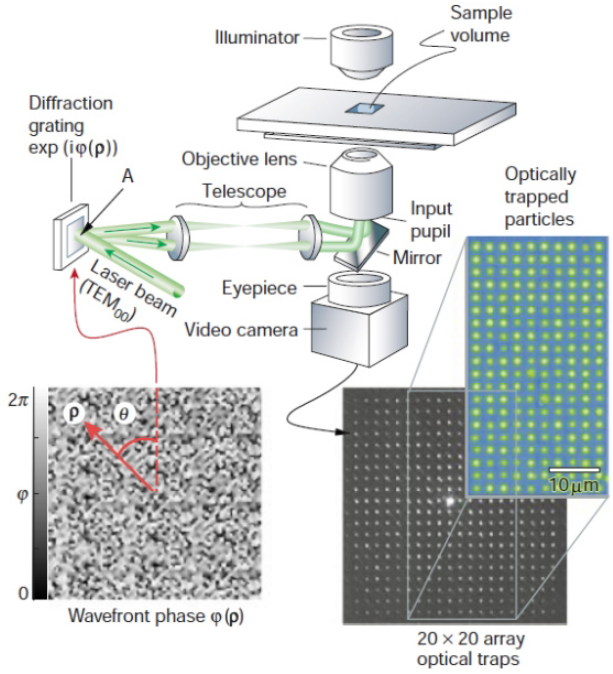

Figure 1.5: (a) A scheme of holographic optical tweezers setup developed by Curtis et al. [12], [27]. This tweezers has been used for demonstrating the trapping of 400 particles with a diameter of 0.8 μm simultaneously.

It is also important to highlight the recent works considering the implementation of optical tweezers for investigating the optical properties of luminescent nanoparticles and quantum dots that have shown interesting features for fluorescence bio-imaging or bio-sensing applications [45]–[48]. The use of optical tweezers has allowed to investigating the luminescence properties at a molecular level via trapping a single molecule [31], [43]. In this context, Reece et al. (2009) has demonstrated PL characterization of optically trapped InP semiconductor single nanowires in water by combining the optical tweezers with photoluminescence excitation (Figure 1.7) [44]. Based on the maximum PL emission observed, it has been possible to distinguish nanowires' structure using their individual spectra [44].

PL spectroscopy allows determining the structure of semiconductors nanoparticles

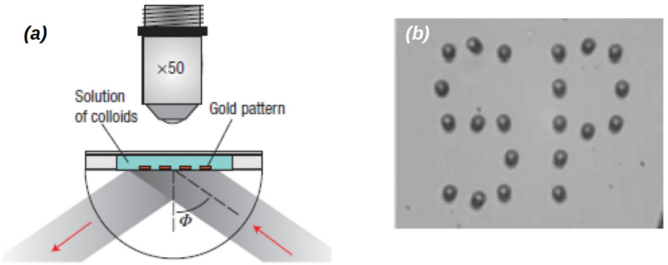

Figure 1.6: (a) A plasmonic optical tweezers setup has developed by Righini et al. [32]. (b) The trapped particles in SP pattern.

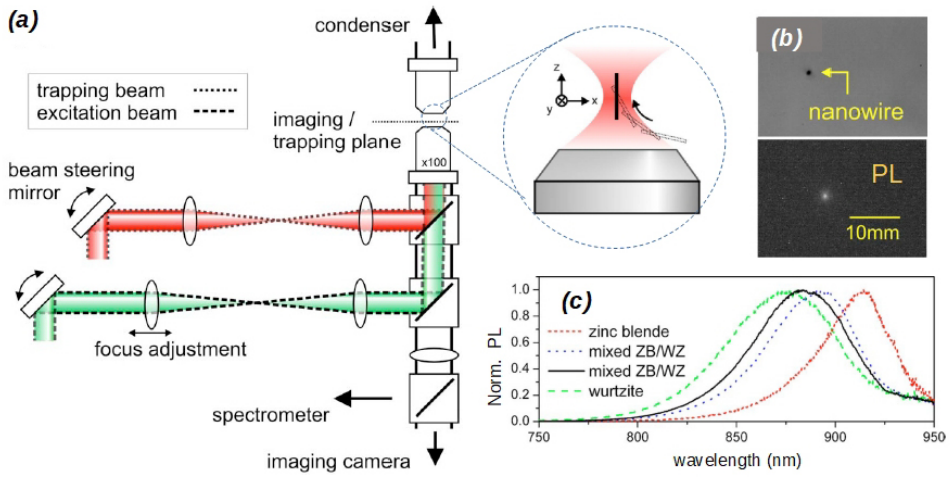

Figure 1.7: (a) A scheme of experimental setup used by Reece et al. for InP nanowires trapping and studying the PL emission. (b) A trapped nanowire in bright field and PL images (c) comparison of observed spectra to distinguish the nanowire structure [44].

as well as providing information of the bundling through the study of energy transfer and interaction with the local environment [49]–[54]. The local environment of nanoparticles plays a major role in bio-sensing or biomarker applications [55]–[57]. Also, this facility has attracted the researchers to characterize the such as rare-earth doped nanoparticles, which are intrinsically depending on host matrix, doping, shape, size, crystalline structure, composition, environment [58]–[60]. These nanoparticles provide significant advantages, including long-term photochemical stability, long luminescence lifetimes, narrow emission lines, and size-independent spectral shape of their luminescence bands [56], [61]–[64]. Rodríguez-Sevilla et al. have performed spectroscopic investigation of optical upconverting Er^{3+}/Yb^{3+} doped-SrF_2 nanoparticles (Figure 1.8) [62]. They have reported the influence of inter-particle interaction effects that have affected the luminescent properties of colloidal suspensions of upconverting nanoparticles. Another popular integrated spectroscopic technique, called Raman spectroscopy uses light scattering techniques to provide details of chemical structure, phase and polymorphism, crystallinity, and molecular interactions [65]–[67]. The details of these techniques can be found in the referred article [10].

Optical trapping, particularly in air, was first observed after the Ashkin approach was realized by Omari et al. Stable optical trapping of glass spheres of 5 μm in air using a single-beam gradient force was reported by Omori et al. (1997) [68]. However, since then, it is very less explored medium because it does not have a stable environment for the levitating particles movement [68], [69]. It is challenging to trap airborne particles because of the external perturbation caused by environmental factors such as acoustic shocks, mechanical vibrations, thermal drifts, and airflows [70], [71]. Usually, in the presence of higher density and viscosity, water significantly dampens these factors and provides highly stable conditions [72]. Moreover, the aqueous environment supports the essentials required for the living biological samples. It is interesting to study trapping properties of these particles in reduced environmental conditions (or trapped conditions) considering the recent challenges in physical, chemical, life, and atmospheric sciences.

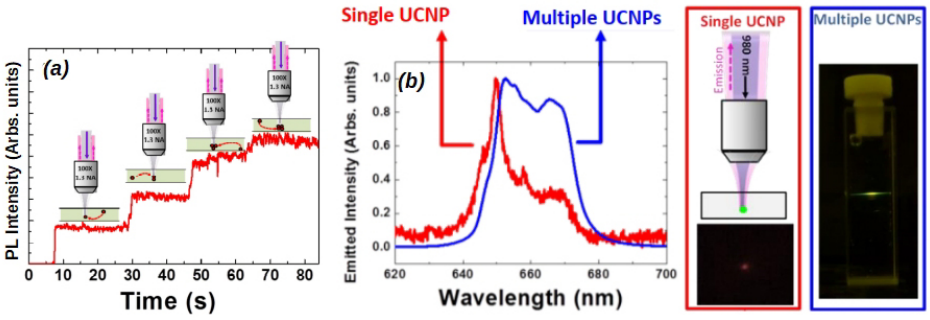

Figure 1.8: (a)Time-dependent PL generated by optically trapped UCNPs which has been measured as a function of the number of nanoparticles increasing in the optical trap. (b) Emission spectra have obtained from a single and multiple UCNPs [62].

Thus we would like to highlight the experimental developments focusing on the trapping in air.

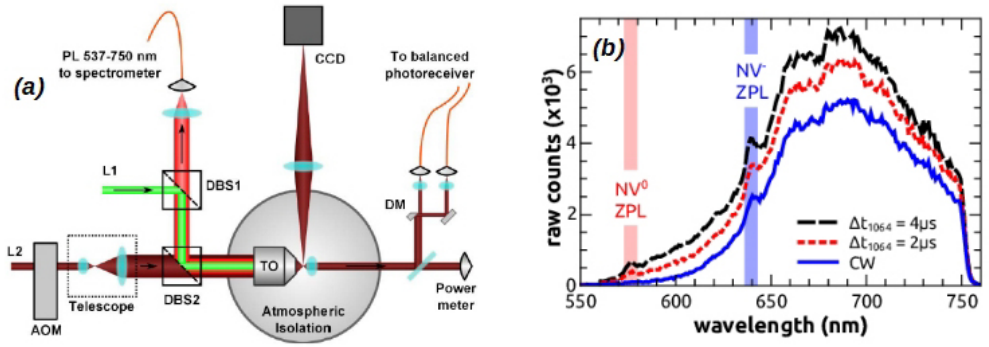

Figure 1.9: (a) An optical tweezers setup used for studying the nitrogen-vacancy in nanodiamonds[51]. (b) PL spectra which represent the nitrogen-vacancy measured at different time duration of pump laser.

The D. McGloin group reported manipulation and trapping of water aerosols and airborne particle arrays using holographic techniques [73]–[75]. Later this group reported the Raman spectroscopic investigation on the trapped aerosols droplets of sub-picoliter volume using a similar trapping technique [76]. Afterward, this technique was used by Shvedov et al. (2009) for demonstrating the first optical guiding of the single absorbing nanoclusters (0.1–10 μm) in air with the counter-propagating optical vortex beams [77], [78]. Pan et al. (2012) reported the trapping of single carbon nanotube clusters in air using the photophoretic force, which originate from heat produced when particles absorbed light. This trapping was performed with two counter-propagating hollow beams generated by axicon lenses [79]. Also, they implemented this tweezers setup for measuring the Raman spectra on trapped particles. Later, their group reported this trapping with different optical configuration [80] and optical manipulation of the single particles in air [81]. Neukirch et al. have studied the nitrogen-vacancy through the PL spectroscopy of an optically levitated luminescent nanodiamond suspended in a free-space (Figure 1.9) [51]. For this free space trapping, they have used an optomechanical cooling approach.

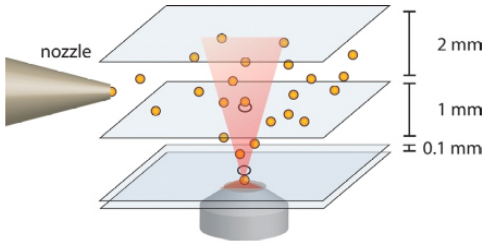

Figure 1.10: A design of optical trapping chamber used for trapping of gold nanoparticles. [82].

Jauffred et al. have reported the efficient trapping of airborne gold nanoparticles (80 to 200 nm) using a single beam optical trap [82]. For this trapping experiment, they have injected gold nanoparticles suspended in ethanol to a three-layer sealed chamber (Figure 1.10).

1.3.2 Fiber optical tweezers

Fiber-based optical traps are reliable and promising alternatives to the conventional optical tweezers. The fibered optical tweezers have emerged after the demonstration of fiber-based optical manipulation by Constable et al. (1993) using two counter-propagating beams [83]. In this configuration of the light beam, the principle is similar to the conventional optical tweezers for producing an effective trap close to the focal point, where the gradient force overcomes the scattering force. The light beam emitted by a cleaved standard single-mode optical fiber diverging. Therefore, it is necessary to find solutions for focusing the light beam to improve the gradient force.

Later, Lyons et al. have produced optical trapping using the counter-propagating geometry of two tapered hemispherically lensed fibers [85]. Their work has enhanced the exploring the potential of fibered optical tweezers using the structured fibers and thus it leads to designing and fabricating fibers with specific application. In 2003, Taylor et al. have designed a hollow shape by chemical etching probe at the end of a single-mode fiber. The light emitted in a ring shape made it possible to trap silica spheres 2 μm in diameter to about 1 μm from the lens with a power of 2 mW [86]. In 2006, Liu et al. have reported the optical trapping of yeast cells in water using single-mode tapered optical fiber, fabricated by heating and drawing technique [87]. Later, Mohanty et al. (2008) have used wet chemically etched tapered fiber tips to demonstrate trapping of low refractive index particles and biological cells [88].

Liberale et al. (2007) have reported three-dimesional trapping and spectroscopic investigation of polystyrene spheres using the four microstructured lens fabricated at the end of bundle of four fibers. These lenses have a working principle based on the total internal reflection (TIR) of light. Later this same group has reported microstructured fiber configuration using four micro prisms, those have also worked on the principal of TIR of light. This microstructured fiber has allowed to integrate with microfluidics

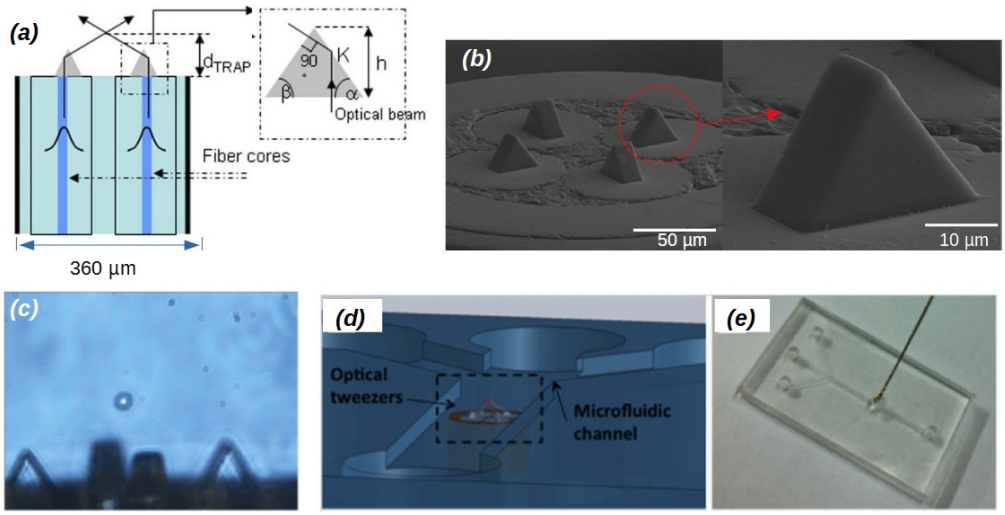

Figure 1.11: (a) Schematics to produced a light beam from the fiber probe used by Librale et al. using a bundle of four optical fiber. (b) Fabricated micro-prism on the fiber's end. (c) Trapping of a red blood cell. (d) and (e) Integration of fiber probe in a microfluidics system[84]

system and spectroscopy technique (Figure 1.11) [84].

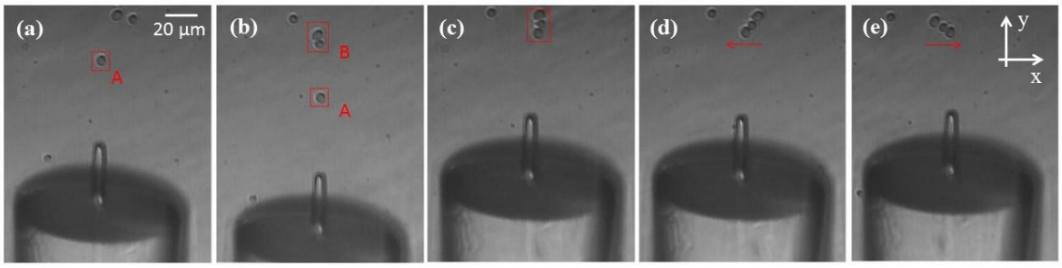

Figure 1.12: Optical manipulation of yeast cell using a fiber tip fabricated by photopolymerization [89].

Valkai et al. (2009) have reported the optical trapping of microparticles using two micro tips that have fabricated by the guided wave photopolymerization of the optical fibers [90]. Later, Ribeiro et al. have used a similar method to fabricate different microstructured fiber tips and demonstrated the trapping and manipulation of yeast cells with average diameters of 4 μm at a light power of 40 mW (Figure 1.12) [91]. They have also demonstrated organelles of plant cell manipulation using these fiber.

Xu et al. (2014) have demonstrated control of the orientation of a single silver nanorod with a diameter and length of 600 nm and 6.5 μm, respectively, using the counter-propagating light beams of two tapered fiber tips (Figure 1.13). They have shown that a rod can be rotated and then stabilized in different orientations by changing the fibers' position in the transverse direction. In this way, they have orientated a rod over a range of 152° by gradually varying the fiber position from -4 to 3.8 μm.[92].

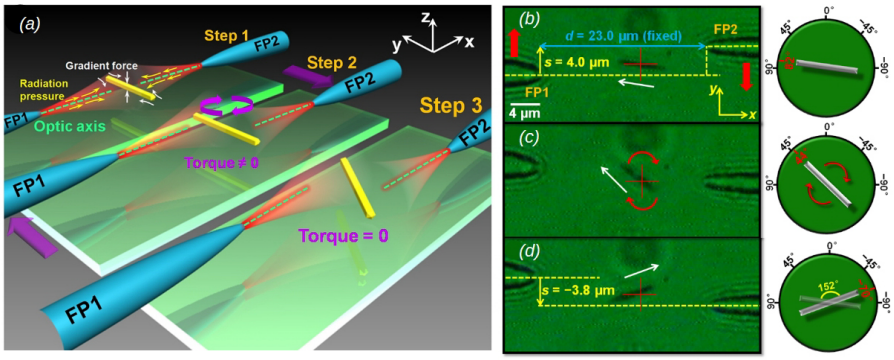

Figure 1.13: (a) Schematics of silver nanorod manipulation using two counter-propagating light beam. (b), (c), and (d) Images of nanorod manipulation at a power of 36 mW between remote tips 23 μm by moving one fiber in transverse direction. [92].

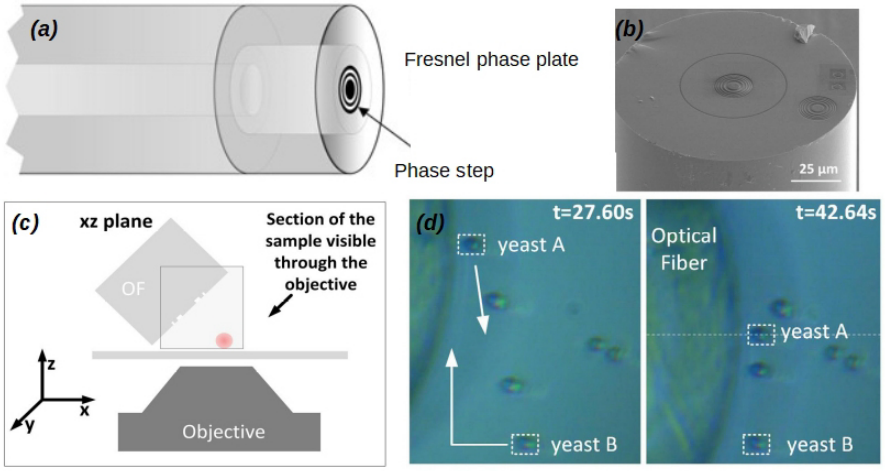

Figure 1.14: (a) Scheme of a Fresnel phase plate fiber. (b) SEM image of Fresnel phase plate fiber fabricated by FIB milling. (c) Scheme of the experimental setup used for trapping (d) Yeast cells trapping.[93].

Ribeiro et al. have developed Fresnel phase plates structured optical fibers (with focal length ~10 μm) by FIB milling process (Figure 1.14) [93]. Using this fiber they have demonstrated the optical trapping and manipulation of PMMA beads (8 μm) and yeast cells (~5 μm).

A very few work have been reported for particle trapping in air using fiber techniques. Rudd et al. (2008) have demonstrated the optical trapping of airborne salt–water droplets using counter–propagating geometries of cleaved single and multi–mode fibers [94]. They have trapped these droplets for a separation distance between two fibers of 170 and 240 μm, and they studied the droplet size as a function of light power.

Horstmann et al. have reported the optical manipulation and trapping of single airborne droplets of water-glycerol ranging from 500 nm to 1.9 μm in diameter using an integrated fiber-capillary trap fabricated onto a microscope slide (Figure 1.15). This

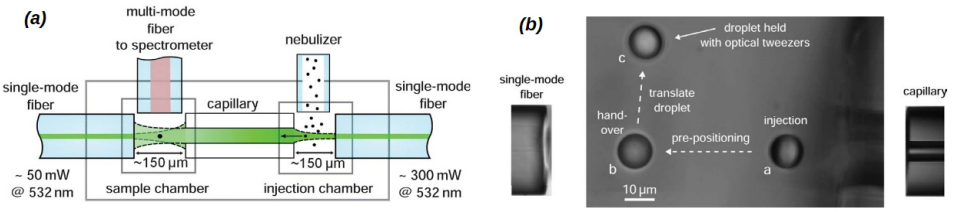

Figure 1.15: (a) Schematics represents optical trapping of airborne particle using the fibers and an integrated optical trap chamber. (b) The steps of water-glycerol droplets trapping experiment using the counter-propagating light beams (d = 10 μm) [95].

chamber allowed selectively single aerosol droplets for optical trap via a light guiding glass-capillary [96]. This glass-capillary separated the injection and trapping chamber. This specific experimental setup allowed to perform the cavity-enhanced Raman spectroscopy on the trapped droplets using a multi-mode fiber [95]

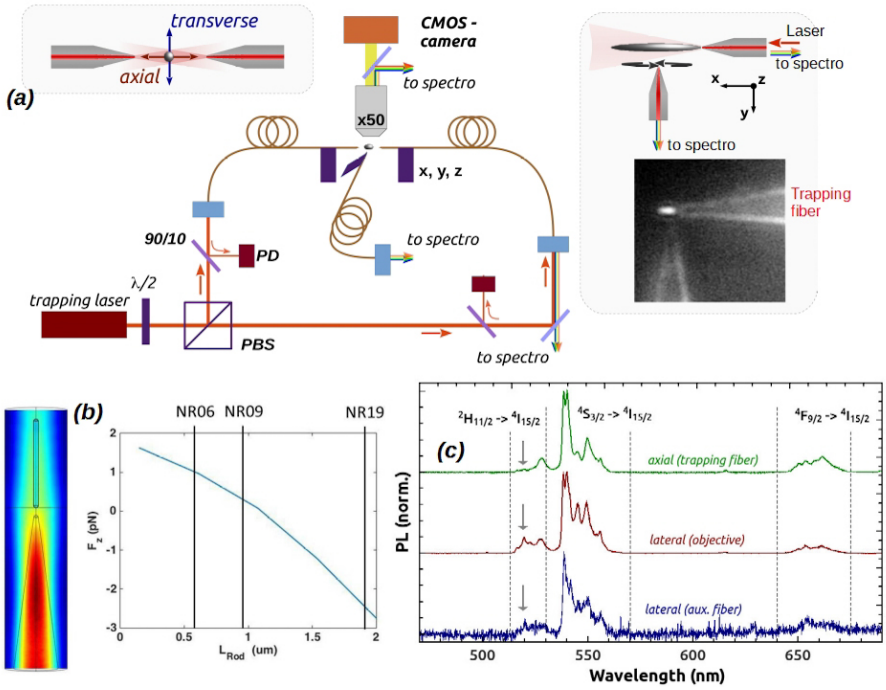

Figure 1.16: (a) Schematics of fiber tweezers setup used for nanorods. (b) The plot of optical force measured for three different nanorod sizes. (c) The PL emission recorded in the three directions [4].

Our group at Institut Néel is developing two distinct fibered optical tweezers setups working in suspension (water) and air. The suspension tweezers setup based on two tapered fiber tips has been developed as a part of the doctoral research work of J. B. Decombe [18]. In his research work, he has first demonstrated the trapping of polystyrene microparticles using the counter–propagating geometry of two chemically etched fiber tips [2]. He has used this experimental setup to study the trapping behaviour of luminescent particles such as YAG:Ce^{3+} nanoparticles of two different sizes, 60 nm and 300 nm [3]. Moreover, a counter–propagating geometry of fibers with a nano-antenna

fabricated at the fibers ends using a wet–chemical etching process have implemented for the polystyrene microparticle [97]. Furthermore, we have used this tweezers setup for studying the optical trapping of Er^{3+}/Yb^{3+} doped $NaYF_4$ nanorods with different aspect ratios (Figure 1.16) [4], [98]. The nanorod trapping has exploited for studying the up-converting luminescence feature of Er^{3+}/Yb^{3+} by integrating fluorescent spectroscopy.

Chapter 2

Experimental techniques

Introduction

This chapter will describe our experimental techniques that include two distinct fiber optical tweezers setups and data analysis techniques for characterizing trapping measurements. At first, we will explain the air tweezers setup and its working principle and the experimental measurements to optimize the trapping chamber. It will be followed by the suspension tweezers setup and its working process. Following the description of these setups, we will present the optical fibers used in the measurements. Lastly, we will explain our approach to characterize an optical trap.

2.1 Air tweezers

A major goal of this thesis is to design and develop a homemade fibered air tweezers setup for trapping of airborne nanoparticles without using any expensive and complex vacuum equipment. For designing this setup, a few specific considerations are required for the particle feeding system and the trapping chamber [73], [99]. It is considered that the lower viscosity of particles in air, which can lead to higher Brownian motion and lower thermal conductivity in air can influence the experimental measurements [82]. Also, the particle experiences high adhesive forces (Van der Waals forces, in particular) in air [100]. This force exceeds by several orders of magnitude than the optical trapping forces, which is in the range of piconewton. Figure 2.1 presents a schematic diagram of a homemade fiber optical tweezers setup consisting of a laser, optical fibers, positioning stages, microscope, and a particle feeding system.

2.1.1 Laser and fiber positioning

A laser is one of the important parts of the optical tweezers. For our experimental setup, we have used a single-mode laser module (LU0808M250, Lumics), an optimized GaAs

substrate-based quantum well laser diode with a wavelength (λ) of 808 nm and maximum output power of 250 mW. We have already demonstrated a reproducible optical trapping of different types of nanoparticles using dual fiber tweezers in suspension at this wavelength. This particular wavelength is chosen due to the following reasons:

1. It allows us to couple the light in a guided mode to pure silica core optical fiber. However, pure silica core fiber does not work anymore in the guided mode above this wavelength. In the case of our experimental setup, we are using optical fiber tips that have been fabricated by wet chemical etching of pure silica core optical fiber (S630-HP).
2. It allows using Si-based photodiode, which works effectively in the 400-1000 nm wavelength region.
3. This wavelength is sufficiently distant from the visible range, which allows studying the luminescent nanoparticles.
4. The light is less absorbed by air at this wavelength.

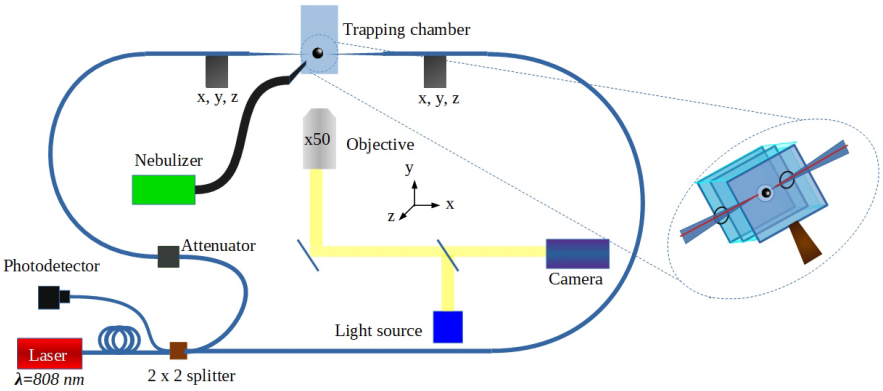

Figure 2.1: Schematic diagram of a dual fiber optical tweezers setup which is designed for particle trapping in air. Inset shows the two layered trapping chamber made of a glass slide and paraffin film.

A 2 × 2 optical fiber coupler/splitter (TN808R5A2, Thorlabs), which is made of fused silica is introduced to divide a laser beam into the two equal outputs. An input port of this coupler is connected to laser source and on the other side, two output ports are connected to two identical fibers tips which is suppose to be use for trapping. A fourth port is connected to a photodiode to read the transmitted signal in the counter-propagating geometry of fibers.

We measure each fiber tip's output power using a portable power meter (PM130D, Thorlabs) before positioning them on translation stages. This power measurement allows balancing the output powers in each fiber tip before each trapping experiments. In the case of an output difference, we use an attenuator to balance the power of a fiber having the maximum output. At the end of trapping experiments, we re-measure the tips output, which is then used in experimental measurement analysis.

Fiber positioning

The fiber positioning is designed to mount the fiber tips using two identical piezoelectric translation stages (SLC-1730, SmarAct) in counter-propagating geometry. The translation stages allow positioning the fiber tips in x-y-z-directions with high accuracy. The precise movement of the stages allows scanning the tip-to-tip (or fiber-to-fiber) transmission, which is used for characterizing the fiber tips before the trapping experiments. Figure 2.2 shows the diagram of transmission measurement in which one fiber tip is coupled to the laser, and another fiber tip is connected to a photodiode (PDA100A-EC, Thorlabs). The fiber tip at the photodiode side scans the transmitted light of the fiber tip coupled to the laser. Based on the scanned transmitted light, a transmission map is generated using a program in Labview. This measurement also allows finding the maximum intensity point where the fiber can be directly positioned during the trapping experiments.

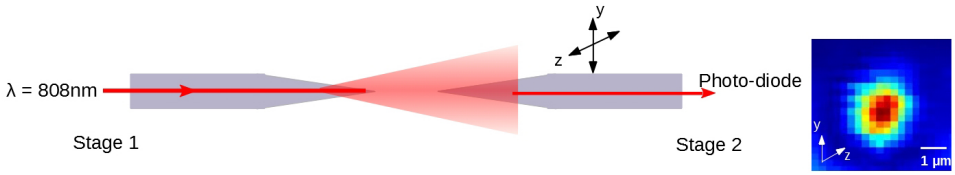

Figure 2.2: Scheme of tip-to-tip transmission measurement to characterize the fibers and positioning them during trapping experiments. A transmission map (shown at the right side) is obtained by scanning the light transmission in the transverse planes (y and z).

For mounting these fiber tips on the translation stages precisely, we optimize the fiber positioning conditions, such as the use of a capillary tube. Initially, the light transmission is found affected by the fiber's vibration, which is revealed in the transmission maps. Therefore, we use two capillary tubes (diameter of 500 μm) to place these fibers, which allows us to limit their vibration.

2.1.2 Particle visualization

We have developed a homemade inverted microscope for particle visualization. The microscope is assembled on an optical table and is versatile to add or remove the setup components. It comprises of a microscope objective, a CMOS sensor camera, and a white lamp.

We have used a microscope objective (Mitutoyo) with x50 magnification and a numerical aperture (NA) of 0.55. The long working distance (13 mm) of the objective allows observing our samples while maintaining a reasonable distance from it. It has a low focus depth of 0.9 μm and a resolution of 0.5 μm, close to the Rayleigh limit. This microscopic objective is mounted on a piezoelectric stage that has only one-dimensional movement.

We have chosen to use a CMOS camera (C13440-20CU, Hamamatsu) because it allows recording image sequences with high frame rates (measures in frames per second or

fps), good resolution, and high sensitivity. The camera displays a 16-bit full-frame image with a pixel size of 2048 × 2048 pixels. The image has a resolution of 130 nm/pixel with a frame rate of 100 fps. By reducing the frame size of pictures to 100 × 100 pixels, we can achieve a frame rate of up to 1000 fps. The frame rate is essential for the characterization of recorded videos. It is necessary for investigating the trapped particles with a high-frequency movement with higher frame rates. Furthermore, it is more sensitive, which allows visualizing the nanoparticles with high resolution, which offers to determine the precise location of the object. Also, a white lamp source is assembled to the microscope to illuminate the particles and fiber tips.

The recorded videos are treated to characterize the experimental features. In a typical video treatment, we have used Image J (a free Image processing software) to manually determine a time-dependent particle position tracking curve [101]. This tracking allows determining the particle speed and optical force using a homemade program developed in the Scilab environment [102].

2.1.3 Particle feeding system

The trapping chamber is one of the main concerns for this experimental setup since all trapping experiment is supposed to performed inside a controlled environment. As we have mentioned at the beginning of this chapter, the main concern is about developing a trapping chamber at low-cost and without any vacuum equipment. Initially, this chamber is designed based on finding a sufficient number of free-falling droplets and particles with very low speed. Later, it is considered to modify based on flexibility to particle trapping experiments.

Preparation of trapping chamber

We have developed a trapping chamber which has two chambers: an upper and a lower chamber. These two chambers are separated by a thin glass slide (Figure 2.3 (a) and (b)). This glass slide has a hole (1 mm) in its center. The upper chamber is designed to store the injected particles and provide them sufficient relaxation time. It is considered that the relaxed particles should fall inside the lower chamber through the hole. For the preparation of the trapping chamber, we required transparent paraffin film, glass slide (l = 50 mm, w = 10 mm, and t = 1 mm), thin glass slide (l = 30 mm, w = 10 mm, and t = 0.1 mm), and a tube of vacuum grease.

We have used a glass slide of 0.1 mm thickness and drilled a hole with a diameter of 1 mm using a diamond driller. We then fix this glass slide under a hollow slab of paraffin film pile, which has been made by melting a thin paraffin film. A hole of 4 mm is drilled on the front wall of the hollow slab by inserting a hot needle. This wall hole is created for injecting the particle to the trapping chamber. Then the upper part of the slab is closed by a thin glass slide (0.1 mm). This prepared part is known as the upper chamber, which has a dimension of 10 mm × 10 mm × 7.5 mm in length, width, and height, respectively.

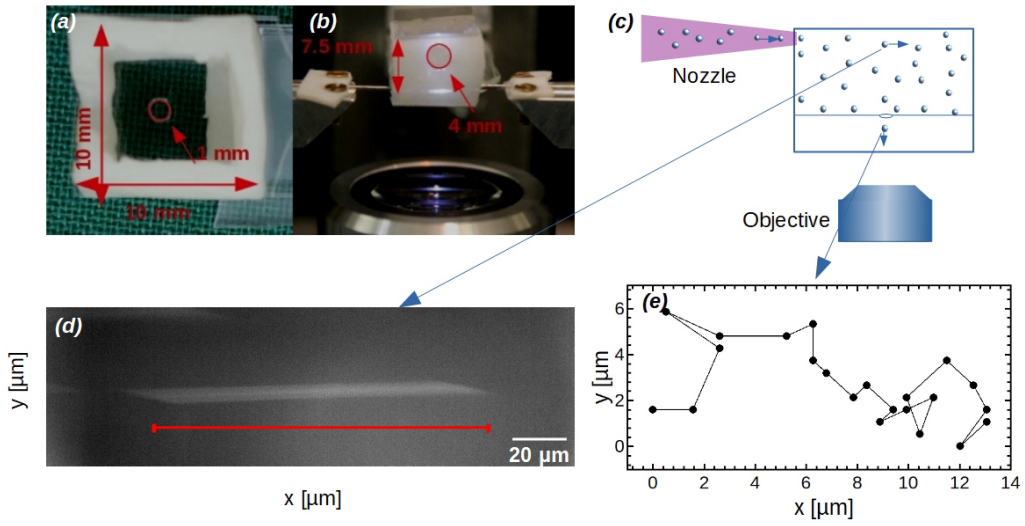

Figure 2.3: Image of the fabricated trapping chamber with two layers. (a) upper view of the chamber indicates a hole (1 mm) in the middle glass slide, which separates the chamber into the two parts. (b) Front view in which a wall hole (4 mm) is made to inject the aerosol using a nebulizer. (c) A schematic that is followed for studying the population and speed of the droplets and particles. (d) A microscopic image of an injected droplet which is captured at 500 μm above the glass hole slide. (e) A 2D plot of droplet motion inside the lower trapping chamber is measured at 600 μm below the glass hole.

Subsequently, the prepared upper chamber is fixed over another chamber, called the lower chamber. The same process is used for the lower chamber preparation, and it has a dimension of 10 mm × 10 mm × 2mm. The lower chamber contains two holes (1mm) to insert the two fibers tips. The combined chamber is fixed on a thick (1 mm) glass slide for support and placed on a translation stage. Once the fiber tips are entered inside the lower chamber, the lower holes are blocked using a vacuum grease to restrict aerosols leakage. The support of capillary tubes provides flexibility for the movement of fiber tips during the experimental measurements. It also protects fibers against grease.

Particle injection system

For injecting the particles inside the trapping chamber, we have used an aerosol nebulizer which contains an electronic oscillator to generate the high-frequency ultrasonic waves. This ultrasonic wave produces mechanical vibration in contact with a piezoelectric element, placed below a liquid reservoir containing water (or suspension). The piezoelectric vibration at high-frequency is sufficient to break the liquid or suspension into aerosol droplets. This nebulizer is used for inhaling the aerosols in the medicinal treatment of cystic fibrosis, asthma, and other respiratory diseases.

We have used deionized water to produce the aerosols of a droplet size 2-6 μm. In the case of microparticles (we will use the "particle" term only in this manuscript), we have suspended the polystyrene particle in ethanol to produce the ethanol aerosol. We

have used ethanol as suspending volume since it evaporates much faster compared to water. Rapid evaporation of ethanol allows particles to dry soon and fall freely.

After fabrication of the trapping chamber, we start to study the statistics of aerosol's droplets or particle population and speed inside both chambers. These statistics are important to optimize the trapping chamber parameters or dimensions, such as the height of the upper chamber, size of the wall hole (upper chamber), and size of the nebulizer nozzle.

The upper chamber height optimization is essential to fill it with a huge amount of aerosol, which contains the maximum number of particles at a given time. On the other hand, we require a certain amount of free-falling particles in the lower chamber through the hole at the lowest speed. The number of particles falling in the lower chamber is comparatively less to their population in the trapping chamber. A bigger upper chamber can be efficient for injecting aerosol in one time and provide enough space for droplets or particles to slow down before they fall into the lower chamber.

The wall hole size also impacts the particle injection since this hole corresponds to the intake capacity (for injecting aerosols once in time) (Figure 2.3 (b)). The nozzle size of nebulizer is related to aerosol droplet speed by which aerosol is injected into the trapping chamber. It also allows controlling the droplet speed, which we have observed by measurements. We find that a smaller nozzle size produces a higher aerosol flow intensity through its aperture.

Droplets

The droplets population is investigated inside the trapping chamber following the schematics presented in Figure 2.3 (c). First, we focus our microscope in the upper trapping chamber at 500 μm above the glass hole. A sufficient amount of aerosol is then injected into the upper chamber using the nebulizer, which is then stopped. We have observed the injected aerosol droplets, and their videos are recorded for measuring their population and speed. The number of droplets is counted in a few images of the video, and their population is approximated. However, we observed that the droplet size reduces with the time delay (when they have been injected). The reduction of droplet size is because of evaporation of water due to its low surface tension [75].

For making droplet size stable against the evaporation[99], we add a few milligrams of salt (NaCl) to 100 ml of deionized water. The solution is kept for 15 min in an ultrasonication bath for homogeneous mixing. As a consequence, droplets become more stable and has also enhanced life duration.

Similarly, the droplet speed is determined by observing the droplet movement in images. Due to the droplet higher speed, compared to our microscope recording rate (100 fps), only their long trail appears per image. Figure 2.3 (d) shows a microscopic image of the droplet trail, and its length is accounted for calculating the speed in the given image frame time. The droplets' speed is estimated to be $\approx$26 mm/s.

Then we focus the microscope in the glass hole at the same height and wait for 10 - 15 sec to see free-falling droplets. On this point, the droplet speed is relatively slower. Therefore they are observed in more than 10 images frames of a video. It allows estimating the droplet speed at this height as ≈700 μm/s.

Subsequently, we focus on 500 μm below the glass hole in the lower chamber. Here we observe the droplets are falling with Brownian motion. Figure 2.3 (e) shows x-y trajectory of a free-falling droplet in the vertical axis (z-axis). The speed of a free-falling droplet is determined to be 85 µm/s with a maximum time delay of about to 2.5 min.

Table 2.1: Table is presenting a statistics of droplets population in a given time (droplets/s) which has been observed with varying the nebulizer nozzle size and intake hole size of upper chamber

Nozzle size		Population per second		
(mm)	hole size =	2 mm	3 mm	4 mm
2		2	-	-
3		-	3.5	10
4		-	6	11

Further, we make a theoretical calculation using the free parameters to verify the droplet's speed in the lower chamber. For this calculation, we used the Langevin equation of motion ($F = m * a + \gamma * v = 0$) under the influence of gravity, where m is droplet mass, a ($= g = 9.8 m/s^2$) is the acceleration due to gravity, γ is the friction coefficient and v is the droplet speed [103]. In this equation, we neglect the influence of droplet Brownian motion. For the average droplet size of 5 μm, the speed is calculated as 580 μm/s without considering any environmental influence. The calculated speed of droplet is higher than the experimentally observed speed in the lower chamber. However, this allows us making an approximation of speed and further to proceed for the next step to optimize the trapping chamber.

These measurements are repeated each time when we make any change in parameters of the trapping chamber. Table 2.1 represents the statistics of droplet populations observed with different nozzle size and intake hole size. Whereas Table 2.2) represents the droplet population rate when we measure for the two different heights of the upper chamber.

Table 2.2: Table of droplets and particle population studied at two different height of upper trapping chamber.

Height	Population per second	
(mm)	droplets	particles
4.5	11	3
7.5	21	8

Polystyrene particles

For this measurement, we use dielectric spherical polystyrene particles with a diameter of 1 μm. We choose to use work with these particles for a few specific reasons. First, their size is of the same order of magnitude as the emitted laser beam by our fiber tip, which allows stable trapping [2]. Also, these particles are very well resolved for our microscopic observation. They have a very good size distribution and are readily available for commercial applications. Moreover, we have used these particles for optical trapping in suspension since they remain suspended in the water for several hours.

The particle population is determined using the same process, which is used for droplets. It has been mentioned earlier that we dissolve the particles in ethanol. The ethanol aerosols are injected into the trapping chamber. We directly measure their population at 500 μm below the glass hole. These particles are dissolved in ethanol, in such a manner that we can observe at least 5-10 particles among 100 ethanol droplets.

In the lower chamber, we mostly observe the particles which are falling freely since ethanol droplets evaporate rapidly. The particle population is determined using the recorded videos. Table 2.2 shows the statistics of particle population. The free–falling particles are observed with Brownian motion and falling with more delay than a droplet. Because of Brownian motion, the particles move in a 3-dimensional trajectory and making it difficult to determine their speed. To resolve this issue, we have used a three–dimensional approach that allows determining the particle's speed. This approach includes the measuring of visualization distance (v.d.), which is depicted in Figure 2.4 (b). This distance can be defined as the difference between the two points where the particle starts becoming visible and then disappear on the focus of the microscope.

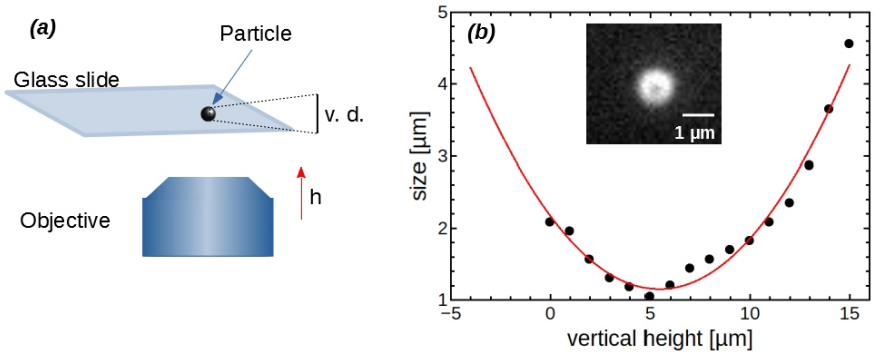

Figure 2.4: (a)A schematics of 3-dimensional approach in which the visualization distance (v.d.) is measured using a particle on the glass slide. (b) The plot of measured particle appearance size at different distance by moving the microscope. (Inset) A image of a particle (1 μm) which is used for size reference.

To measure v.d., a few μL of particle sample is spread on a glass slide. After drying the sample for 15 minutes, the glass slide is mounted on a piezoelectric stage and observed using the microscope. We focus on a particle that has appeared as a bright spot. The size of this spot is measured to ~1 μm, which allows referencing our approach to actual particle size. Subsequently, we observe this spot by moving the microscope verti-

cally to the point where the particle becomes visible and followed in a step of 1 μm until it disappeared. The v.d. in which the particle remains visible is measured to be 15 μm. In simple words, the particle remains visualized for 15 μm to our microscope when it is falling. A graph is obtained based on particle size appeared at different vertical height, moving the microscope objective (Figure 2.4). By fitting a polynomial function, it is revealed that the particle appearance varies in a parabolic shape when it passes over the microscope focus.

Subsequently, particle speed measurement is performed based on the recorded image sequences of a free-falling particle. The total time interval in which the particles remained visible is accounted for determining the speed. By knowing the v.d., it is easy to approximate the particle speed. The particle speed is measured in the range of 8 to 14 μm/s at 600 μm below the glass slide hole.

The particle speed is calculated to be 30 μm using theoretical calculation considering the parameter of polystyrene particle in air. For this calculation, we also do not include the Brownian motion or other environmental influences on the particle. Therefore, it appears comparatively higher than the experimentally measured speed.

To conclude this section, we optimize the different parameters of the trapping chamber based on the measurements carried out and the statistics obtained by estimating the population and speed of free-falling droplets and particles.

2.2 Suspension tweezers and spectrometer

We have another experimental tweezers setup, which is dedicated to particle trapping in suspension (water). Using these tweezers setup, the nanoparticles are trapped in single and dual fiber geometries [2], [104]. This experimental setup is flexible to combined other experimental techniques such as spectroscopy, which is used to study the emission properties of the optical trapped rare earth-doped nanoparticles [4]. The implementation of optical fibers with new techniques and design to this tweezers setup allow upgrading its trapping performance.

Figure 2.5 represents the scheme of suspension tweezers, which is used for trapping and investigating the photoluminescence properties of rare earth-doped nanoparticles. The main components of this tweezers are an 808 nm laser, a 395 nm pump laser, fiber positioning stages, a homemade microscope, an O-ring trapping chamber, and optical fiber tips. Some of this setup components are similar to air tweezers such as trapping laser, microscope objective, and some other optical elements such as photodetectors.

2.2.1 Laser and fiber positioning

We have used 808 nm laser as the trapping laser. It is similar to the trapping laser used in the air tweezers setup. A beam collimator is used to collimate a light beam. This light beam is divided into two equal arms using a polarizing beam splitter, and a half

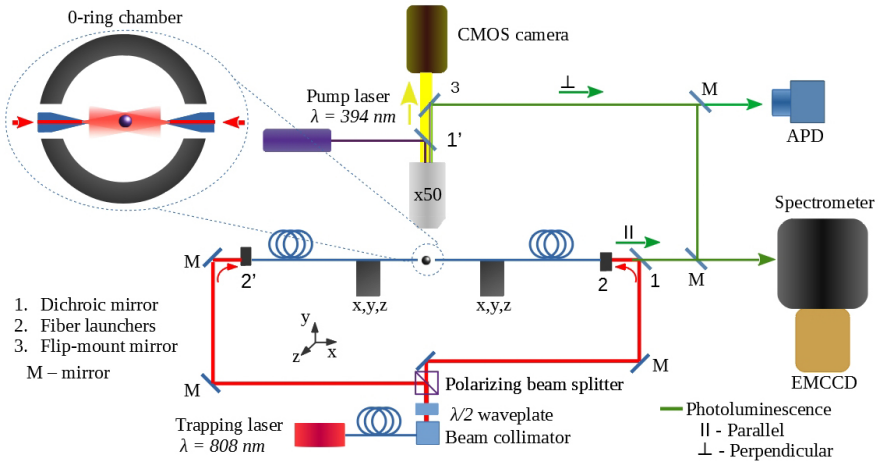

Figure 2.5: Scheme of suspension tweezers including the spectrometer which is used for particle trapping and studying the emission properties.

waveplate is introduced to balance the intensities in both arms. The light beams are coupled into the two identical optical fiber tips by the support of fiber launchers, placed at the end of both arms. The used fiber tips are mounted on two sets of x-y-z piezoelectric translation stages (P-620, PI, and SLC-17, SmarAct) employing two fiber holders. Here also, we use the power meter to read fiber tip output power of fiber in air.

2.2.2 Particle visualization

For trapping experiment visualization, we have used a homemade microscope setup, which is comprised of an objective lens (x50, Mitutoyo) and a CMOS camera (C11440-42U30, Hamamatsu). The sample image is focused on the camera sensor using a cylindrical tube, a lens, a filter, and a diaphragm.

This tweezers setup allows us to perform measurements in bright and dark field microscopy mode. The bright-field mode of the microscope is the simplest and most frequent technique used in experimental studies. In this technique, the sample is illuminated from below with a white light source, and its image appeared on the camera. Due to low contrast, this technique is limited only to the samples or particles having a refractive index close to water. Whereas, the dark-field microscopy technique is used to improve the contrast peaks and especially particles in suspension. The principle of this technique is to block the direct light and only detect the scattered and reflected light of sample. The bright-field can be easily turned to dark-field microscopy by introducing a plate in the light source.

Moreover, our setup is also dedicated to characterize luminescent nanoparticles trapping or the smaller particles having a size lower than the resolution of our microscope (500 nm). For visualizing the luminescent particles, we pump them at their excitation wavelength. For example, 395 nm pump laser (LBX-395HPE, Oxxius) is used for pump-

ing the Eu-doped nanoparticles.

2.2.3 Fluidic chamber

For making an experimental measurement in suspension, we have used a special and inexpensive trapping chamber made of a rubber ring (inset, Figure 2.5). We call it "O-ring chamber" which is prepared by cutting the rubber ring into two halves and fixed on a glass slide using vacuum grease. A few millimeter gaps are left between these two rubber parts to insert the fibers. The prepared trapping chamber is placed on a piezoelectric stage. Once the suspension sample is kept in the O-ring chamber, we insert the fiber tips inside this chamber and cover it using a cover glass slide. This system has the advantage of being quick and easy to carry out the measurements. This chamber is stable, and it works for several hours without much evaporation and yet very efficient.

In water, the adhesive forces (capillary forces and Van der Waals forces, in particular) are lower than the optical trapping forces, and therefore, it is straightforward that particles do not adhere to optical fibers like air. However, in a sample with a large number of particles, some particles can easily adhere to the optical fibers.

2.2.4 Spectroscopy

Our experimental tweezers setup has been upgraded to perform emission spectroscopy of the optically trapped luminescent nanoparticles. This feature is developed by assembling a spectrometer (SP2150i, Princeton Instruments)and coupling it with an EM-CCD camera (ProEM-1600, Princeton Instruments). This camera is sensitive to light, and it works very fast. It is cooled down to -70° C to reduce thermal noise. The spectra can be obtained over a wavelength range of 0 to 1400 nm with an accuracy of ±0.25 nm.

The experimental setup is designed in such a way that it allows recording emission spectra in the two directions; one parallel or along the fiber axis and the other perpendicular to the fiber axis. These two-directions can be easily identifying in Figure 2.5. The emitted emission is collected directly through a trapping optical fiber in the parallel direction. For the perpendicular direction, the emission is collected through the microscope objective by introducing a mirror on a flip-mount in front of the microscope camera. Due to this mirror, we are limited to either visualization by camera or spectroscopy. Besides, a set of optical filters are used for suppressing the trapping and pumping wavelengths. In addition, a linear polarizer in front of the spectrometer allows measuring the polarization-resolved spectra.

2.2.5 Photoluminescence lifetime

In addition, our experimental setup allows measuring the photoluminescence (PL) lifetime of the trapped luminescent nanoparticles. For this measurement, we have modulated the pump laser using a frequency generator (33120A, Hewlett Packard). The modu-

lated laser produces a light beam of the rectangular waveform, which has a decay time of ≈20 μs. A silicon avalanche photodetector (APD-440A, Thorlabs) is used for measuring the PL signal with a maximum gain of $2.65 \cdot 10^9$ V/W. It is connected to a digital oscilloscope (HMO1202 series, Rohde&Schwarz) to read the analog signals. The oscilloscope allows acquiring 1024 waveforms with an acquisition rate of up to 10,000 waveforms/s.

2.3 Optical fibers

The optical fiber is a key element of our experimental optical tweezers setup. It is a cylindrical waveguide consisting of three concentric regions: core, cladding, and plastic coating. The core is a central part of an optical fiber with a diameter of 3.5 - 5 μm. The cladding region that surrounds the core, can range from 5 to 125 μm in diameter. The lower refractive index of the cladding region compare to the core supports the light confinement in guided mode due to the total internal reflection (TIR). Finally, the cladding region is protected by a layer of plastic coating (245 μm) which provides flexibility to the optical fiber.

For our experiment, we have used five different types of structured optical fibers. The used fibers are prepared with different fabrication techniques which will be explained in the next subsections.

2.3.1 Tapered fiber tips

The tapered fiber tips are the most common optical fiber which we have been used for demonstrating the micro and nanoparticles trapping [2]. Besides trapping, these tips have shown interesting applications in optical microscopy of living cells [105] and studying the plasmonic coupling with metallic coating [104]. These tips are typical chemically etched optical fiber having a conical shape [106].

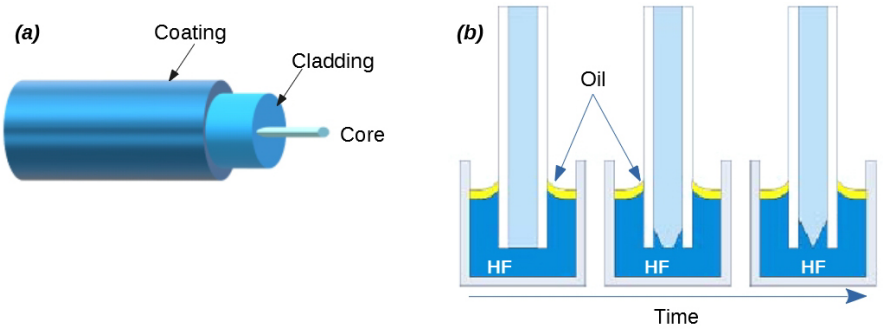

Figure 2.6: (b) A scheme of optical fiber with the three distinct parts: core, cladding and plastic jacket. (b) A scheme of tip fabrication process which is followed for wet chemical etching of optical fibers [107].

The taper fiber tips fabrication has been performed by Gwénaëlle Julie at Institut

Néel. They are fabricated by wet chemical etching of a pure silica core monomode optical fiber (S-630 HP, Thorlabs) which has a working wavelength of 630 - 860 nm. This etching experiment is based on a tube etching process in which an optical fiber is a tip dipped into HF with the a protective jacket or plastic coating (Figure 2.6) [107].This method has the controlled experimental conditions such as temperature, humidity, and vibrations, by keeping the partial plastic cover around the immersed fiber [106]. Before etching, the plastic coating of an optical fiber is removed partially at one end and dipped in the 40 % hydrofluoric (HF) acid (the acid which is known for dissolving the silica). A thin layer of organic solvent (silicone oil) was used for the prevention of the rapid HF evaporation.

A meniscus of concave shape forms due to contact of optical fiber and HF. The height of this meniscus is proportional to the diameter of the fiber. The fibers are etched from inside the hollow cylindrical plastic coating since this coating does not dissolve in HF. A complete etching cladding region turns into conical tip shape which forms inside the protecting layer. After 2 hours of complete etching, the fiber is dipped in DI water by replacing the HF to reduce the impact of residual etchant on the fabricated tip surface. After rinsing, the tip is dipped into toluene and acetone to remove the protective jacket.

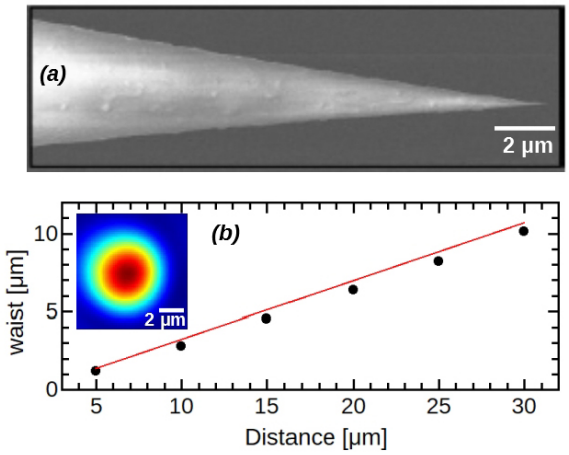

Figure 2.7: A SEM image of a typical tapered fiber tip which is observed after the wet chemical etching of optical fibers [18]. (b) The transmitted beam spot which is obtained by measuring the tip-to-tip transmission scanning (inset). A plot of emitted beam waist of a tapered fiber tip which is measured at different tip-to-tip distances.

The fabricated tapered fiber tips are investigated using a scanning electron microscope (SEM) (Figure 2.7). In this image, these fiber tips are observed with a typical apex size of 60 nm, a full angle is achieved upto 15° [18]. The emission property of these fiber tips are studied before using them for trapping experiments. Their emission properties are characterized by measuring the tip-to-tip transmission in air and analyzing the scanned transmission maps. The fiber tips emission properties are already reported by Decombe [2]. Therefore, we have performed a quick measurement to characterized the newly fabricated tips. The transmission maps are recorded varying the tip-to-tip distance (5 μm to 30 μm) between the two fibers.

The recorded transmission map which can be seen in Figure 2.7 (a), revealed a

Gaussian-shaped spot. The transmission maps of fiber are plotted with a Gaussian function having intensity $I(r)$:

$$I(r) = I_0 exp(-2(r - r_0)^2/w^2) \tag{2.1}$$

with I_0 is the intensity at the beam center and w is the beam waist. The beam has appeared with a spot size of 1 μm at 5 μm distance from the tip apex and then it increases linearly on increasing the tip-to-tip distance (Figure 2.7 (b)). Based on the analyses of transmission maps in air, we observe that the emitted beam through the fiber tips is diverging with a divergence angle (opening angle) of 20°. The numerical aperture N.A (= $n \sin(\theta/2)$, where n is refractive index of medium) corresponds to the divergence angle is measured about 0.17. In water, the divergence angle is reported about to 8°, and the transmitted intensity is three times higher than air [2].

After characterizing these fiber tips, we directly use these tips in trapping measurements. These fiber tips allow investigating optical manipulation of droplets and particles in the air which is discussed in chapter 3. These tips are also used in the trapping of $NaYF_4$:Eu nanorods and investigating their emission properties which are discussed in chapter 4.

2.3.2 Negative axicon fibers

The negative axicon fibers are also known as deep-seated negative axicon (DSNA) fibers since their axicons lie inside the hollow conical annular region [108]. The negative axicon fiber has two axicons: primary and secondary axicon which can be seen in Figure 2.8 (a). The principle of these fibers is based on the diverging (by primary axicon) and converging (by secondary axicon) of the light beam to produce a self reconstructive beam with a finite number of rings Known as quasi Bessel beam.

A Bessel beam contains an infinite number of concentric rings with a highly bright central spot so-called zeroth order. A Bessel beam is a non-diverging beam since its intensity remains constant for a long working distance [109]. A Bessel beam is a particular solution to the Helmholtz wave equation $(\nabla^2 + k^2)\psi(r,t) = 0$ which is obtained by using the Bessel function. In the Helmholtz equation, the term ∇^2 is a Laplacian, k is a wavenumber. The Bessel beam obtained in the form of a cylindrical wave equation as

$$\psi(r,t) = J_0(k_r\rho)e^{i(k_z z - wt)} \tag{2.2}$$

where, $J_0(k_r\rho)$ is zeroth-order Bessel beam function and $k_r^2 + k_z^2 = k^2$ is the propagation wave vector component in radial and longitudinal directions, respectively. The Bessel beam is produced after the interference of plane waves by conical prism known as axicon. The generation of a perfect Bessel beam is not possible since a Bessel beam requires an infinite amount of energy because of the infinite rings. But, it is possible to generate a quasi Bessel beam with a finite number of rings.

The negative axicon fibers are developed to generate a quasi Bessel beam using the etched fibers by S. Mondal's group, CSIO, Chandigarh, India. These fibers are implemented for the sensors applications such as used in the interferometer cavity [110] and

optical tomography of biological specimen [111].

The negative axicon fibers are fabricated by chemical etching of a photosensitive optical fiber [112]. Before etching, the fiber plastic coating is stripped off and then it is dipped into HF (48%). For these fibers, the core etching rate is faster due to the enriched GeO_2-doped silica core. The etching rate of the core and cladding are ≈24 μm/min and ≈1.7 μm/min, respectively [108]. The faster etching rate of core results to hollow conical shape inside the cladding region. The etching process is continued until the formation of axicons and then stops automatically after an etching time of 40 min. An axicon that is located at the core of fiber inside a hollow cone is known as the primary axicon. The other axicon which is located entirely in the cladding region near to the annular side is known as secondary axicon (Figure 2.8 (a)).

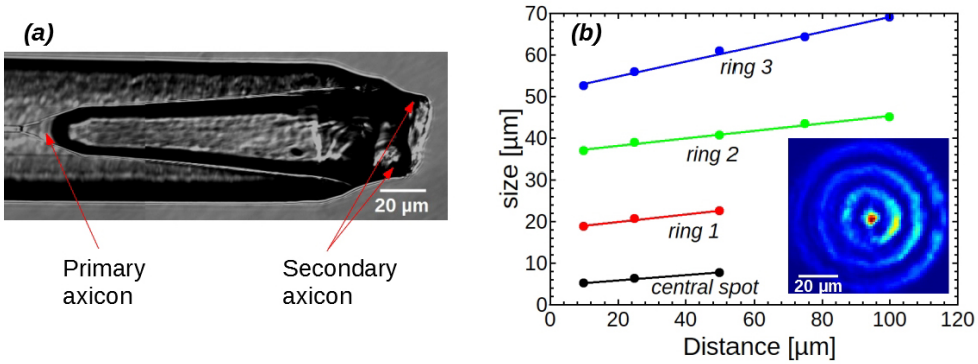

Figure 2.8: (a) A microscopic image of the negative axicon fiber. (b) (Inset) A transmission map is obtained at 50 μm fiber-to-fiber distance between two negative axicon fibers in counter-propagating geometry. A plot of central spot and rings sizes which are measured at different fiber-to-fiber distances.

Fibers emission property is investigated by scanning the fiber-to-fiber transmission in air. In a quick characterization measurement, the transmission maps are obtained at different fiber-to-fiber distances and are observed in their bright central spot surrounded by the concentric rings (Figure 2.8 (b)). A minimum beam waist of ≈ 5 μm is obtained at 10 μm fiber-to-fiber distance. The transmission maps reveal that the beam diverges along with rings which can be seen in a given plot (Figure 2.8 (b)). It is also observed that the first ring merge to the central spot in between the 50 μm - 75 μm. This effect suggests the self-healing feature of the beam.

The beam divergence angle is determined by using a plot of spot size at a different fiber-to-fiber distance. The divergence angles are 3.2°, 5°, 6°, and 10° for central spot, first, second, and third rings, respectively. We have used these fibers in studying the particle manipulation experiments which have been discussed in chapter 3. However, these fibers do not show good transmission in water because of bubble formation and thus these fibers are not used for particle trapping using suspension tweezers [113].

2.3.3 Positive axicon fibers

The positive axicon fibers are optical fibers with a nano-antenna which works as an axicon [112]. The axicon fiber is developed by S. Mondal's group, CSIO, Chandigarh, India. This fiber is designed to generate a quasi Bessel beam. These fibers have found interesting applications in particle trapping in suspension [114], [115], as an optical probe for chemical gas sensing, second harmonic generation [116], and plasmonic coupling with metallic coating [117].

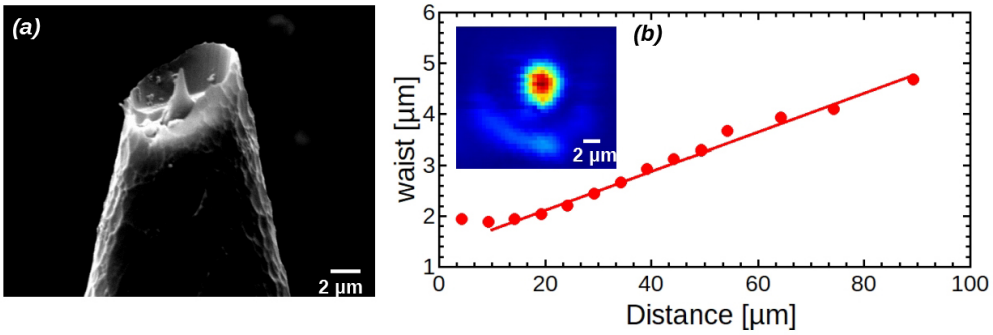

Figure 2.9: (a) A SEM image of a positive axicon fiber. (b) (Inset) The transmission map which is obtained at 10 μm fiber-to-fiber distance. A plot of beam waist vs. fiber-to-fiber distance at which transmission is measured.

The positive axicon fibers are fabricated by chemical etching of a photosensitive single-mode fiber by following the procedure discussed in ref [112]. For the etching of optical fiber, a hydrophilic polymer covered tube is filled with HF (48%) which forms a convex meniscus inside the tube. When an optical fiber is immersed into the HF, the fiber suppresses convex HF meniscus by forming a concave meniscus around the fiber cylindrical-shaped. HF reduces the diameter of the fiber by dissolving silica. This leads to a reduction of the concave meniscus along with the fiber. As a result, nano-tip is formed at the core of the fiber and a capillary rim at the cladding region which forms by etching of the core-cladding boundary. The different etching rates of core and cladding have played a role to form the axicon. An etched fiber is characterized in SEM (Figure 2.9 (a)) at CSIO, Chandigarh, India. A typical 100 nm sized nano-antenna is observed at the center of etched optical fiber. It has been surrounded by etched cladding rings. It has a height of ~4 μm with a base diameter of ~3 μm.

The fiber emission properties are characterized by scanning the transmission using two identical fibers in the air. The transmission maps are obtained at a different fiber-to-fiber distance and reveled a central spot (Figure 2.9 (b)). However, the central spot size is varying with the fiber-to-fiber distance. The mean beam waist size is calculated using the Gaussian fitting in two distinct planes (vertical and horizontal). The minimum beam waist is observed at 15 μm distance from the nano-antenna, which revels the focal point of the fiber. Further, the produced light beam starts diverging with an angle of ~4° (Figure 2.9 (b)). This divergence angle corresponds to a NA of 0.035. This angle is about 5 times smaller as compared to the divergence of tapered fiber tips.

The positive axicon fibers are implemented for studied particle manipulation which has been discussed in chapter 3. Moreover, a single and dual fiber geometries of these fibers are used for studying the trapping behavior of $NaYF_4$:Er/Yb nanorods (not mentioned in this manuscript) [115].

2.3.4 Fresnel lens fibers

The Fresnel lens fibers are the 3D printed fibers that have been made by depositing a Fresnel lens on the standard single-mode optical fibers (Figure 2.10 (1)(a) & (b)). A Fresnel lens is a diffractive optical element composed of a series of concentric radially symmetric rings that are alternating opaque and transparent zones. The radii of these concentric rings are given by [93],

$$r_n = \sqrt{n\lambda f + \frac{n^2\lambda^2}{4}} \tag{2.3}$$

where n be an integer, λ be the wavelength of light, and f be the focal length. In case of $\lambda << f$, the radii can be directly as $r_n = n\lambda f$. Thus, this can be designed based on the focal length and λ considering the application. In our case, these fibers are designed to generate a focused beam at a certain distance based on our trapping laser 808 nm. There are three types of Fresnel lens fibers with the N.A. 0.3, 0.5, and 0.7 which are designed using the software ZEMAX (V.13, Zemax, LLC). The laser beam propagates through the fiber core and gets expanded by propagating through a solid cylinder with a length of 500μm called a socket and then it gets converged by the Fresnel lens at a focal point. For designing the fibers N.A., their focal lengths are calculated in water using a phase function. The Fresnel lens fibers of NA 0.3, 0.5, and 0.7 have the focal lengths 200, 100, 50 μm, respectively, in water. The geometrical ray tracing of the fibers are obtained using the local grating approximation (Figure 2.10 (2)).

These three types of Fresnel lens structures are fabricated by femtosecond two-photon lithography using a Photonic Professional GT (Nanoscribe GmbH) system at 4^{th} Physics Institute, University of Stuttgart [118]. A commercial IP-Dip resist is used for fabricating the high-resolution features of the diffractive Fresnel lenses facet. The lens is deposited on single-mode fiber (S780HP, Thorlabs) with a cladding diameter of 125 μm and the core about 5 μm. The fabrication method allows fabricating the lens with the high aspect ratios of different segments. A minimum lateral size of 1.67 μm is chosen for the lens with N.A. of 0.3 and 0.5, however, segments reach to the outer border for 0.5. Thus, for the higher N.A. of 0.7, it is required to fabricate it using two lenses. The second lens is fixed over the first lens by the support of 6 pillars which are designed by mechanical design software. The diffractive power of 0.7 lens is distributed over two separate lenses and considering the water filling between these two lenses. The total writing times were 50, 55, and 80 min for the lenses of NA = 0.3, 0.5, and 0.7, respectively.

The basic features of the fabricated Fresnel lens are characterized by studying the beam profile in water using an inverted microscope which consists of a water immersion objective (studied at 4^{th} Physics Institute, University of Stuttgart). The beam profile intensity cut measurements are compared with an in-house wave optical simulation of

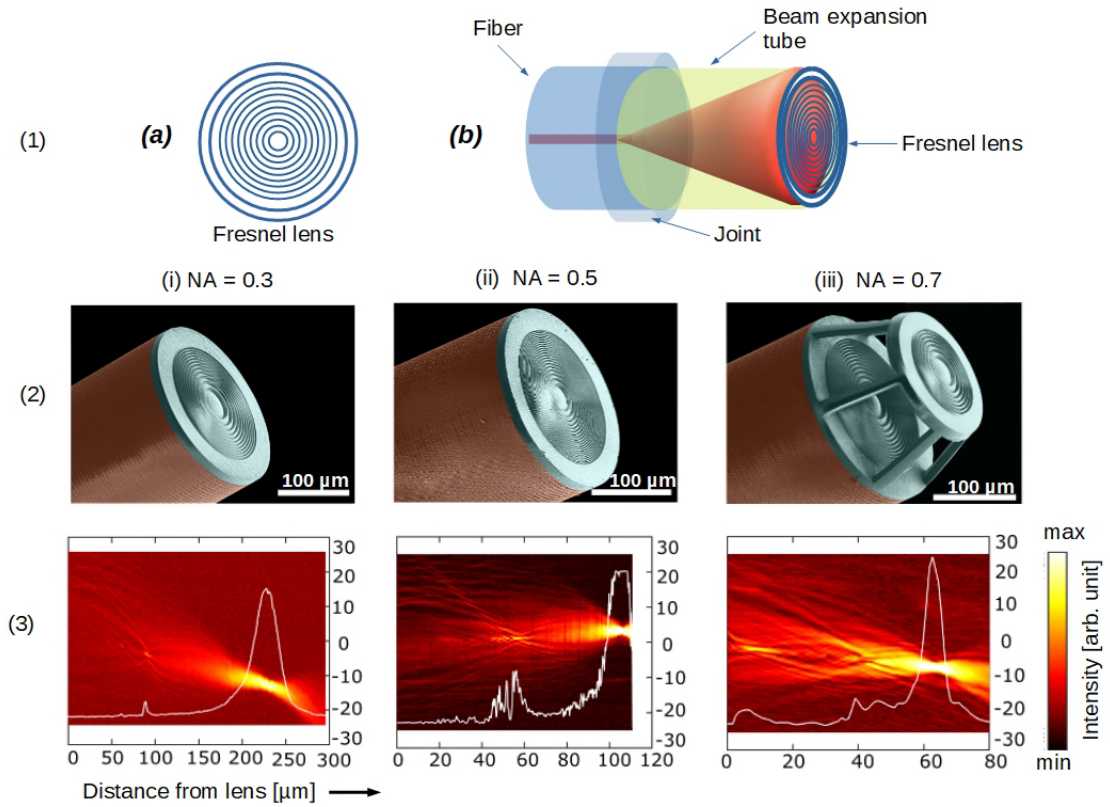

Figure 2.10: (1) (a) A schematic of Fresnel lens, (b) 3D printed Fresnel lens fiber. Images of Fresnel lenses with three different numerical apertures: (i) NA = 0.3, (ii) NA = 0.5, and (iii) NA = 0.7. Column wise, (2) their false color SEM images, and (3) beam profile measurements of Fresnel lenses in water. The white line is an axial intensity cut at the center of the beam produced by the respective fibers.

the lenses using a volumetric wave propagation method based on the beam propagation method (Figure 2.10 (3)). The measured and simulated axial intensity distributions have appeared good qualitative agreement to the shape of the beam.

The fiber-to-fiber light transmission is measured at Institute Néel before the trapping experiments. The transmission measurement is obtained at a different fiber-to-fiber distance (D_{f-f}) until the minimum spot size was observed. At twice the focal distance of the fibers, the obtained transmission maps have revealed an approximation of the circular Gaussian shape of the beam. For example, the beam waist measurements of the Fresnel lens with 0.5 are presented in Figure 2.11. The minimum spot size (waist) for this fiber measured to be ~1.13 μm. The beam spot size can be corrected since two identical fibers are used. This correction is made by dividing the spot size by $\sqrt{2}$ and calculated as ~0.80 μm. The beam waist varies parabolically near to the focal point of the fiber. The measured transmission in air and water reveal that light intensity is 1.4 times smaller in water. However, exact intensity measurement in water is difficult to be found since a significant fraction of light is scattered by these lenses. In such condition, this correction factor is not taken into account and only light power measured in air is used for analyz-

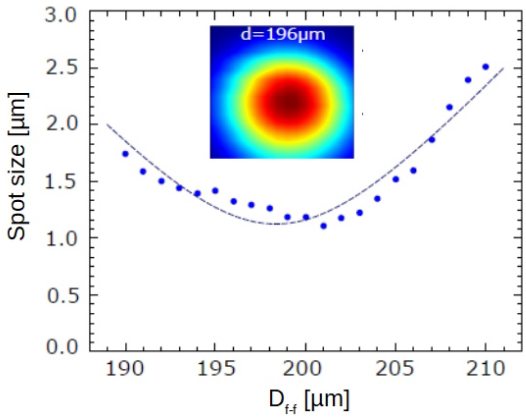

Figure 2.11: The beam waist plot is obtained at the different fiber-to-fiber distance. (Inset) The transmission map obtained at 196 μm between the Fresnel lens fiber.

ing the trapping measurements which is presented in chapter 4.The Fresnel lens fibers are used for stable trapping of nanoparticles.

2.3.5 Total internal reflection (TIR)-probe fibers

The TIR-probe fibers are the micro-structured probe (called TIR-probe) deposited on a single mode optical fiber. This TIR-probe is working on principle of total internal reflection (TIR) and it is particularly designed for the particle trapping in the single fiber geometry. This fiber is designed and fabricated at 4^{th} Physics Institute, University of Stuttgart. The TIR-probe is designed in such a way that it can produce a focused annular beam by total internal reflection of light which occurs inside the probe. It has a N.A. of 1.0 and a back focal length of 50 μm.

The TIR-probe is fabricated by 3D printing using a photopolymer in Nanoscribe.This probe is deposited on fiber with the support of an expansion cylinder made of polymer. During the fiber design and fabrication, a special consideration has given to maintain TIR effect at all surfaces by keeping all angles of reflection above the critical angle.

The light beam propagates through the single-mode fiber (SMF) to the expansion cylinder where it expands over a distance of 500 μm and split into two distinct branches (Figure 2.12 (a)). Light in the red branch gets reflected twice before it converges at focal point whereas in the dark yellow branch it gets reflected once. The probe is fabricated in such a manner that lights from the two branches converge at one focal point.

For characterizing the probe fiber, the beam profile measurement is performed in water at the same laboratory following the similar procedure used in case of Fresnel lens. The highest intensity is obtained at the focal point $\approx$ 50 μm from probe aperture in axial direction. We measure the transmission through the fiber probe at Institut Néel (Figure 2.12 (c)). For scanning the transmitted light we have used a tapered fiber tip since the probe fiber is meant for a single fiber geometry. Perhaps this is not the best way

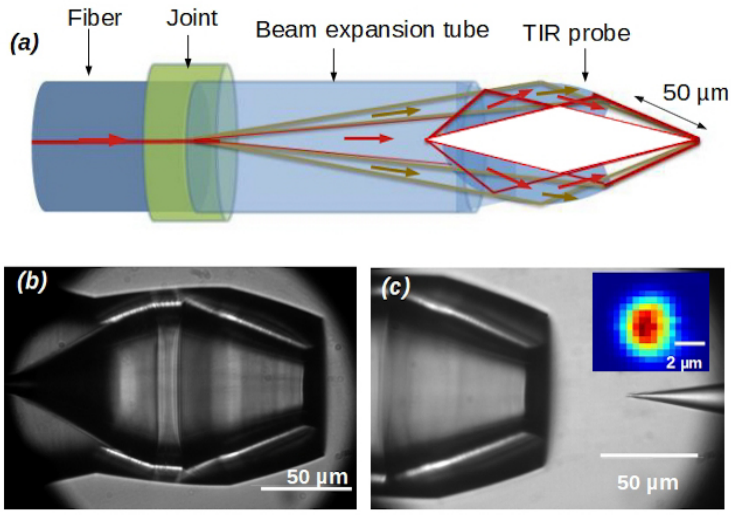

Figure 2.12: (a) A scheme of TIR-fiber's working principle. (b) The microscopic image of TIR fiber. (c) Transmission measurement image of TIR probe fiber in which the transmitted light is scanned by a tapered fiber tip.

to characterize the fiber, however, this allows measuring the transmitted beam shape. We have obtained a beam spot with a quasi Gaussian shape using the transmission map. The spot size is determined to be ~2 μm. The characterized fiber is used for the stable trapping of nanoparticles in water with the single fiber geometry. .

2.4 Data analysis

The characterization of an optical trap is required to quantify the trapping strength. For this analysis, we treat a recorded trapping sequence or video and track the residual Brownian motion of a trapped particle or position fluctuation. We would like to explain our data analysis technique using particle trapping measurements performed with two identical tapered fiber tips. This measurement is used for practicing the trapping experiments on suspension tweezers setup.

In practice experiments, we have trapped a 1 μm spherical polystyrene particle as a function of light power at a fixed fiber-to-fiber distance (D_{f-f}) of 20 μm. Then it is followed as a function of distance at fixed light power 27.7 mW. These trapping measurement videos are recorded using our microscope camera with a typical frame rate of up to 330 fps during the trapping experiments. A standard recorded video contains about 4000-5000 images. We already discussed the importance of a higher frame rate of the trapping videos to determine the high-frequency movement of particles. To track these videos, we have developed a particle tracking algorithm in the Scilab environment that can automatically track the trapped particle from the recorded videos.

In our tracking algorithm, we measure the trapped particle circular bright spot (el-

liptical shape in the case of nanorods) profile in two distinct directions, axial and transverse relative to the fiber axis. These two profiles (in pixels) are fitted with a Gaussian function. The particle position corresponds to a point where the amplitude is maximum. This method is well suited for monitoring an individual particle, and it allows time-dependent position tracking in x-y directions. In the case of nanorods, a time-dependent nanorod angular orientation can be tracked based on their two observed widths.

A 2-dimensional particle position tracking curve is presented in Figure 2.13 (a), which corresponds to a trapping measurement at 27.7 mW light power and for a D_{f-f} = 26.7 μm. The presented tracking curve is one of the best among the other measured traps. It is a bit elongated in the axial direction, however, close to an isotopic trapping potential. A well isotopic trapping potential has been reported for a 1 μm particle using a counter-propagating approach of taper fibers in [2], [18]. The given trap is enough to explain our analysis approach to quantify the trapping efficiency. Figure 2.13 (b) shows a time-dependent position tracking curve in real-time in the axial and transverse direction. Based on the two-dimension position tracking, we used two complementary methods to determine trapping efficiencies, more general the trap stiffness. These two complementary methods are Boltzmann statistics (BS) and power spectra analysis (PSA).

Before discussing these two complimentary approaches, we would like to recall the motion of a trapped particle using the Langevin equation in the presence of a viscous medium, the one-dimensional motion of the trapped particle can be written as [119],

$$m\ddot{x}(t) + \gamma_0\dot{x}(t) + \kappa x(t) = (2k_BT\gamma_0)^{\frac{1}{2}}\xi(t) \tag{2.4}$$

where m, $\dot{x}$, and $\ddot{x}$ are the mass, velocity, and acceleration of the particle, respectively, and $\gamma_0 = 6\pi\eta a$ is the drag or friction coefficient for a spherical particle of radius a in a fluidic medium of viscosity η. On the left-hand side of the above equation, the first, second, and third terms are acting force (Newton's second law of motion), drag force, and restoring force or harmonic force of a trap, respectively. Whereas the term on the right-hand side is the Brownian force of particle at absolute temperature T [2]. The term k_B represents the Boltzmann constant. $\xi(t)$ in Brownian force explains the influence of the thermal noise. The influence of thermal noise can not be neglected, as it tries to push the particle out of the trap, and the optical force pulls it back to the center of the trap.

For the microscopic particles, the particle motion depends on the medium. For example, in liquid, the particle motion is extremely over-damped and its inertial effects which are associated with the mass of particle are negligible[119]. The inertial effect can be quantified using the Reynolds number, Re = $\rho a\dot{x}/\gamma$, where ρ is the density of suspension medium. The inertial effects decay in a very short period of time which is known as momentum relaxation time or characteristic time ($\tau_0 = \frac{m}{\gamma_0}$). For example, in our experiment we used polystyrene particles (1 μm) having a mass ($m = \frac{4}{3}\pi a^3\rho$), where a is radius and ρ is density of polystyrene) of 5.5×10^{-16} kg and its coefficient of friction in water at 20°C is γ_0 = 9.44×10 $^{-9}$ kg/s. The characteristic time for kinetic energy loss is ≈6×10^{-8} s due to the friction. This characteristic time is much shorter than the experimental time resolution at the sampling rate of about 300 Hz. Therefore, we can neglect the first term

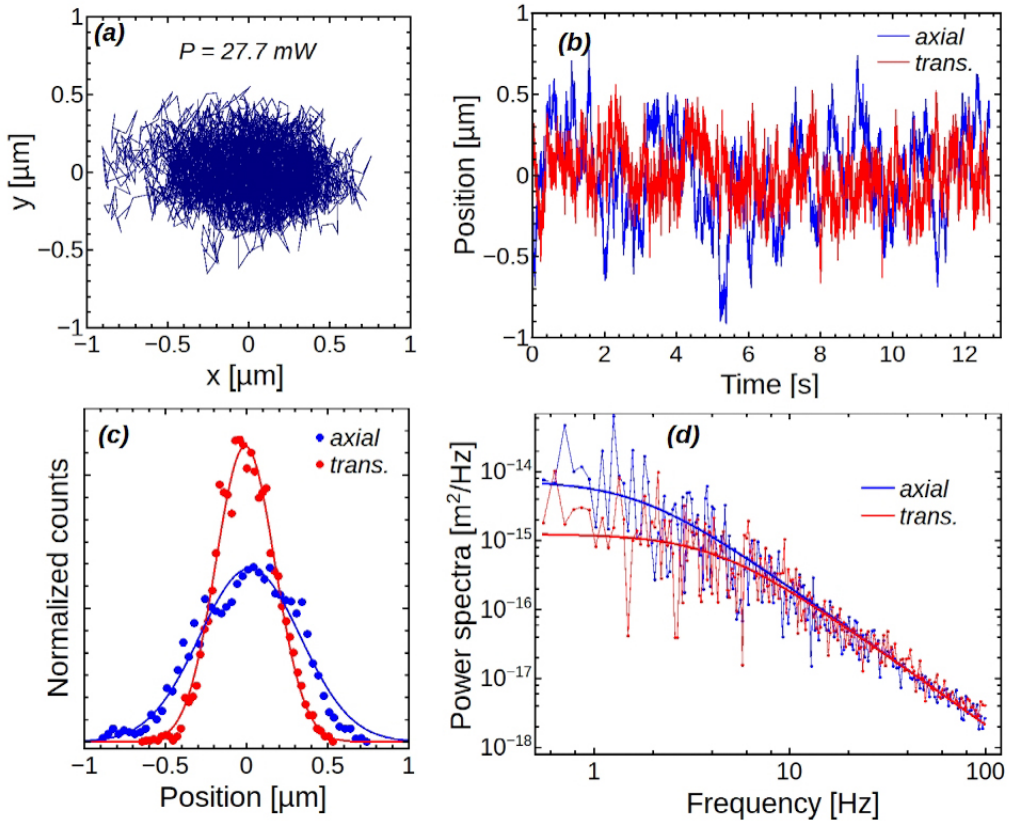

Figure 2.13: (a) A 2 dimensional tracking curve of an optically trapped particle using two identical tapered fiber tips with a light power of 27.7 mW at a D_{f-f} of 26.7 μm. (b) Time-dependent position tracking curve in two directions. (c) The particle position distribution which is obtained using BS and fitted a Gaussian function to determine the trap stiffness. (c) The PSA of trapped particle position fluctuation in the two given directions.

of Equation 2.4 and the system is considered over-damped.

$$\gamma_0 \dot{x}(t) + \kappa x(t) = (2k_B T \gamma_0)^{\frac{1}{2}} \xi(t) \tag{2.5}$$

Following the eq. 2.4 and Figure 2.13, we would like to discuss our approach for determining the trap stiffness of a harmonic trap.

2.4.1 Boltzmann statistics method

The Boltzmann statistics is one of most common method which is used for deducing the trap stiffness (κ). This method is based on the finding the probability density of a particle in a potential well at certain position. This methods uses the equipartition of energy theorem and potential energy ($U(x)$) of a harmonic trap for accounting the trapping strength and can be written as,

$$< U(x) >= \frac{1}{2}\kappa_x < (x - x_0)^2 >= \frac{1}{2}k_B T \tag{2.6}$$

where, x_0 is a mean position of the particle and x is the particle displacement from the mean position. Now considering the equipartition of energy in eq. 2.4, the energy distribution of an optically trapped particle inside the potential well obtained using the Boltzmann statistics as [2],

$$P(x) = \frac{1}{Z}\exp\left(-\frac{\kappa_x(x-x_0)^2}{2k_BT}\right) \tag{2.7}$$

where Z is a normalization factor known as the partition function. For experimental measurements, the trap stiffness can be obtained by fitting a Gaussian function to probability distribution and can be written as

$$P(x) = A\exp(-B\sigma_x^2) \tag{2.8}$$

where $A = 1/Z$, $B = \kappa_x/2k_BT$ and σ_x = x-x$_0$ is a standard deviation function. Then, the trap stiffness can be directly obtained in the given form $\kappa_x = \frac{2k_BT}{\sigma_x^2}$.

Figure 2.13 (c) shows the Gaussian fittings on the position distribution obtained by the Boltzmann statistics in the axial and transverse directions. The κ values are calculated as 0.04 and 0.12 pN/μm in the axial and transverse direction, respectively. Similarly, the κ is obtained for all measurements.

We often use this method to characterize our trapping measurements since it is not only straightforward to determine the κ but also allows visualizing the shape of the trapping potential. The method becomes interesting for a trap with more than one stable trapping position to visualize, however, the related κ is meaningless. It does not require any feature of the trapped particle such as shape, size, refractive index, and viscosity of the surrounding medium.

2.4.2 Power spectrum analysis:

The power spectrum analysis is another widely used method of characterizing the optical trap [119]. This method uses the power spectrum of a signal. The power spectrum of a signal is defined as the magnitude squared of the Fourier transform of the signal divided by the total measuring time. In general, power spectrum is the energy density dived by the frequency of a analog signal ($E = \int_{-\infty}^{\infty}|x(t)|^2dt$).

The power spectrum of an optically trapped particle is obtained by performing Fourier Transform of eq. 2.4. The obtained spectrum has a Lorentzian shape and is described as follows [2],

$$P(f_0) = \frac{2k_BT}{\gamma_0(f_c^2 + f_0^2)} \tag{2.9}$$

where f_0 is the oscillation frequency obtained from Fourier transform and $f_c = \frac{\kappa}{2\pi\gamma_0}$ is the corner frequency, the ratio of trap stiffness and friction coefficient. Considering these frequencies, the power spectrum distinguished into two regimes:

Case 1 : When the corner frequency is higher than oscillation frequency, ($f_0 << f_c$) which means that the Brownian motion of a particle get restricted by the optical force responsible for the trapping. In this case, the eq.2.4.2 follows as

$$P(f_0 << f_c) = \frac{8\pi^2 k_B T \gamma_0}{\kappa^2} \tag{2.10}$$

The power spectrum becomes constant and is inversely proportional to the square of κ.

Case 2 : When the oscillation frequency dominates over the corner frequency ($f_0 >> f_c$), which means that Brownian motion leads the power spectrum and no more dependent on trap stiffness. In this case, the eq.2.4.2 follows as

$$P(f_0 >> f_c) = \frac{2k_B T}{\gamma_0 f_k^2} \tag{2.11}$$

i.e., the power spectra is fully explained by using the oscillation frequency and it is no more dependent on κ.

Figure 2.13 (d) shows the power spectra of trapped particle position fluctuation in the axial and transverse directions at 27.7 mW and a D_{f-f} of 16 μm. Through this analysis, the κ values are calculated as 0.06 and 0.18 pN/μm in the axial and transverse direction, respectively. These values correspond to the corner frequencies (f_c) of 1 and 3 Hz in the given two directions. These two values also estimated by visualizing the power spectrum, which corresponds to the transition curvature between the two planes. Thus, the κ value for all measurements are obtained using this method.

Moreover, this method has the advantage of verifying the calculated κ as it allows us to calculate the temperature and radius of the trapped particle based on the fitted free parameters. This feature makes it more reliable.

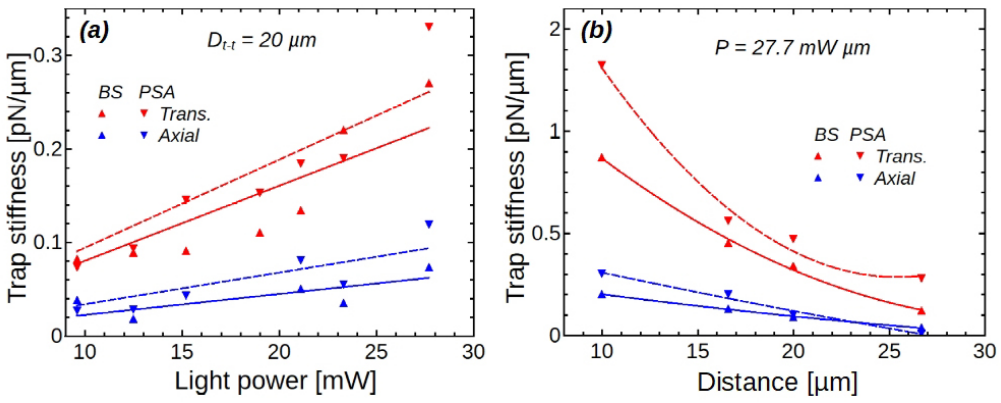

Figure 2.14: A plot of κ as a function of (a) applied light power (b) fiber-to-fiber distance (D_{f-f}).

2.4.3 Trapping efficiency analysis

The κ, which is obtained by employing the above two methods (BS and PSA), are plotted separately as a different light powers and then at different distances at a light power 27.7 mW (Figure 2.14 (a) and (b), respectively). An agreement is observed for κ values obtained from the above analysis. The normalized trapping stiffness ($\tilde{\kappa}$) is obtained by fitting a linear slope. For a power-dependent measurement, a linear dependency of κ is observed on the light power. Their $\tilde{\kappa}$ values are 8.0 and 9.4 $pN \cdot \mu m^{-1} \cdot W^{-1}$ in transverse direction for BS and PSA respectively. Similarly, in the axial direction, these values are determined as 2.3 and 3.4 $pN\mu m^{-1}W^{-1}$ for BS and PSA, respectively. The $\tilde{\kappa}_{Trans.}/\ \tilde{\kappa}_{Axial}$ ratios are observed as 3.5 and 2.8 for the BS and PSA methods, respectively.

The κ values for the measurements as a function of the D_{f-f} between the tips (Figure 2.14 (b)). These values have appeared higher when the distance is closer. It is measured as 0.87 $pN \cdot \mu m^{-1}$ for a $D_{f-f} = \sim 10$ μm using BS and further it reduces with a factor of $1/D_{f-f}^2$.

The presented values are found in good agreement with previously reported work [2]. The results show that these methods are very in order to characterize our experimental measurements, which is discussed in chapter 4. These studies also allow us to understand the experimental tweezers setup and optical trapping experiment as a beginner.

2.5 Conclusion

We have explained our two experimental setups aimed for optical trapping experiments in air and suspension (water). First, fibered air-tweezers setup, which is currently being developed, has been discussed with the primary approach to developing this setup, especially the trapping chamber. Our other tweezers setup which is excellently working for the particle trapping experiments in suspension, has been discussed with our approach to measure emission spectroscopy of the optically trapped luminescent particles.

We have discussed the fabrication and emission properties of five different micro and nanostructured fibers. These are presented here in the prospect of their implementation for trapping experiments on these tweezers setups. The TIR-probe fiber is explicitly designed for particle trapping in suspension.

Finally, we have discussed two complementary methods: BS and PSA, to quantify the trapping efficiency of our experimental observation and reliability on values deduced by these methods. Further, these complementary approaches allow us to study the trapping behaviors of anisotropic nanoparticles.

Chapter 3

Optical manipulation in air

Introduction

This chapter is focused on experiments performed for the development of air-tweezers setup. Firstly, we present optical manipulation experiments using a single optical fiber for studying the influence of light beam on a particle in air. These measurements include the demonstration of water-aerosol droplets manipulation, which is performed in the initial stage. Further, particle manipulation is sequentially studied using the three different optical fibers. Finally, we present numerical simulation performed to understand and interpret the obtained experimental manipulation results.

3.1 Optical manipulation

In the previous chapter 2, we have presented a trapping chamber development for the particle trapping experiments in air. The basic idea for this experimental development is to trap a single airborne nanoparticle a single fiber and dual fibers tweezers approach. Figure 3.1 represents the schematics of particle manipulation experiment with three steps, which is followed initially to study and characterized our experimental setup. First, we observe free-falling particles using our microscope in front of the fiber tip. Then we apply a light beam on these particles and, finally, observing the influence of light beam on them.

The optical manipulation observation has been recorded with a typical frame rate of about 100 fps. Then recorded videos are treated to determine a time-dependent trajectory of the droplet. It has already been said that we have used a manual track to observe the particle's position using the observation video in the Image J program. Then, we use this data to calculate the droplet speed and related optical force using a homemade algorithm dedicated to optical force measurement. This algorithm is based on the Langevin equation of particle motion and allows determining the optical force. This equation can

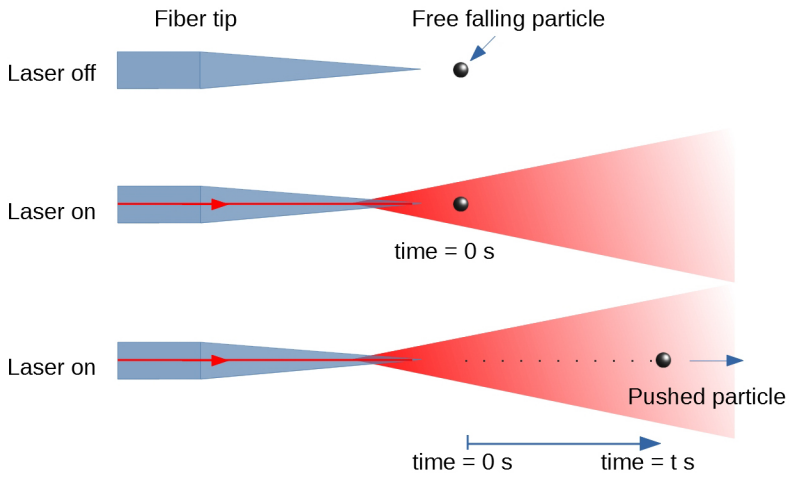

Figure 3.1: Schematics of optical manipulation experiment using a single tapered fiber tip.

be given in terms of Stokes coefficient ($\gamma_0 = 6\pi\eta a$) for air medium as [103],

$$F_0 = m\ddot{x}(t) + (6\pi\eta a)\dot{x}(t) \tag{3.1}$$

where m is the particle mass, η is the medium viscosity, a is the radius of particle, $\dot{x}(t)$ and $\ddot{x}(t)$ is the particle speed and acceleration, respectively. For a water-aerosol droplet diameter of 2.8 μm, mass is calculated as $m = 1.15 \times 10^{-14}$ kg (with water density $\rho = 997$ kg·m^{-3}) and Stokes coefficient as $\gamma_0 = 4.9{\times}10^{-10}$ kg·s^{-1} (with air viscosity $\eta = 18.6{\times}10^{-6}$ kg·(m.s)$^{-1}$ at 25°). For a polystyrene particle, $m = 5.5 \times 10^{-16}$ kg (with polystyrene particle density $\rho = 1.05{\times}10^{3}$ kg·m^{-3}) and $\gamma_0 = 1.75{\times}10^{-10}$ kg·s^{-1}.

3.1.1 Tapered fiber tip

Droplets

In the primary stage, we initiate our experiment using simple distilled water-based aerosols droplets and a tapered fiber tip. We choose to start with these droplets because they are simple to use and do not require any sealed or closed environment, unlike nanoparticles. Also, no special equipment for health protection is needed. Considering the preliminary stage of experiments, it is beneficial to start with simple equipment having a low cost.

We inject the aerosol into the trapping chamber by following the procedure explained in section 2.1. We switch on laser once we observe a few free-falling droplets in front of the fiber tip. In the first step, it observes that droplet sizes are reducing and evaporating rapidly in light. It has been known from D.R. Burnham's work that salt can be used to increase the surface tension of the droplets and enhance the relative moisture inside the trapping chamber [73]. Therefore, we have suspended edible salt (100 μg) to distilled water (10 ml) and sonicated for a few minutes. Then this mixture is used for

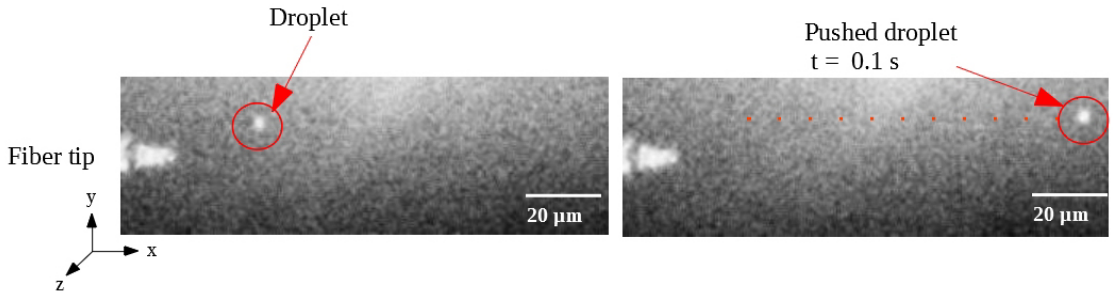

Figure 3.2: The microscopic image of the manipulated of a droplet at the light power of 2.5 mW using the tapered fiber tip.

generating the aerosol droplets. Initially, we also observe that free-falling droplets are attracted to fiber tip due to adhesive forces. So, we use a wire to earth the fiber tip, which allows the discharging of its electrostatic charge.

The first droplet manipulation is observed at a light power of 2.1 mW. On applying the light beam on the droplets, we observed that the droplet is strongly propelled in the direction of light propagation. We record this observation video, and then, this measurement is repeated on several droplets at the same power. Further, the droplet manipulation experiment is studied as a function of light power by varying the power from 0.05 mW to 3.5 mW in several steps. The influence of light beam on a droplet at 2.5 mW can be observed in Figure 3.2.

From the first observation at 2.1 mW, it is observed that the droplets are not pulled or attracted towards the beam center, i.e., the region of higher intensity. In figure 3.3 (a) shows the x-y trajectory of a pushed droplet after experiencing an optical force due to the light beam. The optical force experienced by the droplet at each position is separately measured in axial (x) and transverse (y) direction using the algorithm on Langevin equation 3.1. An arrow (not very well visible) shows the position and the direction of the pushed droplet. A visible range color map shows the magnitude of optical force with dark red as maximum force and dark blue as the minimum.

The droplets have experienced a very high optical force in the axial direction force compared to the force in the transverse direction. Also, the droplets are not pulled by the optical force into the beam center. However, the maximum optical force is estimated to be 3.6 pN near to the fiber tip, which can be identified with red arrows in the given figure. The pushed droplets' trajectory length depends on the distance between the fiber tip and the initial droplet position. It has also been noticed that the droplets are pushed at an angle that can be related to the divergence angle (20°) of the beam.

Figure 3.3 (b), shows the measurements studied as function of light power. These measurements reveal that the optical force experienced by droplets are increasing with increased light power. Also, it influences the pushed droplet trajectories length as the highest power appears with a larger trajectory. In this case, the maximum optical force is estimated to be 5.5 pN at a distance of about 10 μm from the fiber tip.

The analyzed result suggests that the presence of high optical force in axial direc-

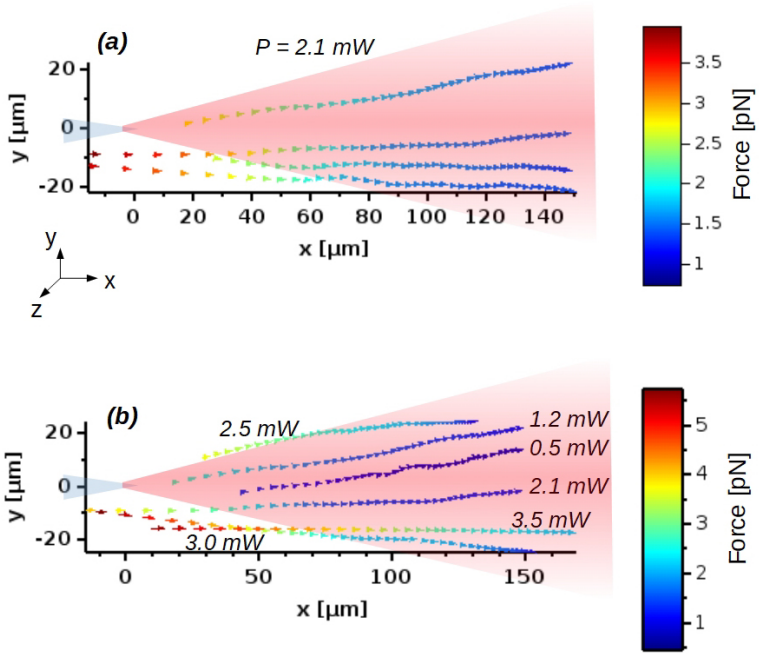

Figure 3.3: (a) The trajectories of the pushed droplets under the influence of laser beam at 2.1 mW. The coordinate (0,0) shows the point of the fiber tip apex. The dark red and dark blue colors are representing the maximum and minimum optical force experienced by the droplets. (b) The trajectories of the droplets at different light powers.

tions leads to pushed droplets strongly and unable to attract them towards the beam center. These experimental measurements provide an approximate idea about the optical forces experienced by the droplets. In principle, It is expected that the droplets should be attracted to the high gradient region for stable optical trapping. However, after this experiment, we found the salt precipitation on the tip surface. This precipitation also affects the light emission property of the fiber tip.

Particles

Further, we use the polystyrene particles of 1 μm for optical manipulation. The particle manipulation is studied using a new tapered fiber tip by replacing the old one. These particles are injected into the trapping chamber with ethanol aerosol as per the procedure explained in the last chapter 2. After the quick evaporation of ethanol aerosol, the particles are easily observed falling due to gravity with Brownian motion. Once particles are observed, we instantly switch on the laser, like the previous experiment.

On applying a light beam with a power of 12.7 mW on the particles, we observe that the light beam is strongly pushing these particles away from the beam center in the transverse direction (Figure 3.4). However, this measurement is repeated to observed the influence of the light beam on the particles. The observation videos are recorded at different light power ranging between 5 mW and 30 mW.

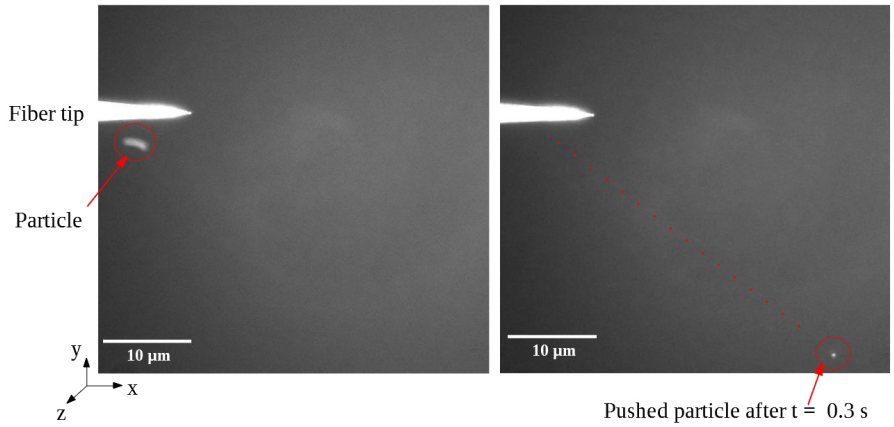

Figure 3.4: The microscopic image of manipulated particle at 12.7 mW. The particle trail appears due to the high speed of the particle near to the fiber tip.

The particle trajectories corresponding to different light powers can be seen in Figure 3.5. It can be clearly observed that the trajectories of the particles depend on light power, as the trajectories appear longer on higher light power. It suggests that the optical force experienced by the particles is highly influencing in axial direction. In this measurement, the particles did not pull into the beam waist, and they are further moving away from beam center. However, the maximum optical force is estimated to be 0.27 pN at a light power of 30.9 mW for the closet position to the fiber tip. However, moving away from fiber tip, the optical force is decreasing gradually. In this case, the attracting force due to the light beam is less than that of the pushing force.

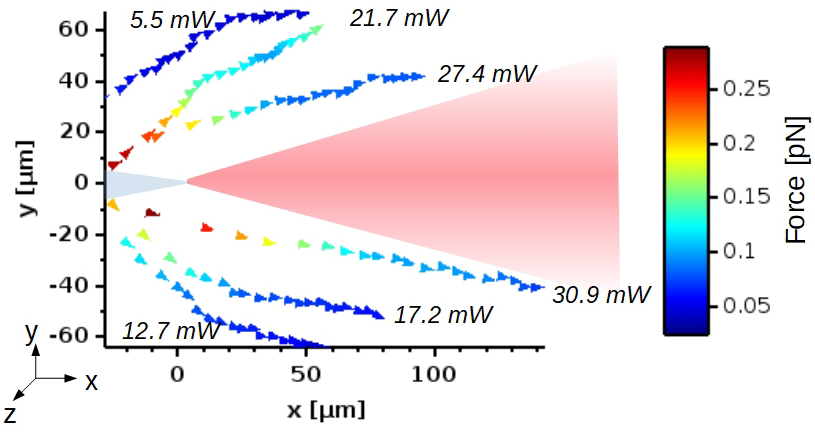

Figure 3.5: (a) A 2D plot of the trajectories of pushed particles under the influence of different light powers.

The particle manipulation experiments show that particle trapping is not possible by employing this fiber. The critical problem behind the trapping is that the particles are not attracted to the light beam waist. The particles are mostly pushed away from the beam center with an angle more than the beam diverging angle. Comparing to previous work on trapping in water with the same particle and fibers [2], they reveal a completely

different story for experimental measurement in air. However, the experienced optical forces have appeared comparatively lesser than the previous one measured in suspension. Therefore, we have decided to use a different approach, such as a less diverging beam for our next measurements.

3.1.2 Negative axicon fiber:

In the last experiment, we have observed that optical manipulation with a diverging fiber is challenging. For further measurement, we choose a negative axicon fiber that emits a less diverging beam. As we have seen in the previous chapter 2 that the central spot of this fiber is diverging with a small angle of about 3.2°.

Initially, the visualization of particles is difficult due to the broad aperture of the fiber, i.e., to find a particle at the axial center of the fiber. The particles are injected into the chamber using the same procedure as the previous experiment. When we apply a light beam with 1 mW power, we have observed particle is pushed axial direction. However, after this moment, we do not observe any falling particle or influence at our microscope focus. Then we further move vertical direction above the fiber axial center. At the height of 70 μm, we observe that some particles are influenced and moving axial direction with Brownian motion. This influence can be attributed to the rings of the beam produced by this fiber. However, for our experimental analysis, we have recorded the videos of particle manipulation at different light powers.

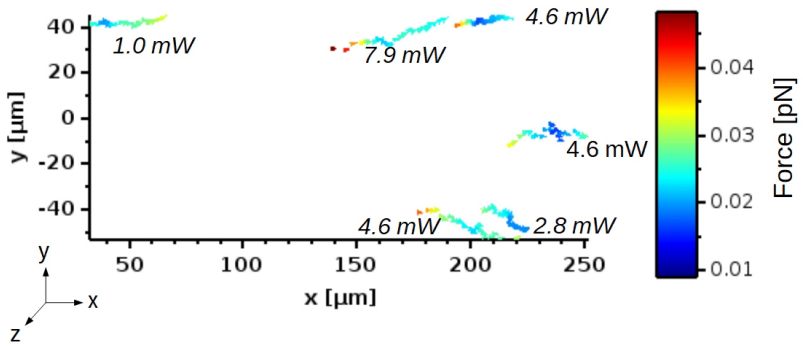

Figure 3.6: A 2D plot of trajectories of particles which are pushed under the influence by light beam emitted by the negative axicon tip.

The influence of the light beam on the particles can be seen in Figure 3.6. It is observed that the particles are pushed by beam over a broad region of ≈50 μm either side of the tip center. The maximum optical force is determined as 0.048 pN at 7.9 mW light power. The optical forces are observed depending on the laser powers. The higher light power influences the particle, which leads to a long trajectory.

The particle manipulation observed using the negative axicon does have any significant influence. It is even worse than the taper fiber tip, and there are difficulties in particle visualization and the influence of rings of the light beam. Therefore, we have dropped this fiber for the particle manipulation experiment and choose a less diverging

fiber, which is the positive axicon fibers.

3.1.3 Positive axicon fiber

The positive axicon fiber tip has been chosen because it produces a least diverging beam. At first, the manipulation experiment is performed using a single positive axicon fiber. The series of measurements is first performed at a light power of 10.8 mW. It is observed that the light beam strongly pushes the particles in the direction of light propagation, and the trajectories of the pushed particle are presented in Figure 3.8 (a). The influence of optical force decreases when particles are moving away from the fiber axicon. The maximum optical force experienced by the particles is determined to be 0.4 pN at a distance of 10 μm away from the fiber axicon.

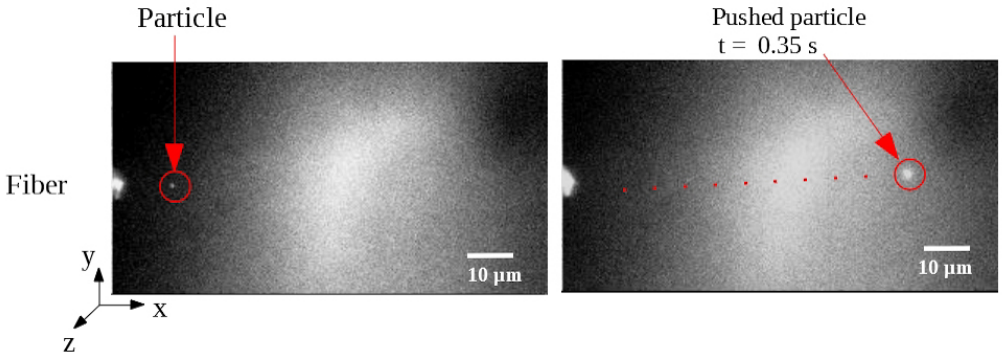

Figure 3.7: The particle manipulation under the influence of the laser beam which is produced by a positive axicon fiber at a light power of 10.8 mW.

Further, a series of manipulation measurements are recorded at different light power from 3 mW to 16.5 mW to investigate the impact of power. The trajectories of pushed particles at different light power can be seen in Figure 3.8 (b). The optical forces are observed to depend on the light powers as it increased with increasing light power.

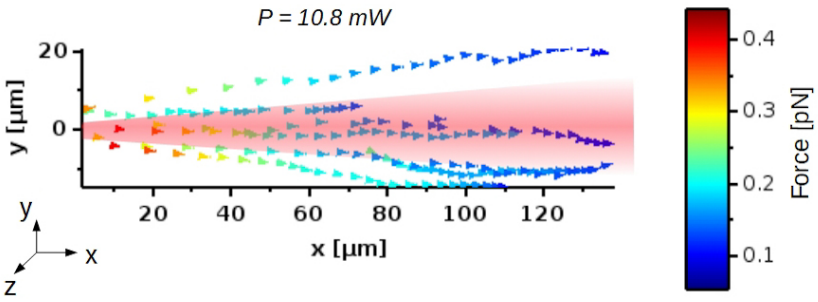

Figure 3.8: The 2D trajectories of particles under the influence of light beam emitted by the positive axicon tip at 10.8 mW.

The demonstration of particle manipulation using the positive axicon fiber has shown that the particles have not been influenced along the beam gradient. Also, they still experience the higher optical force in the axial direction compare to the transverse direction.

It has also appeared that these particles are being pushed through a narrow-angle very lower compared to tapered fiber tip manipulation. At this stage, we have made an effort to trap these particles using the counter-propagating approach. However, due to the high scattering force, particles have been pushed by both fibers but have not trapped, or not for even while. Therefore, we have stopped our experimental measurements and performed the theoretical analysis to find out the real problem.

3.2 Numerical simulations

The experimental measurements have shown that the air-tweezers setup is not very well working for particle trapping, since the particles are pushed by the optical force away from the beam center in the transverse direction. It is known from experimental observation that the optical force is unable to pull the particle into a high gradient region. To understand our experimental observation, we have been performed numerical simulations. We have used a homemade program that is developed in the Sci-lab environment for this simulation. The simulation is performed considering the parameters observed for light beam emission of tapered fiber tip and 1 μm polystyrene particle [2]. For this simulation, first, we calculate the electric field of light beam considering a Gaussian beam and then use the Rayleigh approximation. For calculating the electric field in terms of r as the radial distance from the axial center of beam and z be an axial distance from the beam, the equation can be given as [120],

$$E(r,z) = E_0\hat{x}\frac{w_0}{w(z)}\exp\left(\frac{-r^2}{w(z)^2}\right)\exp\left(-i\left(kz + k\frac{r^2}{2R(z)} - \psi(z)\right)\right) \tag{3.2}$$

where, E_0 is the electric field at origin (0,0), i is the imagenary unit, k is the wave number ($= 2\pi n/\lambda$, λ is light wavelength and n be the medium's refractive index), w_0 is the radius at beam waist, $w(z)$ is beam waist along z-direction where field is decreasing by a factor of $\frac{1}{e^2}$, $R(z)$ is the radius of curvature and ψ is the Gouy phase at z. The E_0 has been calculated from the beam intensity ($I = cn\epsilon_0|E|^2/2$), based on the experimentally measured light power ($P = \int I \cdot dA$, where dA is a differential closed surface of the laser beam). The parameters, which are used in the simulations are: $E_0 = 1{\cdot}10^6$ W$\cdot$m^{-1} (which corresponds to a light power of ~4.1 mW), $\lambda = 808$ nm, $n = 1$ for air, $w_0 = 1$ μm, and particle size a=0.5 μm [2], [3].

Further, the application of dipolar approximation in Rayleigh regimes allows deducing the optical force in transverse and axial directions. This approximation helps to avoid the rigorous mathematical calculations and straightforward. It is also very well known that the optical force experienced by a trapped particle in this regime is a combination of two forces called scattering and gradient force.

Figure 3.9 (a) and (b), respectively, show the simulated scattering force map, which has been experienced by the particle in both axial and transverse directions, represented by x and y, respectively. This force has appeared higher in the axial direction as compared to the transverse one. Also, it is higher near the tip apex about 34 pN but decreases while moving away from the tip. In Figure 3.9 (c), the influence of scattering force can be

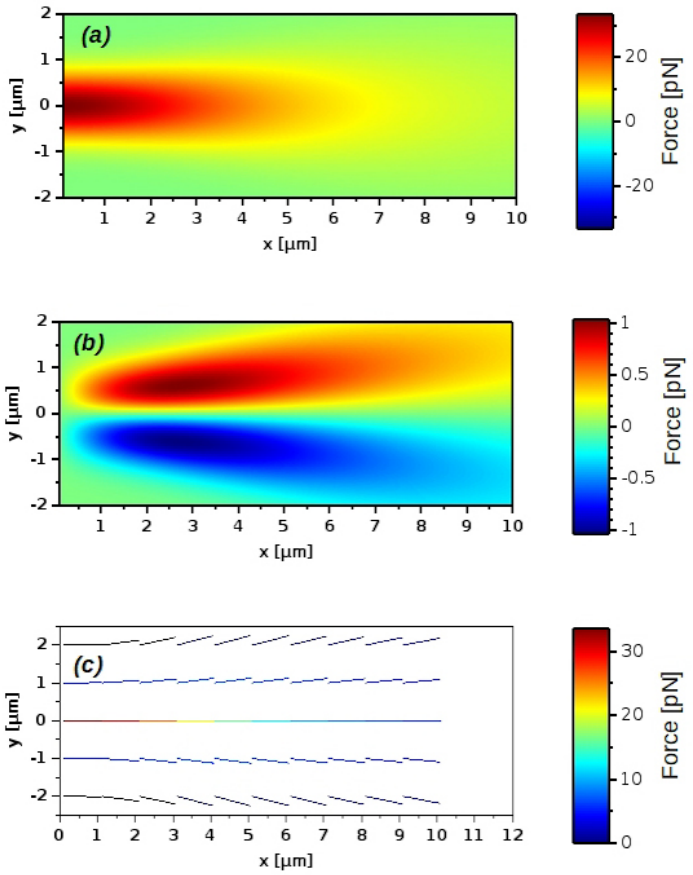

Figure 3.9: The scattering force obtained through the simulation (a) axial direction and (b) transverse direction. (c) The simulation of the scattering force experienced by the particles under the influence of the laser beam.

observed on a particle as it pushes the particle strongly away from the fiber tip in the axial direction.

Similarly, the gradient force is also calculated in both x and y directions, which has been presented in Figure 3.10 (a) and (b). The gradient force has appeared very lower as compared to the scattering force (Figure 3.10 (c)). The maximum gradient force has appeared near to tip about 15 fN. Thus one can observed that the optical force in transverse direction is almost negligible. Therefore, the particles are unable to be attracted by the light beam toward the beam center.

This simulation have confirmed the dominance of the scattering force over the gradient force, causing strong pushing of particles in the axial direction, which has been observed in experimental measurements. Also, it shows that the optical force in transverse direction does have much impact on the particles. In general, this study shows the real challenges of optical trapping in air using a diverging beam producing fibers. In such a condition, we are looking to use other structured optical fibers, producing other than the diverging light beam.

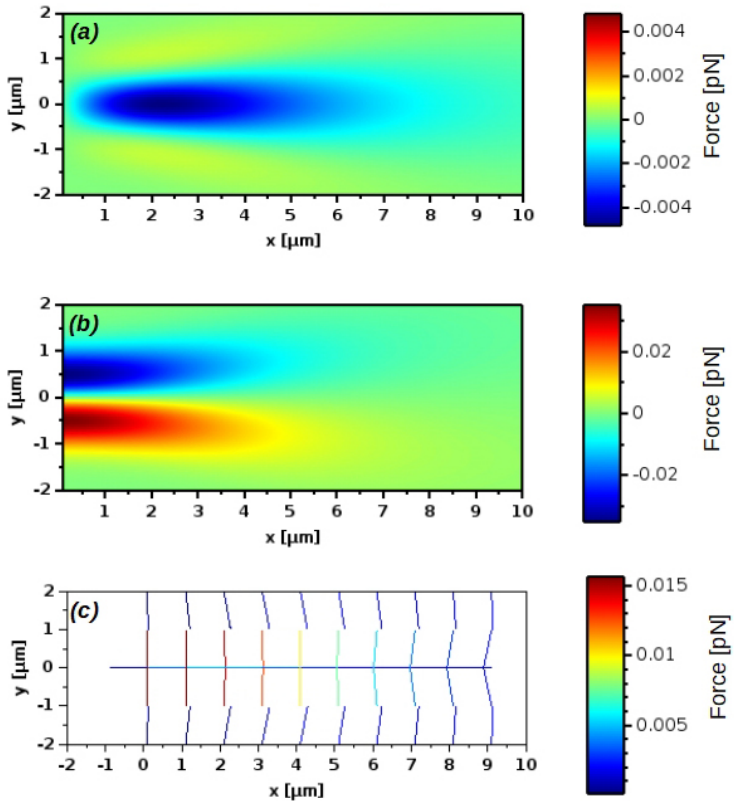

Figure 3.10: The simulated gradient force using the simulation in (a) axial (x) direction and (b) transverse (y) direction. (c) The simulation of the gradient force experienced by the particles due to the laser beam.

3.3 Conclusions

A newly developed fibered air tweezers setup is employed to study particle manipulation with a single fiber tip. The influence of the laser beam on the droplets and particles is studied separately using three distinct fibers. Firstly, manipulation using the tapered fiber tip has reveled that the droplets and particles are not attracted to the beam center and also strongly pushed in the light propagation direction. The negative axicon fiber is also unsuccessful in manipulating the particles since a significant problem appeared due to rings of the beam. In the case of positive axicon fiber, the particles are efficiently pushed in the axial direction but without getting pulled towards the beam center. Numerical simulations have been performed to understand the results observed with the experimentally and are coherent with this measurement. This simulation has revealed the real difficulties found in trapping in air.

Chapter 4

Optical trapping in suspension

Introduction

In this chapter, we present the optical trapping of micro and nanoparticles using a suspension tweezers setup employing different micro-structured optical fibers. This chapter is divided into three parts based on the particles of interest that are used for studying the trapping events. In the first part, we discuss the trapping measurements by employing two different 3D optical fibers; Fresnel lens and TIR-probe fibers. In the next part, we have focus on the application of tapered fiber tip and Fresnel lens fibers for studying optical trapping and spectroscopic investigation of Eu-doped nanorods. Finally, the last part shows the application of Fresnel lens fibers for optical trapping of $CsWO_3$ nanoparticles.

4.1 Trapping of polystyrene particles

4.1.1 Fresnel lens fibers

1 μm spherical particle

In chapter 2, we have briefly introduced the fabrication and characterization of Fresnel lens fibers with three different N.A. of 0.3, 0.5, and 0.7. These fibers are sequentially implemented for the optical trapping of polystyrene particles (1 μm in diameter), which allows studying their trapping performance in suspension. In this process, two identical fibers with the same N.A. are aligned in a counter-propagating geometry so that they can transmit a maximum intensity to each other and create an optical trap by cancelling their radiation pressure at an equilibrium point (4.1(a)).

We begin trapping experiments with the fibers having N.A. =0.3. In the present case, we observe the particle trapping at a fiber-to-fiber distance (D_{f-f}) of 385 μm, which

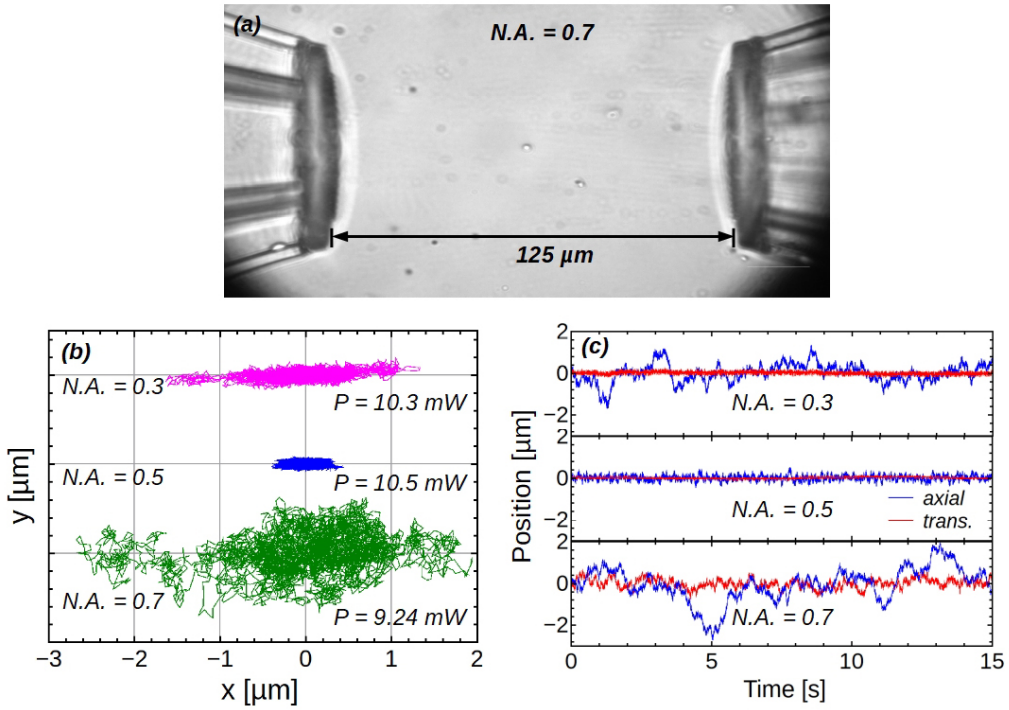

Figure 4.1: A microscopic image of a particle trapping using the counter-propagating beams of Fresnel lens fibers of 0.7 N.A. (b) A x-y trajectory of trapped particles observed using the three fibers different of N.A.= 0.3, 0.5, and 0.7, respectively. (Here, y-and x-axis has similar axis values.). (c) The time dependent position tracking curve corresponds to transverse and axial directions.

is corresponding to twice of their focal lengths. For such a large distance, the trapped particles appears as small bright circular spots in the bright-field microscopy mode. Also, it is not possible to observe the two fibers with this distance in a microscopic image. Thus, we could only record the video of bright spots (particles).

The particle trapping has been studied at different light powers (from 24.2 mW to 3.9 mW) varying in a controlled manner. Here, we would like to mention that the used light power is the total output of fiber measured in air. Subsequently, we use the fibers with N.A. of 0.5, which allows measuring the trapping performance of particle at a (D_{f-f}) of 195 μm by varying the light power from 10.5 mW to 0.21 mW in several steps. In the case of 0.7 N.A. fibers, the particle trapping is observed at 125 μm and studied by varying the power from 25.7 mW to 9.24 mW. For this trapping distance, two fibers could be visualized in microscopic images along with a trapped particle.

In these experimental observation, one can easily observe the differences between these fibers based on the trapped particle movement. The most stable trapping events have been observed using the fibers having 0.5 N.A. They have allowed us trapping the particle even at a very low power of 0.21 mW. It is the lowest trapping light power at which we have demonstrated a stable particle trapping until now.

Subsequently, we characterize trapping videos to obtain x-y tracking and time-dependent

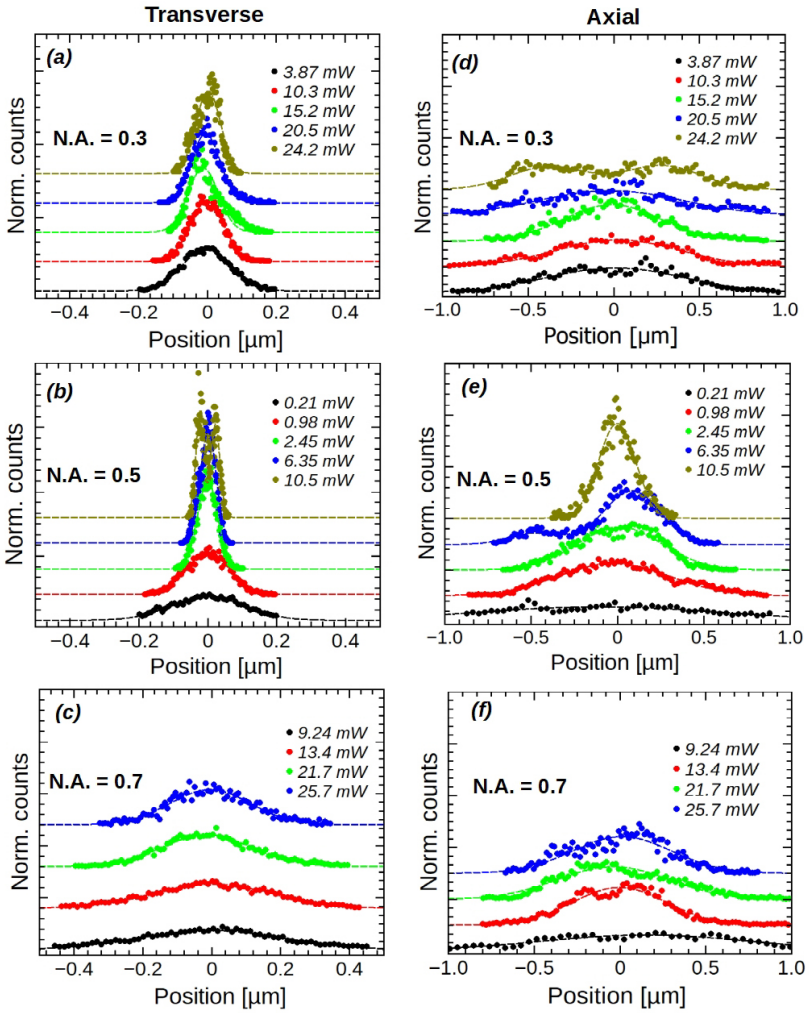

Figure 4.2: Position distribution of optically trapped particles using three different fibers with 0.3, 0.5, and 0.7 N.A. using BS method in (a), (b), (c) for transverse and (d), (e), and (f) for axial directions. The dashed lines represent the best Gaussian fits to the position distribution.

position (Figure 4.1 (b) and (c)), for all three types of fibers. These tracking curves have revealed an anisotropic trapping volume for all three types of fibers. For example, the most efficient effective tracking curve is observed using 0.5 N.A. fibers. It has a smaller confined trapping volume which increases on lowering the light power. It also appears relatively elongated in the axial direction. For the fibers having 0.3 N.A., the trapping volume is much larger, and it further increases for 0.7. The trapped particles show a non-uniform movement in the axial direction with a relatively high oscillation frequency. Also, they are more confined in the transverse direction.

The position distribution of the trapped particles is obtained independently in the transverse and axial directions using the BS method. Figure 4.2 shows the obtained position distributions, which are studied as a function of light power. The distribution is very wide in the axial direction and narrow in the transverse direction. By fitting a Gaussian

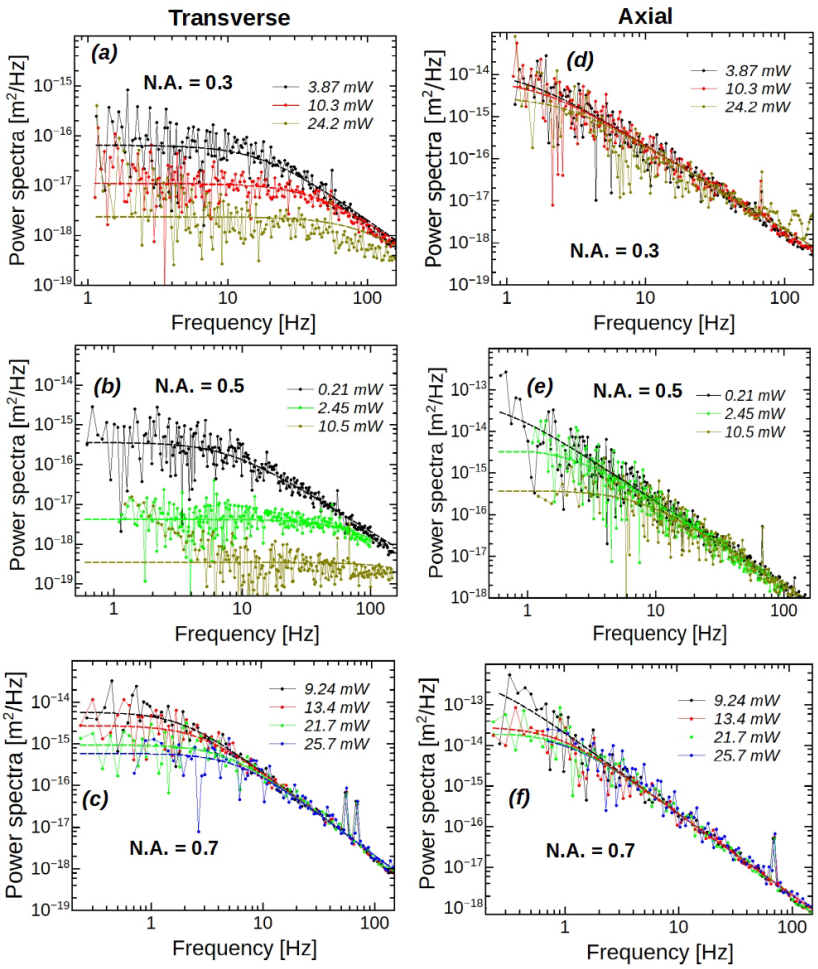

Figure 4.3: PSA method to obtained κ values for all three types of fibers. (a), (b), (c) for transverse and (d), (e) and (f) for axial directions, respectively. The dashed lines indicate the best Lorentzian fitting curves. A peak at 67 to 68 Hz results from the mechanical vibration of the visualization system but it does not have any significant influence on trapping results.

function to the distribution, trap stiffness (κ) can be deduced in both directions. It can be noticed that on lowering the power, the distribution width increases, and therefore κ decreases. Also, in few cases such as the measurement at 10.5 mW using the 0.5 N.A. fibers, the particle is confined with two meta-stable trapping positions in the transverse direction due to a slow mean trapping position shift. In this case, the position distribution is fitted with two Gaussian peaks, and thus, κ does not have any meaningful value. Also, a fewer measurements (e.g., 24.2 mW for N.A. 0.3, 6.35 mW for N.A. 0.5 and 21.7, and 25.7 mW for N.A. 0.7) in the axial direction, are also observed with two meta-stable positions.

Applying the PSA method, κ values are calculated for all three types of fibers at different light powers. In the axial direction, a good agreement between experimental results and fitting model can be noticed in Figure 4.3. However, in the transverse direc-

tion, this fitting model does not fit well for the measurements at higher light power (e.g., 24.2 mW for N.A. 0.3 and 10.5 mW for N.A. 0.5). In these measurements, it can also be noticed that below 10 Hz, the power spectrum increases with decrease in frequency, which is caused due to the slow mean trapping position shift. In this case, the κ values are not accounted to determine the trapping efficiency.

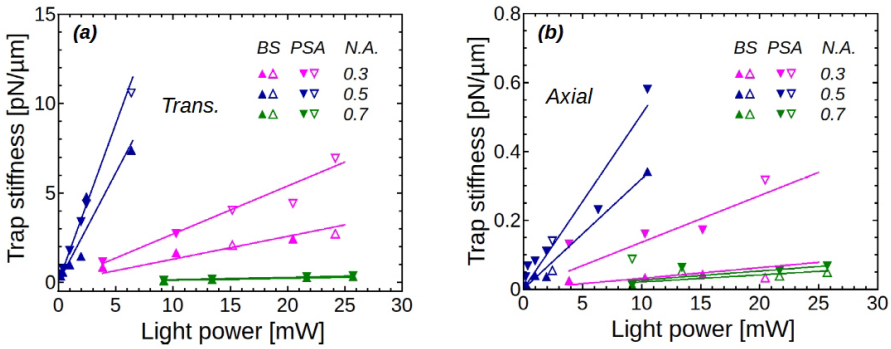

Figure 4.4: Trap stiffness in (a) transverse and (b) axial directions, which have been calculated using the BS and PSA for three fibers with 0.3, 0.5, and 0.7 N.A. at different light powers. The filled-in symbols represent values with a confirmed fit while hollow symbols represent the values of non-confirmed fits.

To determine trapping efficiency, we plot κ as a function of light power for all the three types of fibers. Figure 4.4 shows a comparison of trapping efficiencies measured using the different fibers independently in axial and transverse directions. The normalized $\tilde{\kappa}$ values, deduced using the BS and PSA methods, have been presented in Table 4.1. One can observe the difference between the κ values obtained by BS and PSA methods. This discrepancy can be accounted using two reasons: first, the appearance of two metastable positions in BS and second, values at higher light power are not coherent with the fitting in PSA, especially at the higher light power. In both the scenarios, the κ values have been underestimated. Also, we have neglected lower frequencies during the PSA fittings. Therefore, it has resulted in higher κ values than the ones calculated by the BS method.

Table 4.1: Trapping efficiency of the fibers with three different N.A. are listed in terms of the normalized trap stiffness ($\tilde{\kappa}$) in (pN·μm^{-1}·W^{-1}) which separately calculated using the BS and PSA methods (NA: numerical aperture of the Fresnel lens, D_{f-f}: fiber-to-fiber distance, $d_{particle}$: particle diameter)

NA	D_{f-f} (μm)	$d_{particle}$ (μm)	$\tilde{\kappa}_{trans.}$		$\tilde{\kappa}_{axial}$	
			BS	PSA	BS	PSA
0.3	385	1.0	127.7	268.2	3.1	13.5
0.5	195	1.0	1217.6	1762.9	31.3	50.5
0.7	125	1.0	10.5	13.3	1.9	2.6
0.5	195	0.5	34.9	28.2	2.1	3.2

We have observed the highest trapping efficiency using 0.5 N.A. fibers with $\tilde{\kappa}$ = 1763 pN.μm^{-1}·W^{-1} in transverse direction. Compared with similar measurements that have been previously performed using the tapered fiber tips [2] and nano-antennas (which

generate quasi Bessel beams) [114], the presented $\tilde{\kappa}$ values are 30-50 times higher. In the case of fibers with N.A. = 0.3, the trapping efficiency is lower than N.A. = 0.5., however, their trapping performance for such a large D_{f-f} of ~395 μm is interesting for the far-field trapping applications. Finally, the least trapping efficiency is observed for fibers having N.A. = 0.7. Low trapping efficiency of N.A. 0.7 fibers can be accounted for using their fabrication structure and the alignment of the doublet lenses.

Based on the optical trapping using the Fresnel lens fibers with three different N.A., we choose the most efficient fibers for further trapping applications. Also, their implementation in our experimental setup is very easy.

Trapping of particles with a diameter of 0.5 μm

In the further experiment, we have chosen to trap a polystyrene particle with a diameter of 0.5 μm using the fibers of 0.5 N. A. A particle is stably trapped at a light power of 27.75 mW. However, it leaves the trap if the light power is decreased. This occurrence has been confirmed based on several observations.

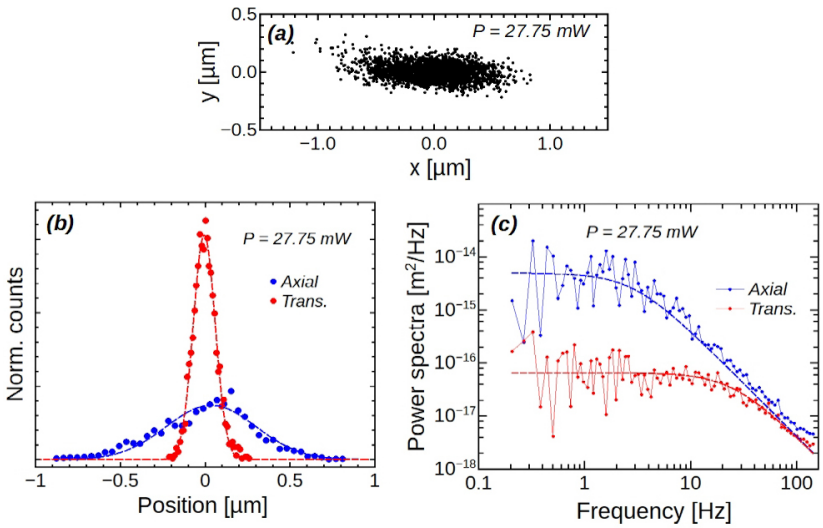

Figure 4.5: (a) Tracking curve of a trapped particle with a size of 0.5 μm. (b) Position distribution in axial and transverse direction. The dashed lines are the best Gaussian fits. (c) PSA fitting curves in axial and transverse direction. The dashed line are the best Lorentzian fits.

The x-y trajectory of trapped particle can be observed in Figure 4.5 (a), which also shows an anisotropic trapping volume. The particle is efficiently confined in the transverse direction compare to axial one. The application of BS and PSA allow calculating the normalized $\tilde{\kappa}$ independently in the transverse and axial directions (Figure 4.5) (b) and (c), respectively. The measured $\tilde{\kappa}$ value is determined using the PSA as 34.9 and 3.2 pN·μm^{-1}·W^{-1} in transverse and axial directions, respectively. The obtained values which determined by these two methods are listed in Table 4.1 and have appeared with a good agreement and it is higher in the transverse.

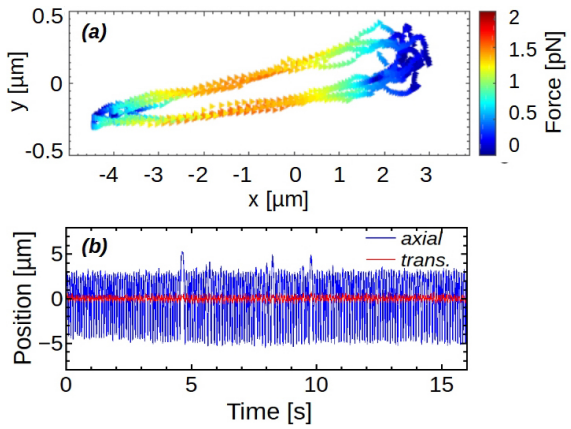

Figure 4.6: Oscillating movement of 0.5 μm diameter particle in the dual-fiber trap with slightly misaligned fibers. The trapped particle oscillates at about 10 Hz in a slightly tilted elliptical orbit with axial and transverse amplitudes of 3.5 and 0.3μm, respectively.

During this trapping experiment, we have observed an event in which a trapped particle oscillates between the two fibers (Fig. 4.6). It occur due to a slight misalignment of the two counter-propagating light beams. The particle starts oscillating in a slightly tilted elliptical orbit at a frequency of about 10Hz. It has an amplitude of 3.5 and 0.3 μm in the axial and transverse directions, respectively. The maximum optical force of about 1.9 pN is obtained at the equilibrium position from a distance between two fibers.

Based on these experimental studies, we conclude the particle trapping experiment using Fresnel lens fibers. Their high trapping performance has allowed measuring a trapped particle with high accuracy. The smaller N.A. (0.3 and 0.5) fibers have appeared very effective in far-field optical trapping or manipulation, which can be further used for studying single nanoparticle or biological specimens. Considering our interest in investigating the anisotropic luminescent feature of $NaYF_4$:Eu^{3+} nanorods, the 0.5 N.A. fibers can provide a befitting scenario for measuring their PL emission.

4.1.2 TIR-probe Fibers

We have used TIR-probe fibers for studying the optical trapping in a single fiber geometry by producing an annular beam. For this experiment, we have used two different sizes of polystyrene particles of 0.5 and 1 μm in diameter which have been trapped in two distinct trapping experiments.

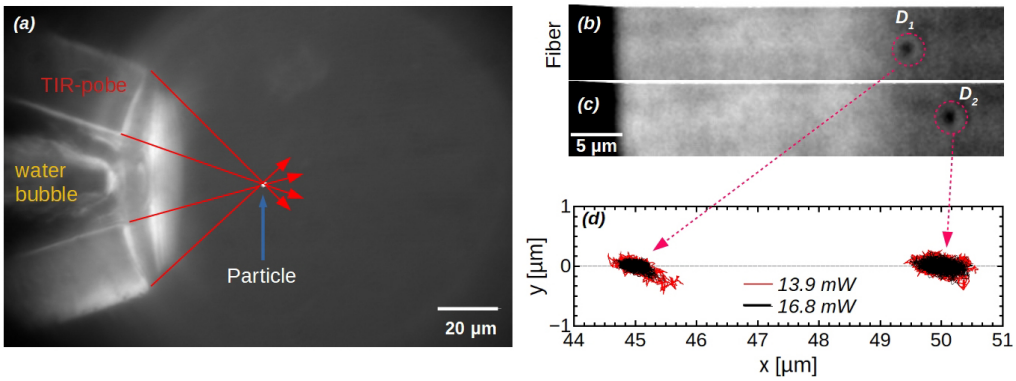

Figure 4.7: (a) A microscopic image is labelled to represents the particle trapping using a single TIR-probe fiber, (b) and (c) present the microscopic images which have been captured at a light power of 16.8 mW of for a trapped particles at two different trapping positions D_1 = ~40 μm and D_2 = ~50 μm, respectively. Scales of these two images are the same. (d) Trajectories of the trapped particle at two different powers.

The particle trapping is observed at five different light powers in the range from 16.8 mW to 5 mW. Figure 4.7 (a) shows the trapping of a particle at the focal point of the fiber. In the video observation, we have found that the particles are trapped at two stable positions, first at ~45 μm (D_1) and second at ~50 μm (D_2) from the end of the fiber (Figure 4.7 (b) & (c)). These two positions occur due to the converging of light beams at two distinct spots. These two events are observed in two distinct trapping sequences. We have seen that the particle jumps from first to second trapping position, however, it is rare to observe two particles trapped at two separate positions simultaneously in a video. For the light power below ~ 14 mW, the particles are stably trapped at the first trapping position. Note that the light power which has been used in this experiment is the total emitted fiber's output power measured in air.

Trajectories of trapped particles at two different light powers are presented in figure 4.7 (d). In measurements at 16.8 and 13.9 mW light power, the trapped particles jump from the first to the second position during the interval of image sequence acquisition (3-5 min). The tracking plots reveal an anisotropic trapping potential and indicates that particles are stably trapped at D_1. The particle is more confined in transverse direction compared to the axial direction. It is observed that the particle trajectories elongate on lowering the light power. Also, a small tilt can be noticed in each trajectory but is more pronounced for the particles trapped at D_1 than in (D_2). This tilt has appeared due to an asymmetry of the converging beams, which caused by a minor misalignment of optical element during probe fabrication.

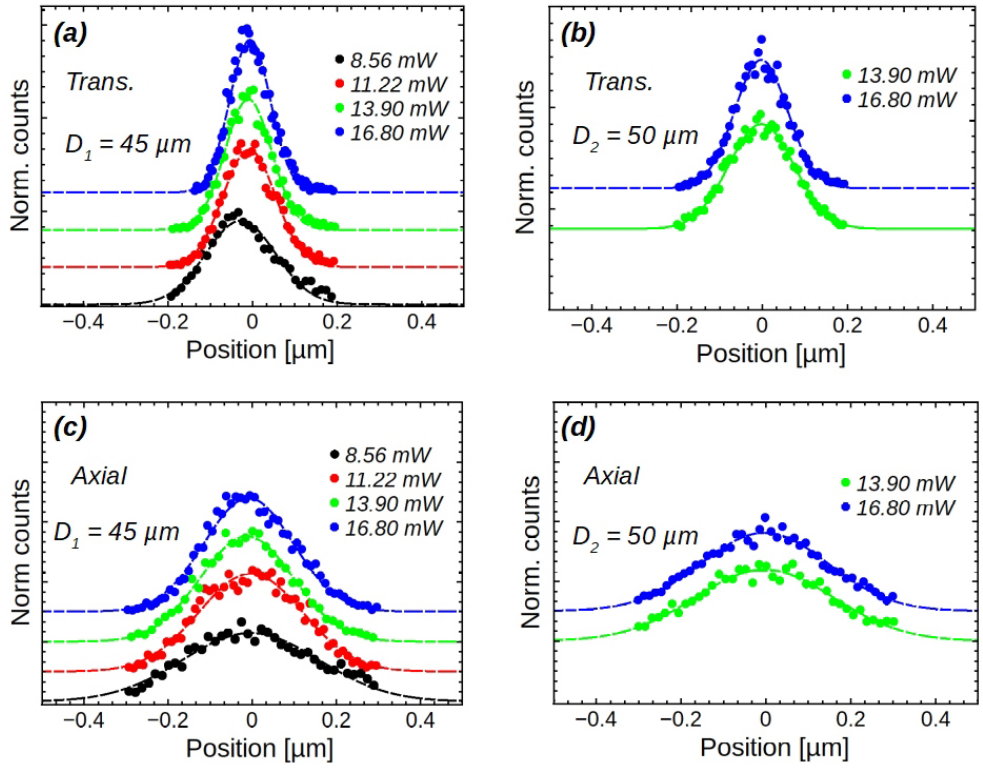

Figure 4.8: Position distribution of trapped particle at different light powers. (a) & (b) corresponds to D_1 (= 45 μm) and D_2 (= 50 μm) in transverse direction, respectively. (c) & (d) corresponds to D_1 and D_2, in axial direction, respectively.

Position distribution of trapped particles is obtained separately in transverse and axial directions using the BS method to determine the κ values. Figure 4.8 represent the position distribution for the two trapping position in both directions. The obtained κ values are linearly dependent on the applied light powers (Figure 4.9). The normalized $\tilde{\kappa}$ values for the two trapping positions are determined in both directions, which are listed in Table 4.2. The $\tilde{\kappa}$ in the transverse has appeared 4.4 times higher than axial direction at the D_1. Also, the particle trapping at D_1 position is two times more stable as compared to trapping at D_2.

In comparison with trapping of 1 μm particles in a similar experiment, which are traped at a position of about to 46.2 μm from the fiber, we have observed that particles are strongly confined near the first trapping positions. Depending on the $\tilde{\kappa}_{trans.}/\tilde{\kappa}_{axial}$ ratio, 0.5 μm particles are 50% less stably trapped at the first trapping position. Compared with the trapping performance of Fresnel lens Fibers with 0.5 N.A. for 0.5 μm, this fiber is about 3 times more efficient. However, it is 5-6 times less stable for 1 μm particles. Furthermore, this fiber supports transporting the optically trapped particles from one position to another in a controlled manner. It has allowed transportation of 1 μm particles in transverse and axial directions with a speed of 15 μm/s.

In general, the TIR-probe fiber has presented an excellent trapping performance by producing at a highly stable optical trap for particles. However, the appearance of more

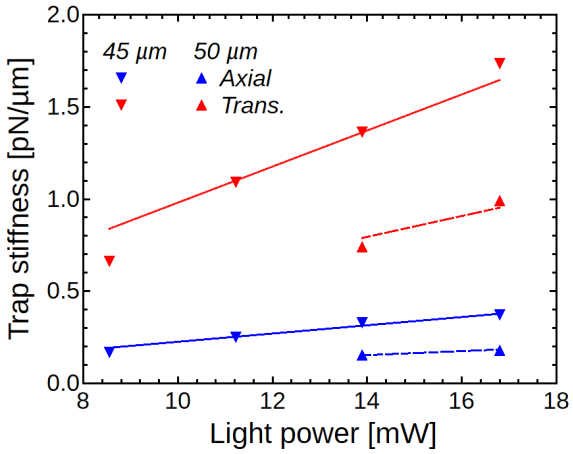

Figure 4.9: A plot of obtained κ against the corresponding light powers for the both trapping positions.

Table 4.2: Normalized trap stiffness $\tilde{\kappa}$ obtained using BS method for the particle trapping using TIR-probe fiber. D_f: distance from fiber

D_f [μm]	$\tilde{\kappa}$ [pN·μm^{-1}·W^{-1}]		
	axial	trans.	$\tilde{\kappa}_{trans.}/\tilde{\kappa}_{axial}$
45	22.4	97.8	4.4
50	10.6	56.6	5.2

than one trapping spots leads to the distribution of optical force, which slightly reduces its efficiency. This undesirable feature can be eradicated by considering the design of its fabrication. This fiber can show great potential for trapping of the biological specimens or even smaller particles than the ones presented here. Considering the design of this probe fiber, it can be highly beneficial for measuring the fluorescence emission through it for spectroscopy or bio-imaging applications.

4.2 Trapping of $NaYF_4$ nanorods

The experimental measurement presented so far are studied with spherical particles. It has observed interesting to study the trapping behaviors of anisotropic luminescent nanoparticles following our previous research activities [3], [4]. The main interest of this experimental study is to characterize the luminescent features of a single nanoparticle in reduced environmental conditions such as a substrate-free environment. For this specific purpose, we have used lanthanide-doped nanoparticles, which are featured with anisotropic luminescent emission. The principle of these nanoparticles is based on the process of photon conversion in which they absorb a light energy during the laser excitation and emit the light in the energy range from UV to infrared region [121]. In general, the nanoparticles show Stokes shift emission when they emit photon having less energy than the absorbed one [122]. In the process, where they emit higher energy than the absorbed energy, it is known as an anti-Stokes emission.

For our spectroscopic characterization, we choose to characterize the PL emission of europium (Eu^{3+}) doped $NaYF_4$ nanorods. These special nanorods have been chosen considering the following reasons:

1. The aspect ratio (length/width) of the rod is well controlled and may be easily modified [4], [123], [124].
2. The fabrication of these nanorods is well controlled and they have good dispersion in water [123].
3. These nanorods show excellent anisotropic luminescent properties due to the distribution of (Eu^{3+}) ions in the anisotropic host matrix [124]–[126].
4. These nanorods allow us to study anisotropic emission of an optically trapped single particle. This measurement is a highly exciting aspect for the study of orientation resolved emission properties [124], [126].
5. We have already used the Er/Yb doped $NaYF_4$ nanorods, with different aspect ratios and successfully studied their emission spectra efficiently [4].
6. These nanoparticles are suitable for the biomedical application [127]

In general, the $NaYF_4$ nanorods are bio-compatible materials used as one of the efficient host materials for rare-earth dopants for emission in visible range [128], [129]. The presence of Yttrium in the host nano-crystal structure allows doping with other lanthanide ions very easily and can activate them very efficiently [130].

4.2.1 Nanorods elaboration

The $NaYF_4$:Eu^{3+} nanorods are developed by Jeongmo Kim as part of his Ph.D. thesis work at PMC, Ecole Polytechnique, Palaiseau [123], [131]. The $NaYF_4$:Eu^{3+} nanorods

are elaborated following the hydrothermal methods and it is described in detail [123], [131]. In a typical chemical experiment, 45 mmol (1.8 g) of NaOH is mixed in 6 mL of water. Later, 15 mL of ethanol (EtOH) and 30 mL of oleic acid (OA) is added to the mixed solution gently while stirring [132], [133]. Thereafter, 0.95 mmol (288 mg) of $Y(Cl)_3{\cdot}6H2O$, 0.05 mmol (18 mg) of $Eu(Cl)_3{\cdot}6H_2O$ and 10.2 mmol(377mg) of NH_4F dissolved in 4 mL of water and added selectively to the obtained chemical solution. Then, the obtained solution is transferred into an autoclave and heated at 200°C while stirring continuously for 24 hrs. Then, this solution is cooled down to ambient temperature to obtain suspended nanoparticles. The resultant nanoparticles are precipitated in 50 mL of ethanol and collected by centrifugation.

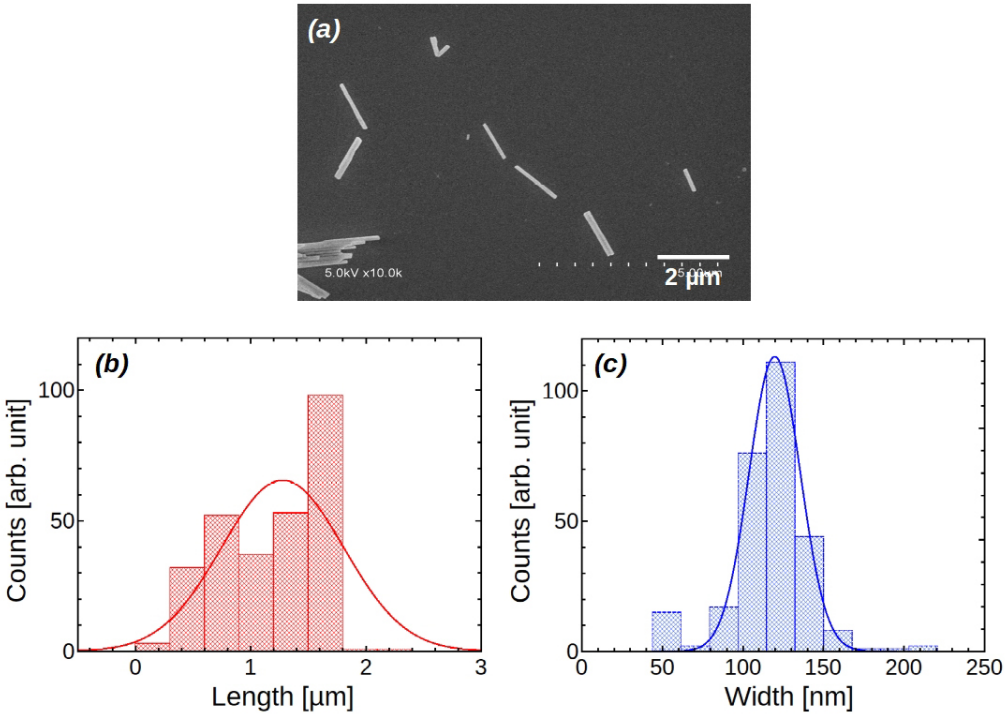

Figure 4.10: (a) SEM image of $NaYF_4$:Eu^{3+} nanorods. The obtained distribution of particle length and size. The fitted curves correspond to a Gaussian fitting.

Afterward, the obtained nanoparticles are washed with water and ethanol several times and dried in a vacuum chamber to obtain the white powder of nanoparticles. Through this process, 60% of the resultant product is obtained from the original amount of yttrium chloride.

The produced nanoparticles are characterized at PMC, Palaiseau using different characterization techniques such as SEM [123], [131]. The morphology of nanoparticles is studied in SEM and their size distribution is measured (Figure 4.10). Their length and width are determined by fitting a Gaussian function to the distribution and observed with a mean length of 1.2 ± 0.4 μm and diameter of 120 ± 20 nm. Using X-ray diffraction technique (XRD), a hexagonal structure is observed for these nanorods [123], [131]

The final step is performed to functionalize these nanoparticles. For this 20 mg of

$NaYF_4$:Eu^{3+} nanoparticles are added in oleic acid and kept for sonication, followed by three times centrifugation with 2 mL aqueous citrate solution (0.2 M). Finally, the resultant solution is washed with EtOH and water to remove the excess oleic acid molecules and ensured that the nanorods are well dispersed in water [123]. To use these nanoparticles for our optical trapping experiments, the nanorods solution is extensively diluted in water and sonicated for 10 - 15 minutes to get a well dispersed trapping sample.

These nanorods are trapped using two different types of optical fibers: a single tapered fiber tip [2], and Fresnel lens fibers. These trapping experiments are exploited to measure the Eu^{3+} emission spectra and PL decay lifetime.

4.2.2 Tapered fiber tips

Nanorod trapping

The $NaYF_4$:Eu^{3+} nanorods are trapped by employing a tapered fiber tip in single fiber geometry. The trapped nanorods are visualized by Eu^{3+} ions PL emission which has been excited using a 394 nm pump laser having a typical pump power of ~25 mW. Their images are characterized by bright elliptical spots with a typical length and width of 1.5 µm and 500 - 600 nm. The characterized particle width corresponds to the microscopic resolution of our visualization system of about 500 nm and thus it is not possible to resolve the actual nanorod width.

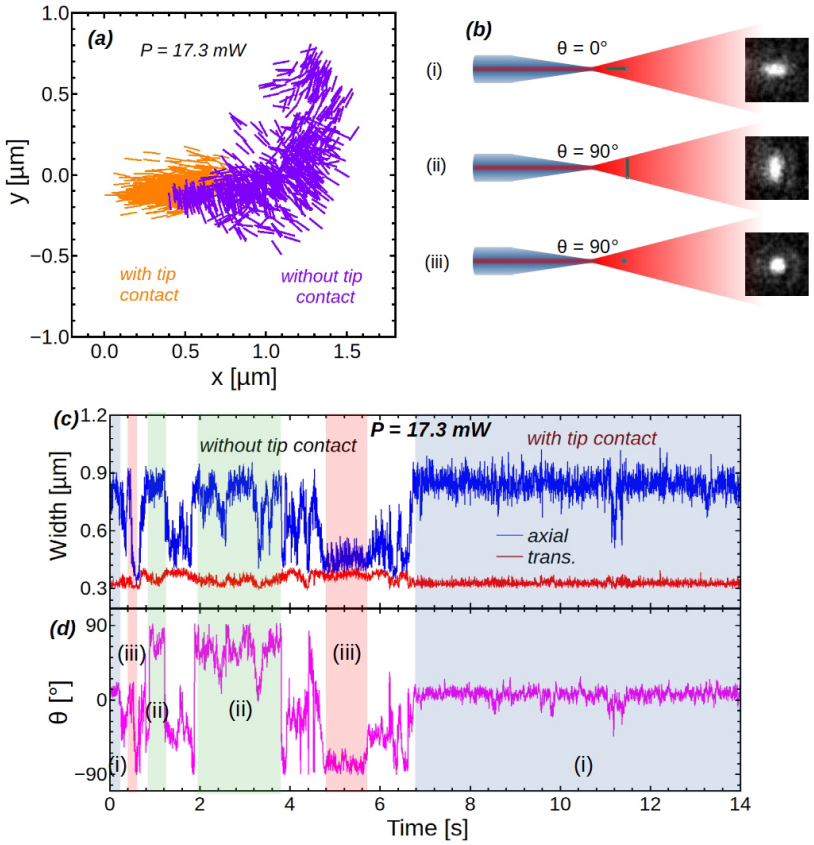

Figure 4.11: Nanorod trapping using the single tapered fiber tip at a light power of 17.3 mW. (a) the x-y trajectory of the nanorod with and without tip contact. (b) Three preferred orthogonal orientations of the trapped nanorods. Time-dependent (c) tracking width and (d) angular orientation tracking of trapped nanorod with and without tip contact.

In the present measurement, the optical trapping of nanorods is studied by varying the applied light power from 11.8 mW to 52.1 mW in several steps. In trapping videos, the nanorods behaviors are distinguishable with two effects; first trapping at tip contact or in the proximity of fiber tip. In case of trapping a nanorod at tip contact, a second

nanorod is trapped at a distance of ∼5 μm from the fiber tip in axial direction, however, it is rare. For a trapping event at 17.8 mW, the nanorod is first trapped near to the fiber tip (at ∼1 - 1.5 μm) about ≈9 sec before going back to at the tip contact (Figure 4.11). Further increasing the power, nanorod's dynamic movement is reduced and shifted towards tip contact and slowly becomes stable. The observation times for a trapped nanorod with or without tip contact are listed in Table 4.3. For the powers above 34 mW, the nanorods are efficiently trapped at the fiber tip contact and remain in the same condition during the entire recording interval up to 15 sec. The nanorods are leaving their trapping position immediately after switching off the trapping laser. Thus it confirms that the observed results are due to optical forces only.

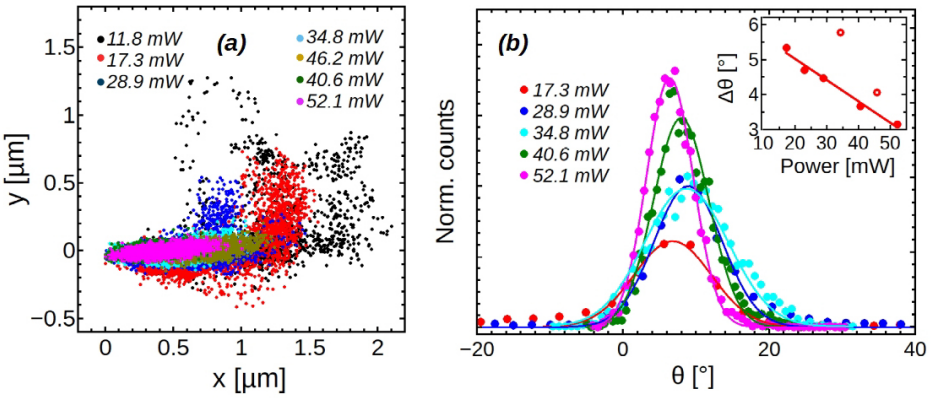

Figure 4.12: Nanorod trapping is studied as a function of light power. (a) the x-y trajectory of trapped nanorods. (b) Nanorod angular orientation distribution and best fitted Gaussian curves allow us to deduce distribution width ($\triangle\theta$). Inset: A plot of $\triangle\theta$ vs. the used light powers.

Table 4.3: The observation time to find a trapped nanorod with or without the fiber tip contact. $\triangle\theta[°]$: nanorods angular distribution width in tip contact.

Power [mW]	Time [s]		$\triangle\theta[°]$
	with contact	without contact	
52.1	15.0	-	3.1
46.2	15.0	-	4.0
40.6	15.0	-	3.6
34.8	15.0	-	5.7
28.9	12.5	2.5	4.5
23.0	12.0	3.0	4.7
17.3	8.9	6.1	5.3
11.8∗	3.8	3.7	-

∗ nanorod left the trap after 7.5 s.

The x-y trajectory of trapped nanorods at 17.3 mW is present in Figure 4.11 (a). It reveals an anisotropic trapping volume, which is highly elongated in the axial direction. The range of nanorod's residual motion is small compared to its length. The nanorods are mainly oriented parallel to the fiber axis while in the tip contact. However, in the case of without tip contact, the nanorods are rotating with two meta-stable orientation

either parallel (i) or perpendicular ((ii) & (iii)) to fiber axis (Figure 4.11(b) & (c)). The first two orientations (i) and (ii) are corresponding to two distinct tracking widths, whereas the last orientation (iii) can be dedicated to a case when the two widths are the same. In this case, we have measured the angle (θ) of nanorod orientation based on the nanorod tracking, which allows us to distinguish the two orientations.

In general, x-y tracking curves as a function of light power are obtained. These curves have revealed that nanorods are trapped in an anisotropy trapping volume (Figure 4.12 (a)). It shows that nanorods trapping at high power have one stable trapping position whereas at low powers it has more than one stable trapping positions. The Nanorods Brownian movement is increasing when power is reduced. The nanorod Brownian motion is completely dominating in the case of lowest power, therefore nanorod left the trap after 7.5 sec.

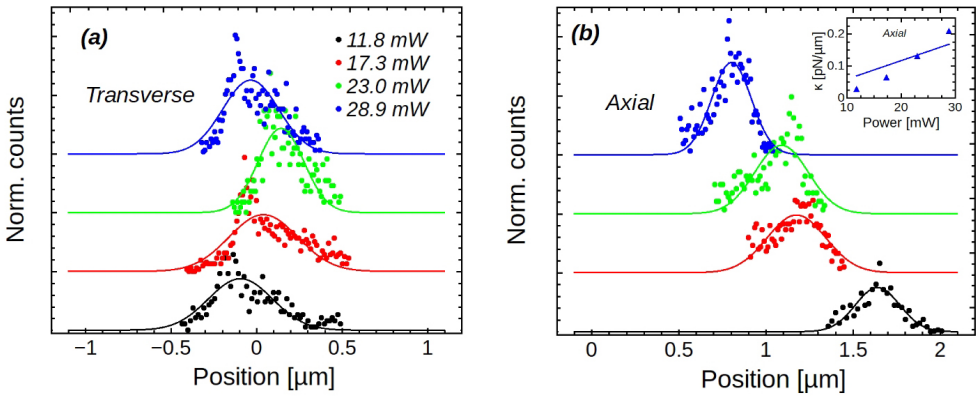

Figure 4.13: Position distribution of trapped nanorods when they stay away from the tip contact are given in (a) transverse and (b) axial direction. Inset: A plot which is showing κ as a function of powers for without tip contact in axial direction.

Nanorod trapping with tip contact excludes the application of the harmonic potential approximation and the related trap stiffness κ. However, in this case, we use residual angular nanorod motion to evaluate the light power-dependent trapping efficiency. Figure 4.12 (b) represents the probability distribution of the angular orientation of the nanorod at contact and fitted with a Gaussian function. Their mean angular orientation (refer to Gaussian peak) is measured about 8° to 10° tilted with respect to the fiber axis. This small tilt is considered as due to geometric imperfections at the fiber tip contact point. The angular orientation width ($\triangle\theta$) is deduced using the Gaussian fits. A plot of $\triangle\theta$ vs. light power is obtained, which shows that the orientation width decreases linearly on increasing the trapping power (inset, Figure 4.12 (b)).

For accounting trapping efficiency, we choose the trapping events when the particle is not in tip contact. Figure 4.13 (a) and (b) shows the position distributions of without tip-contact trapped nanorods in transverse and axial directions, respectively. It can be observed that distributions are not well symmetric in transverse direction. For tip contact trapping, the validity of the harmonic oscillator model can be questionable, and thus, a valid κ value can not be deduced. For the position distribution in the axial direction, the distance between trapped particles mean position and fiber tip contact decreases

when light power is increased. Also, it remains symmetric, and the distribution width is decreasing while power increases. In this case, we measured the κ values using the BS method, which shows a linear dependency on light power (Inset: Figure 4.13 (b)). The normalized $\tilde{\kappa}$ values is estimated about 6 $pN \cdot \mu m^{-1} \cdot W^{-1}$.

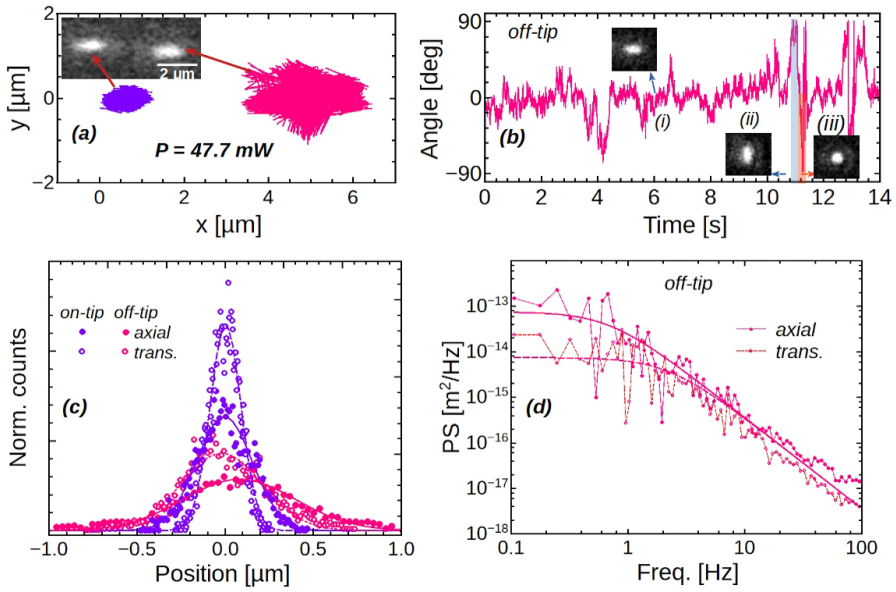

Figure 4.14: (a) Position tracking curve for two distinguished trapped nanorods: in-tip contact (0 μm) and off-tip at (5 μm). (b) Angle tracking curve of the off-tip nanorod. (c) BS of trapped nanorods on-tip contact and off-tip (d) PSA fitting for the off-tip trapped nanorod.

During a trapping event at high light power, we observe a second nanorod is trapped at a secondary stable trapping position at a distance of about 4-6 μm from the fiber tip, whereas the first nanorod is at the tip contact, simultaneously (inset: Figure 4.14 (a)). Through this observation, it is noticed that off-tip nanorod is less stably trapped compare to trapping in fiber tip contact. The x-y tracking of off-tip nanorod trapping shows an anisotropic trapping volume which is larger compared to trapping of in-tip contact. Nanorod orientation tracking reveals the preferential orientation of off-tip nanorod, which is mostly oriented parallel to the fiber axis (Figure 4.14(b)). Also, we find that this nanorod has a wider angular orientation distribution width compare to the last case. The position distribution widths for off-tip nanorod are observed about 0.8 and 1.2 μm in transverse and axial directions, respectively (Figure 4.14(c)). In this case, the application of BS and PSA methods are very straightforward to apply in the framework of harmonic oscillator approximation (Figure 4.14(c) and (d)). Considering the anisotropy of nanorod, we use a corrected expression for the Stokes' friction coefficient in the PSA [134]–[136],

$$\gamma_0 = \frac{4\pi l \eta}{\ln(l/d) + 0.84} \tag{4.1}$$

where η is the dynamic viscosity of the surrounding medium (in the case of water η = 8.65×10^{-4} N·s·m^{-1} at 300 K), l and d are the nanorod length and diameter, respectively.

The resultant friction coefficient is calculated as 5.32 $\times 10^{-9}$ N·s·m^{-1}. The normalized $\tilde{\kappa}$ value is deduced as 1.7 and 1.9 pN·μm^{-1}·W^{-1} using the BS and PSA methods, respectively, in transverse direction. The resultant κ values, which are deduced using these methods are found to be in the good agreement.

The presented nanorods trapping results have been observed in good agreement with previous works based on trapping of $NaYF_4$:Er/Yb nanorods with different aspect ratios [4], [98]. In the previous work, it has been observed that nanorods trapping behavior depends fundamentally on their length. The nanorods having a length shorter than 1 μm are pushed by light beam away from the used optical fiber tips and, therefore, stably trapped using dual fibers approach. However, the nanorods longer than 1 μm are pulled by the beam towards the tips and thus are not stable in the dual fibers approach. In the present work, we have also observed the similar effect for nanorods around 1.9 μm long. Compared to the trapping efficiency of 1.9 μm long nanorods, the normalized trap stiffness is observed similar in axial direction, but about 4 times higher in transverse one [98]. Moreover, the mean distance from the fiber tip is the same.

Spectroscopy

In chapter 2, we have presented the scheme of our experiment, which allows us to measure emission spectroscopy of the trapped nanoparticles. Using this setup, it is possible to record the spectroscopy with two accessible configurations; firstly, through the microscope objective and secondly, through the trapping optical fiber with respect to the nanorod axis and other configuration is in parallel direction. In the present experiment, we have measured anisotropic PL emission of a trapped $NaYF_4$:Eu^{3+} nanorods in contact of a tapered fiber tip.

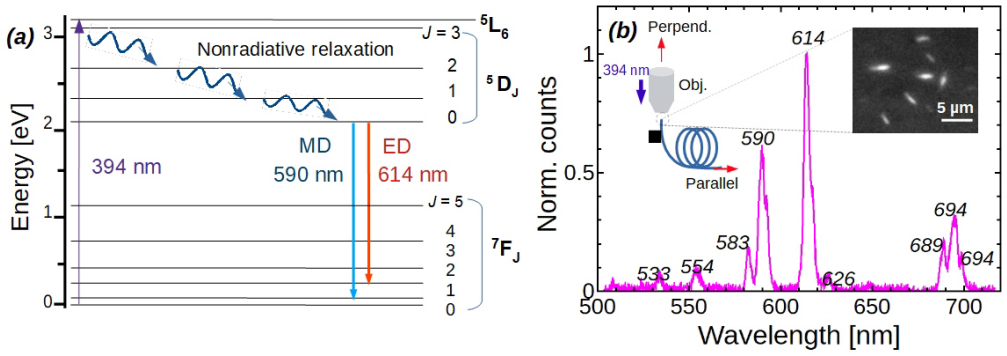

Figure 4.15: (a) Energy diagram of Eu^{3+} ions emission from $^5D_0$ to ^7D_J transition via radiative transition. (b) The spectrum of Eu^{3+} ions PL emission in perpendicular direction which observed on facet of a cleaved fiber. (Inset) Microscopic image of the nanorods on the facet.

Figure 4.15 (a) shows the energy level diagram of Eu^{3+} ions emission under the PL excitation of 394 nm light. This excitation line correspond to energy transition from ground state ($^7F_0$) to excited state ($^5D_6$) [137]. After excitation, the Eu^{3+} ions relaxes to

the lower state by releasing their energy via nonradiative multiphonon relaxation pathways. The rate of this relaxation depends exponentially on the phonon energy of $NaYF_4$ matrix (has a relatively low phonon energy about 300–400 cm^{-1}) [137]. As a result of multiphonon relaxation, it emits PL via a radiative transition of $^5D_0 \rightarrow ^7F_J$ [124].

In the very first measurement, we have observed emission spectra through the perpendicular directions using a few $NaYF_4$:Eu^{3+} nanorod clusters on facet of a cleaved fiber. The fiber is placed vertically to the microscope objective which is used to align the two directions for recording the emission (inset, Figure 4.16 (b)). The recorded spectrum in perpendicular direction has appeared with several peaks, which correspond to Eu^{3+} ions PL emission (Figure 4.16 (b)). The strongest emission is measured for a transition at 614 nm and then at 590 nm. These two peaks are originated from the radiative transitions of $^5D_0 \rightarrow ^7F_2$ and $^5D_0 \rightarrow ^7F_1$, which are corresponding to electric dipole (ED) and magnetic dipole (MD) transitions, respectively [137].

However, the used method of alignment has not provided the benefit for observing the emission through fiber (parallel direction) since it is difficult to align the nanorod at the fiber's core. To make it easier, we have used a tapered fiber tip, which has the advantage of its tip geometry, which allows us easy picking of nanorods from the suspension sample. Thus using a few nanorods, which are adhered to the fiber tip apex with an orientation parallel to the fiber axis, we have aligned the parallel direction to record nanorod's PL is observed through the fiber. Afterward, in successive experiments, we measure the Eu^{3+} ions PL emission using an optically trapped nanorod in tip-contact of the fiber, in the given two directions and later on the nanorods stuck to the tip.

For spectroscopy, we have chosen to trap the nanorods at 34.8 mW. For this power, a nanorod can be strongly trapped in fiber tip contact with a nanorod orientation distribution of about 4°. The emission spectra are recorded with a slit width of 0.88 mm and an integration time of 10 seconds. During the spectroscopic measurements, we have focused our observation on the two strongest transitions. Figure 4.16 (a) presents the spectra recorded separately in perpendicular and parallel directions for the trapped nanorod and the nanorods adhered to fiber tip, respectively. These spectra show that the peak regions are 608 - 620 nm and 586 - 595 nm for ED and MD transitions. PL emission appears relatively stronger for the trapped nanorod, especially in the parallel direction, which may be featured due to the auto-alignment of nanorod with fiber tip (inset Figure 4.16 (a)). The small peak at around 583 nm corresponds to energy transition $^5D_1 \rightarrow ^7F_3$, and is well-pronounced for the perpendicular spectra and detected mainly for the adherent nanorod. The ED peak shape is observed slightly broader in the perpendicular direction. The spectra in parallel direction suggest that observed PL emission is mostly due to the trapped nanorod's long axis.

Polarization resolved emission spectroscopy

Afterward, we have studied a polarization-dependent PL emission spectra for ED and MD transitions (Figure 4.16(b)). These measurements are recorded with a slit width of about 0.88 mm and an integration time of 10 sec in the perpendicular direction with respect to the nanorod axis. In parallel direction, no polarisation-dependency of Eu^{3+}

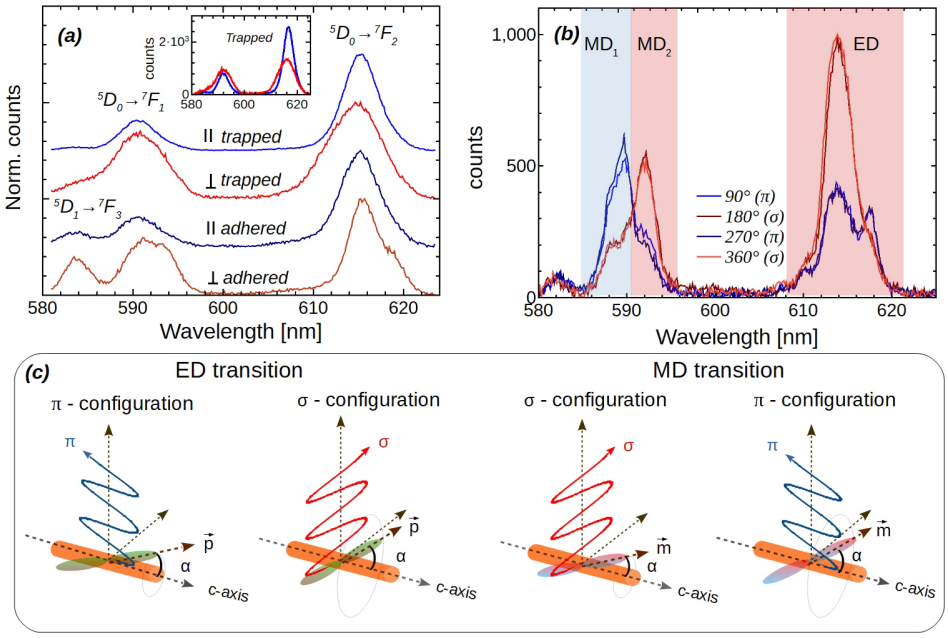

Figure 4.16: (a) Eu^{3+} PL emission spectra obtained in two orthogonal directions: perpendicular and parallel directions with respect to the nanorod axis for trapped and stuck nanorods, respectively. Inset: comparison of two spectra measured on the trapped nanorod in perpendicular direction without normalization. (b) Polarization-dependent Eu^{3+} PL emission spectra are presented for a wavelength range of 580-625 nm in the perpendicular direction with a polarizer angle from 90° to 360°. (c) Schematics of σ and π configuration for Eu^{3+} emission, where $\vec{p}$ and $\vec{m}$ represent the electric and magnetic dipole moments.

emission is observed which reflects the hexagonal symmetry of the crystalline nanorod with the c-axis parallel to the rod axis.

We measure the polarization-resolved spectra separately for ED (608 to 620 nm) and MD transitions (586 to 595 nm). The spectra are measured for a full cycle of 360° with a step of 15°. For this measurement, we choose to begin spectral recording for a polarization angle (refer to 0°) where the ED peak has a maximum intensity which appears perpendicular to the nanorod axis. This spectrum at 0° polarizer angle actually corresponds to σ-configuration of polarization with respect to the nanorod axis. Similarly, 180°, and 360°, which are appeared with maximum peak intensity have been denoted by σ and those at 90° and 270° with minimum intensity by π. (Figure 4.16 (b)).

Firstly, the observed spectra of ED transition are analyzed by measuring the peak intensity. The experimentally measured spectra are fitted with four Gaussian peaks 610.2 nm, 613.2 nm, 614.9 nm, and 617.5 nm.A polar diagram is obtained using the measured peak intensities (Figure 4.17 (a)). The obtained values are fitted with an orthogonal polar function,

$$I = A \cdot \cos^2(\theta_P - \varphi) + B \cdot \sin^2(\theta_P - \varphi), \tag{4.2}$$

with I is the intensity, θ_P the polarization angle, and φ a phase shift, which shows the

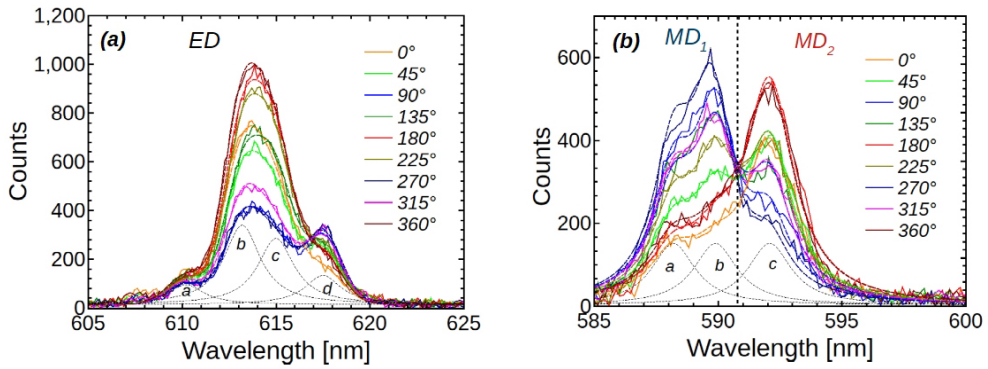

Figure 4.17: Polarisation-dependent Eu^{3+} emission spectra with raw and peak fitted curves for (a) ED and (b) MD. For ED, four Gaussian peaks are fitted at a = 610.2 nm, b = 613.2 nm, c = 614.9 nm, and d = 617.5 nm. For MD there are three Lorentzian peaks at a = 588.2 nm, b = 589.9 nm, c = 592.4 nm.

actual orientation of nanorod. A and B are two free parameters used in fitting, representing the contribution of two orthogonal directions to the experimental reference system. The fitted parameters are listed in Table 4.4. The emission is clearly of σ configuration with the highest intensity ratio (A/B) of 2.8 for the 614.9 nm peak. Considering only the two strongest peaks (613.2 nm and 614.9 nm), a nanorod orientation is measured to be 8°.

Table 4.4: List of fitting parameters for the ED and MD transitions (pf: peak fitting, int.: integration over wavelength range).

Peak	λ [nm]	orient.	A	B	φ	A,B ratio
ED (pf)	610.2	σ	133	86	-6.1° ± 4.3°	1.3
ED (pf)	613.2	σ	760	316	7.9° ± 2.0°	2.4
ED (pf)	614.9	σ	647	232	8.2° ± 2.3°	2.8
ED (pf)	617.5	π	199	281	13.3° ± 4.1°	1.4
MD_1 (pf)	588.2	π	600	1200	10.1° ± 2.7°	2.0
MD_1(pf)	589.9	π	486	897	10.6° ± 2.8°	1.8
MD_2 (pf)	592.4	σ	2466	358	7.5° ± 2.1°	6.9
MD_1 (int.)	586.0 - 590.8	π	876	1752	9.0° ± 1.8°	1.9
MD_2 (int.)	590.8 - 595.0	σ	1275	586	4.9° ± 2.2°	2.3

The MD spectra are fitted with three Lorentzian peaks of equal width at 588.2 nm, 589.9 nm, and 592.4 nm (Figure 4.17 (b)). The polar intensity plots clearly show that the first two peaks (588.2 nm and 589.9 nm) correspond to MD_1 and the third one to MD_2 transition emissions with the σ and π-configuration, respectively (Figure 4.18 (b)).. Peak fitting approach shows higher visibility, especially for 592.4 nm peak, which is appeared with an A, B ratio of 6.9.

Figure4.17 (b) presents the polarization-dependent MD transition (586 - 595 nm) with two subregions, MD_1 and MD_2. A line at 590.8 nm separates these two subregions, which represents the intersection point of all spectra. The polar plots are obtained

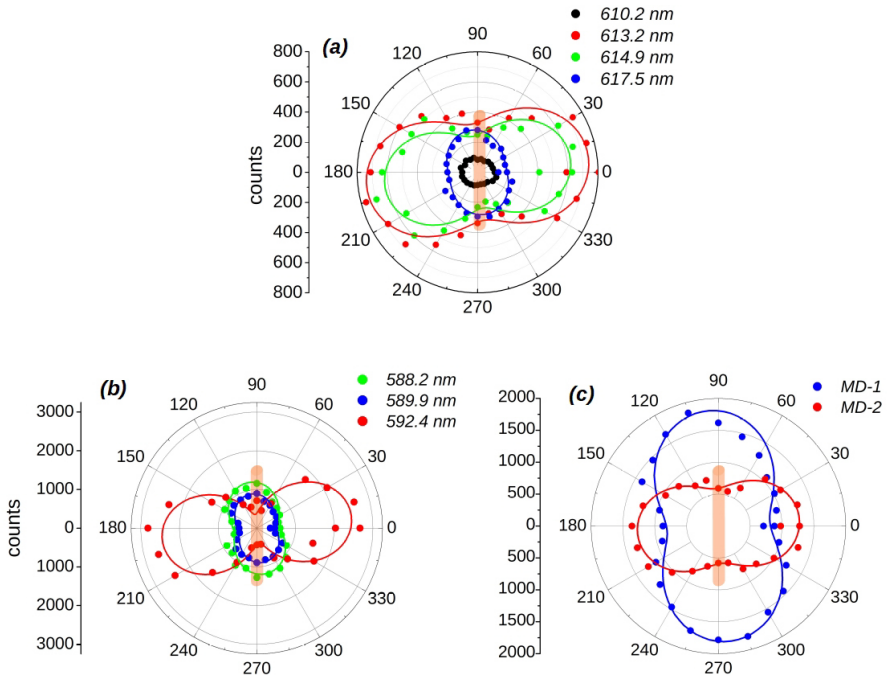

Figure 4.18: The measure intensity polar plot for (a) ED, and (b) MD by peak fitting, and (c) MD by the integrated intensity approach.

using the integrated intensities of MD_1 and MD_2, which indicate their polarisation dependency, and it allows us to identify their configurations. The subregions MD_1 and MD_2 corresponds to the emissions with π and σ-configurations of nanorod, respectively (Figure 4.18 (c)). Moreover, fitting the polar function (Eq. 4.2) measured integrated intensities, the actual nanorod orientation angles are deduced about 9° and 4.9° for MD_1 and MD_2, respectively. The obtained angles are observed in good agreement with the values (~4°) obtained from particle tracking based on trapping video analysis (Figure 4.12 (b)).

To conclude this measurement, we have studied the polarization dependency of two peaks, ED and MD transitions of Eu^{3+} emission. In a comparison to the ED emission, the MD emission is observed with two subregions (MD_1 and MD_2) having the opposite polarization dependency. Their emission configurations are determined using the orthogonal polar fitting that allows measuring the nanorod orientation 7.5° to 10.6° using a peak fitting approach. This result appear to be coherent with nanorod measured by means of trapping video observation. This experimental characterization shows that we can use the spectroscopic approach to measure the nanorod orientation.

Our measurements appear in good agreement with the similar works which are performed to measure the Eu^{3+} emission on quartz substrate [123] and in confocal microscopy on a single nanorod [138]. Previously, Kim et al. have shown a strong influence of host nanocrystals on Eu^3 by measuring a polarization-dependency in $LaPO_4$ host matrix [124]. They have also observed the σ and π configurations for MD_1 and MD_2, respectively.

4.2.3 Fresnel lens fibers

Nanorod trapping

Here, we present a pure, contact-free optical trapping of $NaYF_4$:Eu^{3+} nanorods using the counter-propagating light beams of Fresnel lens fibers of 0.5 N.A. As in the last section, a tip contact-based trapping environment has limited the studying the behaviour of a purely trapped nanorod also it can have influenced the luminescent features of Eu^{3+}. Therefore, we trap these nanorods far from the fiber using Fresnel lens fibers.

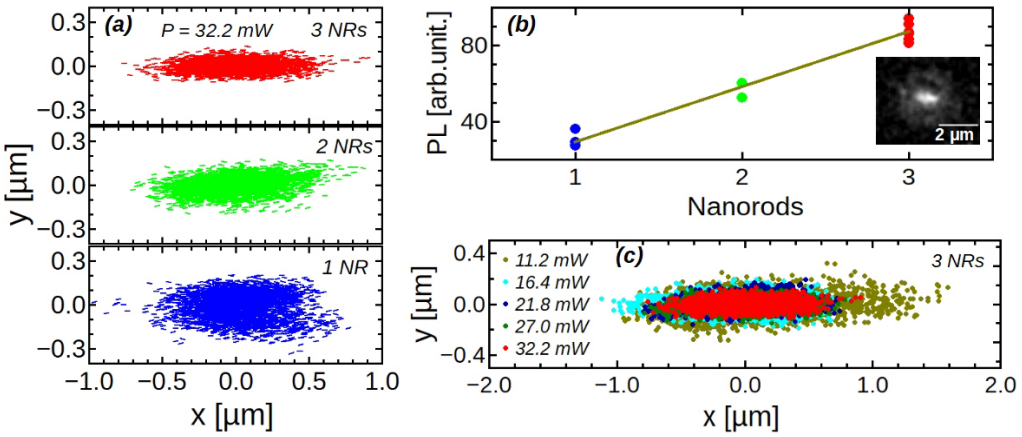

Figure 4.19: (a) The time-dependent angle tracking curves of trapped nanorods at a light power of 32.2 mW. (b) observed PL intensity as a function of number of nanorods in a cluster. (c) The x-y trajectory of a three nanorods cluster (3NRs) as a function of light power.

We have observed a stable and reproducible nanorods trapping at a D_{f-f} about 200 μm. These trapping events are studied at five different light powers (from 11 mW - 32.2 mW). In the experimental measurement, we often observe that the untrapped nanorods are easily attracted to the optical trap. When they enter the trap, they become indistinguishable along with the trapped nanorod, and usually, their long axis aligned parallel to the fibers. Once they assemble within the trap, their separation is not possible but there PL intensity is observed to be increasing. Therefore, we measure the emitted PL intensity of trapped nanorods to estimate the number of nanorods inside the optical trap (or calls it nanorod cluster). It has been observed that the PL intensity is increasing in steps when a nanorod assembles to the trapped nanorods. Figure 4.19 (b) shows a plot of PL intensity which increases when the number of trapped nanorods is increasing in the trap. The obtained lowest PL intensity is estimated for a single nanorod (1 NR) and highest for three nanorods (3 NRs). Therefore, it is possible to observe their trapping behavior as a function of the trapped number of nanorods present in the optical trap or nanorod cluster's size.

Three distinct nanorods or clusters are trapped at a particular light power of 32.2 mW in three separate trapping observations. The x-y tracking curves of trapped nanorod clusters are displayed in (Figure 4.19 (a)), which reveals an anisotropic trapping volume. All

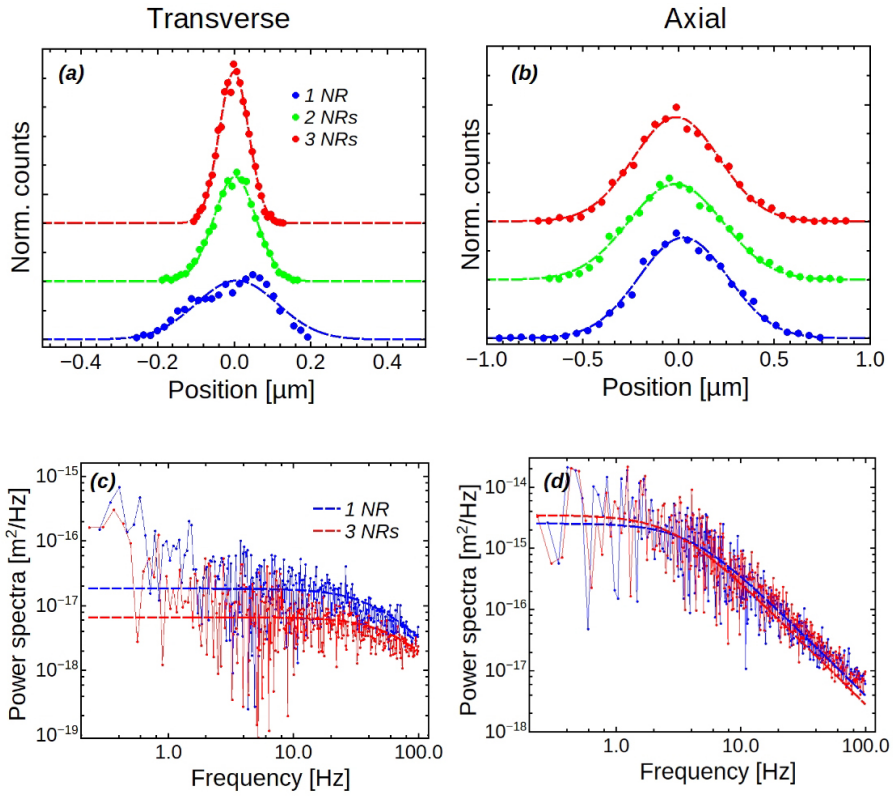

Figure 4.20: Position distribution of trapped nanorods cluster of three different size at 32.2 mW in (a) transverse and (b) axial direction. The dashed line are the best Gaussian fitting. PSA fitting curves in (c) transverse and (d) Axial direction. The dashed lines represents the best Lorentzian fitting curve.

nanorods have a similar movement in the axial direction but are getting strongly confined in transverse direction when the number of nanorods increases. They move about 0.5 to 1.0 μm about their mean position in axial directions with a preferred nanorod orientation and mostly aligned parallel to the fiber axis. Based on the function of light power, the 3 NRs cluster's trapping volumes are getting smaller with increasing the light power and thus, their trapping stability is increasing (Figure 4.19 (c)). Similarly, the trapping of 1 NR is also studied at different light power in range from 32.2 mW to 21.8 mW.

The position distribution of trapped nanorod clusters is measured separately in transverse and axial directions, which are displayed in Figure 4.20 (a) and (b), respectively. The distribution width obtained is smaller for a 3 NRs cluster in the transverse direction as compared to that in axial direction. The κ values are deduced using the BS and PSA methods. Two metastable positions can be observed in the case of 1 NR that excludes determining the related κ. The PSA method allows us to deduce the κ value by fitting a Lorentzian to experimental data (Figure 4.20 (c) and (d)). For this fitting, we have used three different nanorod sizes of 120, 180, and 240 nm with a friction coefficient (given in eq. 4.1) and limited to the frequency range of 0.3 Hz to 100 Hz. It can be noticed from Figure, the power spectra are increasing below 3 Hz in the transverse direction. While it fits very well to the experiment data in the axial direction.

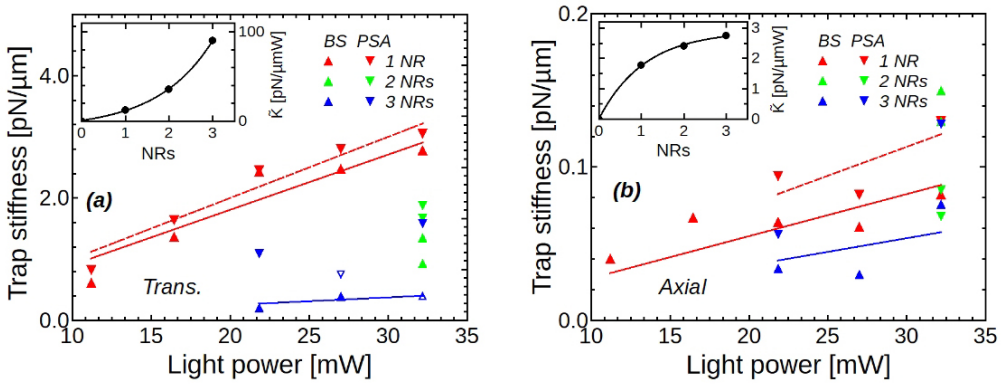

Figure 4.21: Plot of κ values obtained as a function of light power for the three different size nanorod clusters in (a) transverse and (b) axial direction. (Insets) a plot of normalized κ value for all three nanorod clusters at 32.2 mW (a) transverse and axial direction.

In general, the obtained κ values using PSA are a bit higher than BS. The 3 NRs are almost 2.5 and 7 times efficiently trapped than 2 NRs and 1 NR, respectively in the transverse direction. Their $\tilde{\kappa}_{trans.}$ / $\tilde{\kappa}_{axial}$ ratio shows that they are 7 to 33 times stable in the transverse direction than the axial direction. In addition, we have observed that they reveal very different trapping stability for these two directions. The $\tilde{\kappa}$ for nanorods are exponentially increasing in the transverse direction, while converging to a threshold in the axial direction.

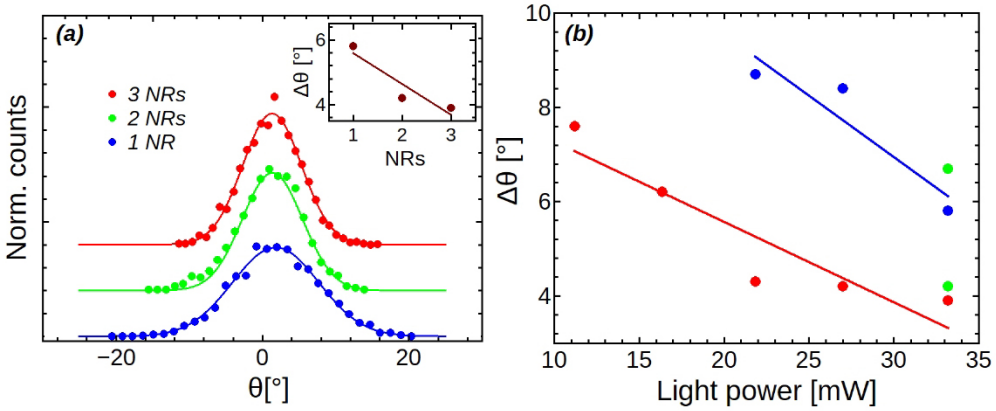

Figure 4.22: (a) Angular orientation distribution for the nanorod clusters trapped at 33.2 mW light power. (Inset) The nanorod angular distribution width obtained as a function of the number of nanorods in a cluster. (b) Plot $\triangle\theta$ as a function of light power for 1 NR and 3 NRs cluster.

Depending on the number of nanorods, their angular orientation distribution is measured and allows determining the angular width ($\triangle\theta$) (Figure 4.22 (a)). This width is decreases as the number of nanorods increases in a cluster (inset, Figure 4.22 (a)). Moreover, the power-dependent measurements reveals that distribution width is decreasing linearly as light power increases (Figure 4.22 (b)). Based on the nanorod orientation, it

can be observed a nanorod cluster of 3 NRs is 0.7 times efficiently confined than the 1 NR.

Table 4.5: Normalized trap stiffness ($\tilde{\kappa}$) obtained by BS and PSA in transverse and axial direction, respectively, along with nanorod angular orientation width ($\triangle\theta$) for one, two and three rods trapped at P = 32.2 mW.

	$\tilde{\kappa}$ [pN·μm^{-1}·W^{-1}]					$\triangle\theta$[°]
	Trans.		**Axial**		$\tilde{\kappa}_{Trans}/\tilde{\kappa}_{axial}$	
	BS	PSA	BS	PSA	BS	
1 rod	12.4	49.3	1.78	-	7.2	5.8°
2 rods	35.0	-	2.4	-	14.5	4.2°
3 rods	90.1	99.8	2.74	3.76	32.8	3.9°

Comparing these results to trapping of spherical polystyrene particles of 0.5 and 1 μm using the same fibers, we observed that nanorods trapping efficiency are 20-100 times (depending on the number of nanorods) lesser than 1 μm particles but in comparison to 0.5 μm particles they are efficient. In the case of nanorods trapping using the tapered fiber tips, the Fresnel lens fibers have provided a very efficient trap, however, the mean nanorod orientation distribution widths remain coherent.

Spectroscopy

Afterward, the stable trapping of $NaYF_4$:Eu^{3+} nanorods is exploited to study the polarization–dependent Eu^{3+} ions PL emission feature. The spectroscopic recording is performed on a trapped single nanorods, which is at 32.2 mW. This light power has been chosen to ensure maximum trapping stability. The emission spectra are recorded only through the microscope objective, which is in a perpendicular direction with respect to fiber and nanorod axis, respectively. These measurements have been recorded with a slit width of 0.88 mm and an integration time of 10 sec.

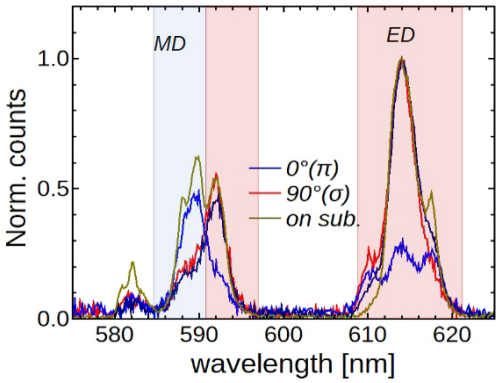

Figure 4.23: Polarization-dependent spectra observed for Eu^{3+} PL emission in perpendicular direction (through the microscope objective) to the nanorod axis. The spectrum with a dark yellow line recorded on the glass substrate.

The polarization-resolved spectroscopy of two main transitions $^5D_0 \rightarrow {}^7F_2$ (ED) and $^5D_0 \rightarrow {}^7F_1$ (MD) is measured with a polarization angle from 0° to 180°. Here, we would like to mention that the measured 0° spectrum is now corresponds to the polarization angle parallel to the nanorod axis. In this measurements, we have corrected the error of referring the spectra corresponding to the polarization angle, e.g., 90° is referred to σ-polarization and 180° with π-polarization. Several attempts have been made to record a full 360° polarization angle measurements but could not be done due to intrusion of multiple upcoming nanorods in the optical trap. There is no option to control these unwanted guest nanorods.

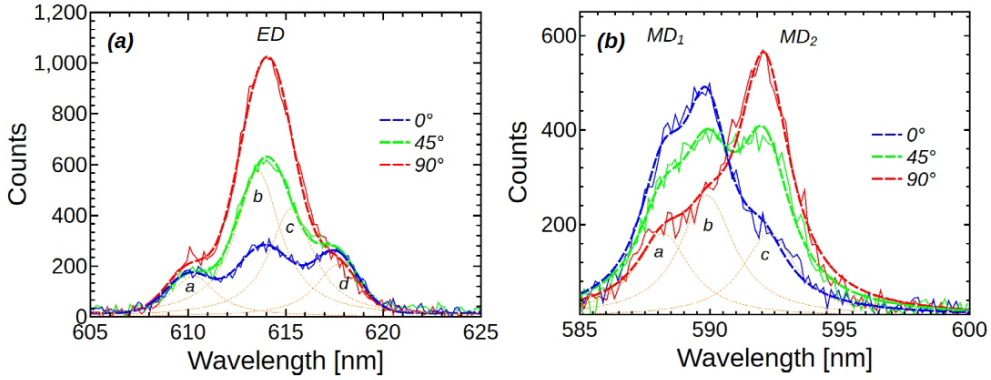

Figure 4.24: Polarisation-dependent Eu^{3+} emission spectra with raw and peak fitted curves for (a) ED and (b) MD. For ED, four Gaussian peaks are fitted at a = 610.3 nm, b = 613.6 nm, c = 615.3 nm, and d = 617.7 nm. For MD, there are three Lorentzian peaks at a = 588.0 nm, b = 589.9 nm, c = 592.3 nm.

The observed spectra of Eu^{3+} PL emission shows the two strong peaks at 608 - 620 nm and 586 - 595 nm similar to our previous measurement with tapered fiber tip (Figure 4.23 (a)). The strongest peak is observed at 608 - 620 nm, which corresponds to ED transition. A σ orientation can be clearly noticed for ED peak with a measurement of 90° polarization in the given figure. Whereas two separate subregions can be found in case MD transitions for a peak region of 586 to 595 nm. Moreover, a third spectrum is shown in Figure (4.23 (a)) is measured on nanorod cluster (of 10 - 15 nanorods) over a glass substrate at the end of the experiments but not used for measuring the polarization dependency. This spectra clearly shows all three observable peaks of MD (about 588, 590, and 592 nm) and two peaks for ED (about 614 and 617 nm). Also, an observable peak of about 583 nm, which corresponds to $^5D_1 \rightarrow {}^7F_3$ transition, is more pronounced for nanorods on the substrate.

The influence of polarization is separately studied for ED and MD transitions in this experiment. Firstly, we have measured ED transition spectra and observed that peaks are still not visible to identify. For this reason, we use a peak fitting approach using four Gaussian peaks at 610.3, 613.6, 615.3, and 617.7 nm. The peak intensities correspond to these peaks are used for determining a normalized emission diagram in polar form. These intensities are normalized by the maximum peak intensity corresponding to the given peak's spectra. This normalization is used to measure α-angle between the respective dipole moments and the nanorod c-axis, which we will explain further in this

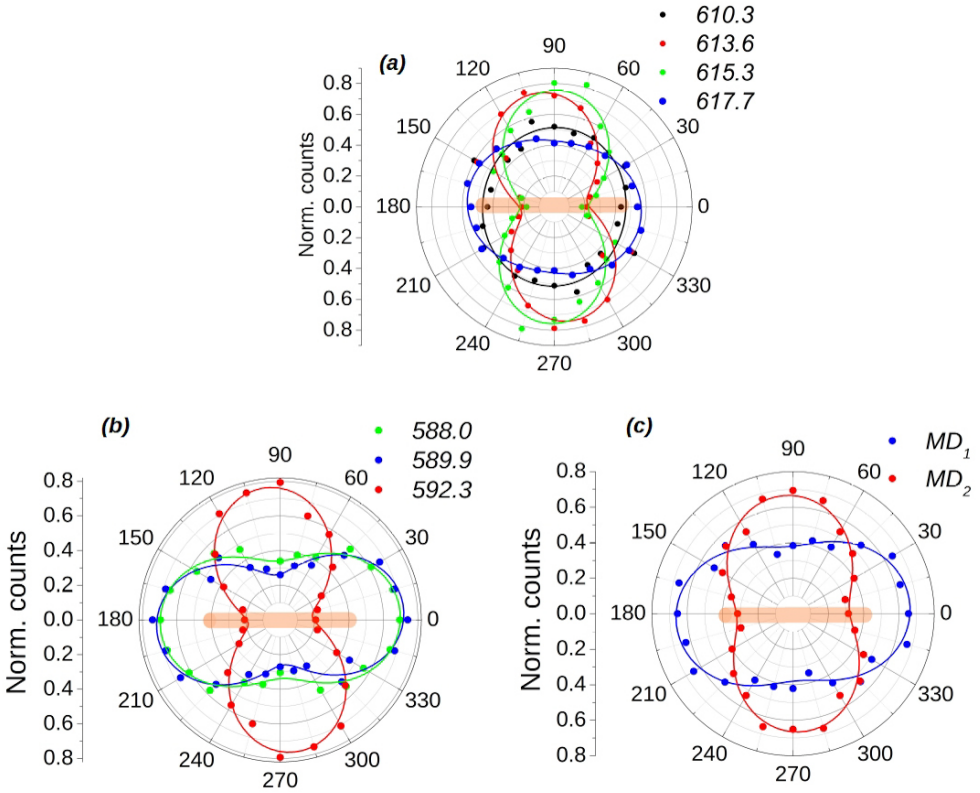

Figure 4.25: The normalized emission polar plot for (a) ED (peak fitting) (b) MD (peak fitting), and (c) MD (integrated intensity). The values are normalized using the maximum value.

chapter.

We have measured peak intensities of 0° to 180° for presenting the first half of the polar plot and then used these values for the next half 180° to 360° as a mirror image. By fitting the orthogonal polar function (eq. 4.2), nanorod orientation angle is obtained. The parameters fitted to this polar function are listed in Table 4.6. Figure 4.25(a) shows the σ-configuration for the first three peaks (610.3, 613.6, and 615.3 nm) and π-configuration for last one (617.7 nm). The 613.6 is observed with a maximum peak intensity (A,B) ratio of 3.7 with an orientation of 9°. The main influence of this dipole transition can be observed only on the two peaks 613.6 nm and 615.3 nm, whereas the other two peaks do not show much variation for spectral emission.

Further, the α angle suggests that the electric and magnetic dipole moments (p and m) are not perfectly parallel or perpendicular to nanorod c-axis. It can be estimated using the paraxial approximation discussed in the ref. [124]. It can be deduced using the A and B parameters [138]. For a ED, $A = 1/2 \cdot sin^2\alpha$ and $B = cos^2\alpha$ and for MD, $A = cos^2\alpha$ and $B = 1/2 \cdot sin^2\alpha$. In both scenario it has to satisfy the trigonometric relation as $sin^2\alpha + cos^2\alpha = 1$. The peaks at 613.6 and 615.3 nm show approximately a similar α angle about 62°.

Table 4.6: Main fitting parameters for ED and MD transitions (int.: integration over wavelength range, pf.: peak fitting).

Peak	λ [nm]	orient.	A	B	A, B ratio	φ	α
ED(pf)	610.3	σ	0.51	0.46	1.1	-7.5° ± 1.9°	47.3°
ED(pf)	613.6	σ	0.75	0.20	3.7	9.3° ± 2.1°	62.1°
ED(pf)	615.3	σ	0.76	0.22	3.5	-1.8° ± 1.7°	62.0°
ED(pf)	617.7	π	0.42	0.51	1.2	-9.2 ° ± 8.2°	44.4°
MD1 (pf)	588.0	π	0.33	0.69	2.1	2.2 ° ± 1.5°	54.9°
MD1 (pf)	589.9	π	0.26	0.72	2.8	4.9 ° ± 1.5°	59.3°
MD2 (pf)	592.3	σ	0.76	0.18	4.2	6.3° ± 1.0°	36.9°
MD1 (int.)	586.0 - 590.8	π	0.37	0.66	2.0	4.2° ± 2.0°	52.5°
MD2 (int.)	590.8 - 595.0	σ	0.66	0.31	2.1	4.0° ± 1.4°	35.7°

The influence of polarization on MD transition (586 - 595 nm) is analyzed, which revels the two distinguished subregions called MD_1 and MD_2 (Figure 4.24(b)). These spectra are fitted with three Lorentzian peaks at 588, 589.9, and 592.2 nm. The first two peaks belong to the MD_1 region with π-configuration, whereas the last one to the MD_2 regions with σ-configuration (Figure 4.25(b)). The polar fitting provides measuring with A,B ratio of 2.1, 2.8,and 4.2, respectively, for these three peaks and other fitted parameters are listed in Table 4.6. In this case, α angles are measured about 55°, 59°, and 37° for the respective peaks.

The spectra of MD_1 and MD_2 regions are intersecting at a line 590.5 nm and their peak total intensity is separately measured. The polar diagram based on the integrated intensity has revealed the configuration of MD_1 and MD_2 PL emission as σ and π-configuration (Figure 4.25(c)). The polar fitting parameters are given in Table 4.6. The both regions are appeared to have a similar peak intensity ratio about 2 and φ-values about 4°, Also, α is deduced about 52 ° and 36°, respectively for these two regions.

Compared with the integrated intensity approach, the peak fitting approach shows very high visibility, and it has resulted in a higher A/B ratio. Especially in the ED transition case, it shows no significant variation for 617.7 nm peak while the other two strong peaks show higher visibility. The polar diagram based on the integrated intensity of MD_1 and MD_2 regions has revealed the φ value about 4°, which is in excellent agreement with observed video analysis about 5°. For measuring the α angle, peak fitting clearly shows improvement because it is not very clear from the integrated intensity approach. In the case of the ED transition α is found with an angle above to 45° for σ-configuration and close to 45° for π. On the other hand, for the MD transitions, it is well below and above 45° for σ and π configurations, respectively.

Here, we compare these results with the previous one with tip contact measurements, and we have high visibility with normalized polar emission. However, no significant difference is observed. A small difference can be observed in peaks values, which differ due to the peak fitting procedure. The obtained results show a good agreement for the measured nanorod orientation angle (φ) between purely free and fiber tip-contact trapped nanorod emission. It is also in good agreement for emission spectra with two

other similar reported measurements, as we have discussed earlier [123], especially for α angle [138]. This experimental analysis suggests no such influence of tip contact environment, affecting the Eu^{3+} PL emission.

Lifetime measurement

We have measured the lifetime of Eu^{3+} PL using the trapped nanorods. The lifetime of the PL emission can be defined as the time required by a population of n electronically excited molecules to be dropped by a factor of 1/e [139]. The PL emission with the intensity $I(t)$ occurs from an excited state residue at a given time t can be given by

$$I(t) = I_0 exp(-t/\tau) \tag{4.3}$$

where I_0 is the PL intensity at $t = 0$ and τ is the PL lifetime. The τ is an intrinsic characteristic of the excited molecule, which depends on the various factors, for example, change in the chemical environment (viscosity, polarity, pH), shape, and size of the noncrystalline structure, and doping of molecular mixtures [140], [141]. Any change in these factors can easily influence the decay time.

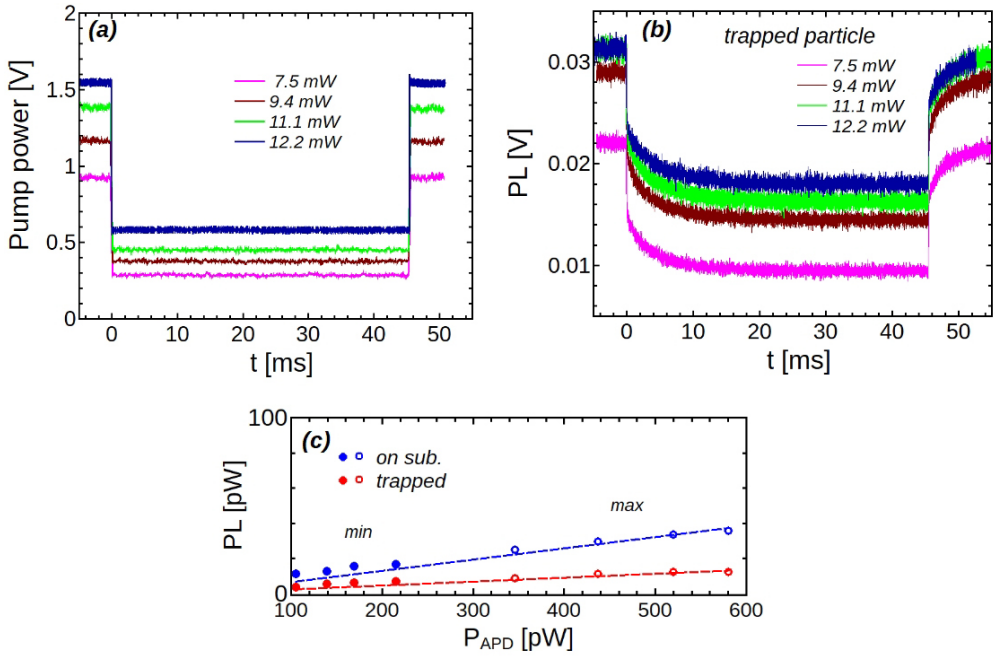

Figure 4.26: (a) Measurement of pump light intensity, which is produced after modulating with rectangular waveform (at 11 Hz) at different pump powers (P_{PM}). (b) PL emission is measured on the trapped nanorod as a function pump power. (c) The plot of PL power vs. pump power (P_{APD}) for trapped and glass substrate nanorods. (Here, P_{PM} represents the power measured using power meter whereas P_{APD} is pump power measured using APD detector.)

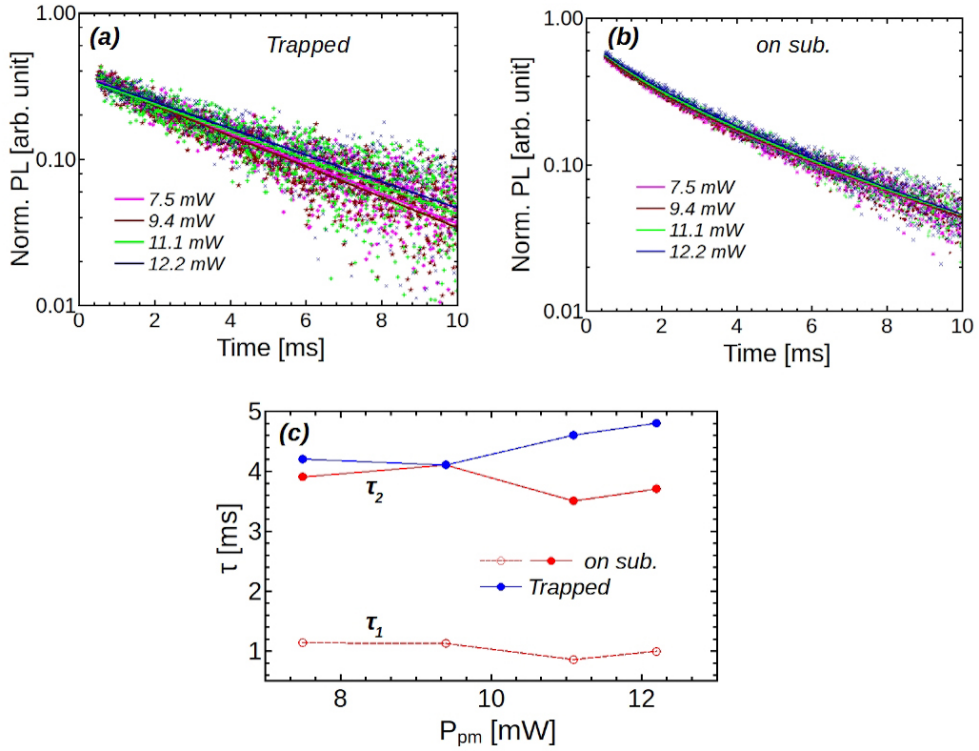

Figure 4.27: The PL lifetime measured using the exponential fitting to the experimental data for (a) trapped nanorods and (b) a cluster of 10-15 nanorods on glass-substrate. (c) A plot of τ vs. the pump power (P_{pm}) for trapped and glass-substrate nanorod.

To excite particles, we have modulated our pump laser to produce a rectangular waveform (with a decay time ≈20 μs), which is explained in Chapter 2. The PL intensity is measured at four different pump powers from 7.5 mW to 12.2 mW. These pump powers are the total output powers measured through the microscope objective. Here, we would like to mention that we are losing a high fraction of PL power (more than 50%) through the microscope objective, which has resulted in a very low signal. These signals are acquired with maximum gain ($2.65{\cdot}10^9$ V/W) of the APD detector.

Figure 4.26 (a) shows pump intensity with a direct exposure of pumping laser to APD. While in (b), the measured PL intensities using a single trapped nanorods cluster of 2 - 3 particles at the different pump power. A linear dependency is observed between PL emission and pump power 4.26 (c). Moreover, the PL emission is acquired using a cluster of 10 - 15 nanorods over a glass slide, It has also shown that its PL is depending on the pump power.

Subsequently, the acquired data are analyzed to determine the τ by fitting the exponential eq. 4.3 (Figure 4.27 (a)). These fitting are obtained for a range of 0.5 ms to 10 ms to exclude the any influence of pump on PL decays. For the trapped nanorods, the PL decay with a τ of about 4.4 ms (Figure 4.27 (c)). In the case of PL measurement on the glass substrate, numerical fitting is obtained with two decay times, representing the short τ_s and long τ_l lifetimes. The τ_s and τ_l are measured about 1 and 4 ms. The fast decay time

can be explained using the spectrum measured on the glass substrate, which shows the third observable peak at 583 nm for $^5D_1 \rightarrow {}^7D_3$ transition. This transition occurs due to the nonradiative route and has a faster decay rate than the $^5D_0$ state [137].

The Eu^{3+} PL lifetime is measured using two distinct procedures: first, a purely optically trapped in water and second, on the glass substrate. In the first case, a mono-exponential emission decay is observed while a bi-exponential decay is observed for the second case. There is no significant difference observed on τ as the function pump power. These obtained results are found in good agreement with the previously reported results [137].

4.3 Trapping of Cs_xWO_3 nanoparticles

Further, we would like to characterize a new variety of nanoparticles, those can show great potential in nanophotonic applications considering their plasmonic excitation feature [142]. This feature is based on the localize surface plasmonic resonance which arise due to the elementary excitations between photons and phonons of metallic nanparticles during light-matter interaction.

Previously, $W0_3$ nanoparticles have been reported with excellent optoelectrical properties due to their outer-d valence electrons [142]–[144]. They host localized surface plasmonic resonance and allows tuning the plasmonic resonance using Cs as a dopant. The Cs has a excellent light absorption capability in the NIR region. Due to plasmonic resonance feature, these nanoparticles are known as plasmonic oxide nanoparticles. For our trapping application, we choose the Cs_xW0_3 nanoparticles for the following reason. It works as positive charge carriers [145]–[147].

1. A well controlled elaboration process which allows procuring nanoparticles with a good crystallinity. [148], [149].
2. These nanoparticles are featured with a tunable bandgap that can be readily tuned by varying oxygen stoichiometry [142].
3. These nanoparticles have shown excellent photothermal converting feature by absorbing a light from mid-visible to NIR range [142], [150].
4. These nanoparticles are fascinating also due to their photo-catalytic feature [143].

4.3.1 Elaboration of Cs_xWO_3 nanoparticles

The Cs_xW0_3 nanoparticles elaboration is done by Yannis Cheref in the course work of his doctoral studies at PMC, Ecole Polytechnique, Palaiseau. [148]. These nanoparticles are polycrystalline nanoparticles, which are elaborated by following a solid-state synthesis process. A stoichiometric mixture of Cs_2WO_4, WO_3, and metallic tungsten powders are thoroughly grounded, then pressed into a pellet and sealed into a quartz tube at 2.2×10^{-4} mbar. Then this tube is heated in a tubular furnace at 700° C for 24 h. Then nanoparticles powder is collected and characterized in X-Ray Diffraction, which confirms a pure hexagonal phase of $Cs_{0.33}WO_3$ nanoparticles.

The obtained blue powder are grounded using a planetary ball mill and then, dispersed in isopropanol (IPA), using polyvinylpyrrolidone (PVP), a polymer, as a stabilizing agent. Over time, the larger particles of the mixture are sedimented at the bottom of the flask. In contrast, the smaller ones stay dispersed in the liquid phase. Thus, the "supernatant" samples contain only these smaller particles.

Further, the nanoparticles sample which are obtained after thoroughly stirring of the segmented mixture are reffered namely, "stirred" sample. In general, the stirred

sample contains particles of different sizes. The obtained particle sample are characterized by SEM imaging techniques at PMC. These images show "stirred" nanoparticles are appeared with a heterogeneous size distribution [148]. Thus particles are ranging from a few tens to several hundreds of nanometers for stirred nanoparticles.

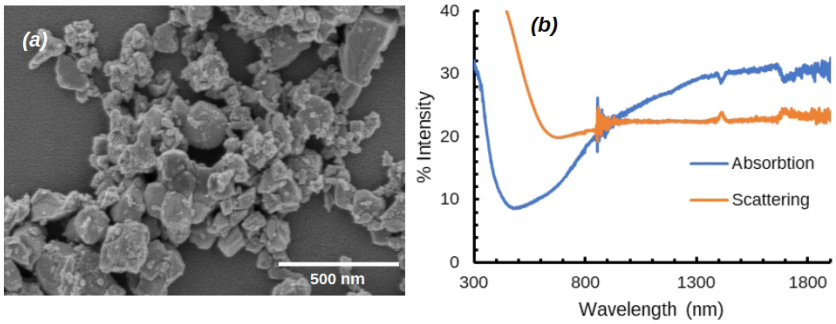

Figure 4.28: (a) SEM image of $Cs_{0.33}WO_3$ nanoparticles. (b) Absorption and scattering spectra observed in UV-Vis-NIR spectroscopy.

A fraction of elaborated samples dispersed in IPA is further diluted to preserve these samples for the optical experiment. While another fraction of the sample is diluted in tetrachloroethylene (TCE) to measure the absorption and scattering spectra in UV-Vis-NIR spectroscopy (Cary 5000, Agilent) at PMC, Ecole Polytechnique [148]. Figure 4.28 (b) shows the absorption and scattering spectra. These nanoparticles show less light absorption in the visible region, and higher light scattering in IR region.

4.3.2 Optical trapping using Fresnel lens fibers

We have observed the stable and reproducible trapping of $Cs_{0.33}WO_3$ using the Fresnel lens Fibers. The nanoparticles are trapped at a fiber-to-fiber distance (D_{f-f}) about 195 μm using the counter-propagating beams of Fresnel lens fibers. Firstly, the nanoparticle trapping is studied at different light power. Then, it is followed to observe the nanoparticle's trapping as a function of D_{f-f} by moving one of the fiber. These two trapping events are observed with two distinct $Cs_{0.33}WO_3$ nanoparticles which have been visualized in dark-field microscopy. These nanoparticles are observed with a small circular bright spot of ≈500 nm (Inset: Figure 4.29 (a)).

The single nanoparticle is first trapped at a light power of 16.4 mW and is then reduced up to 8.6 mW in a controlled manner. These trapping events are observed with one nanoparticle which remains trapped until 8.6 mW. In the distance-based trapping events, the nanoparticle trapping is observed at a light power of 16.4 mW by moving one fiber away from another for the D_{f-f} from 193 to 196.5 μm in the axial direction.

Afterward, we have analyzed the trapping videos. Figure 4.29 (a) represents the position tracking curves of the trapped nanoparticle. It shows that the residual Brownian motion of trapped nanoparticle is increasing when power is reduced. Moreover, it reveals trapping volume as anisotropic potential, which can be readily identified through their trajectories. In general, the nanoparticle is efficiently trapped in the transverse direction

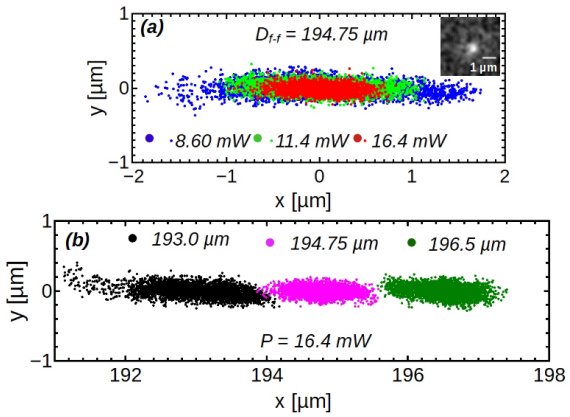

Figure 4.29: Position tracking curves of trapped $Cs_{0.33}WO_3$ nanoparticles (a) at a D_{f-f} of 194.75 µm with applying different light powers and (b) at different D_{f-f} from 193 μm to 196.5 μm with applying a light power of 16.4 mW.

but has a highly elongated trajectory in axial one. Similarly, tracking curves are also obtained for the trapping measurements of D_{f-f} variation. We have observed a high trapping stability in a transverse direction as compare to the axial direction. (Figure 4.29 (b)).

The κ values are deduced using the BS and PSA methods (Figure 4.30 (a) & (b)). The values are obtained in transverse direction since the experimental data are fitted with one Gaussian peak for both events based on light power and distance. In the axial direction, at lower light powers we observe two or more metastable trapping positions for the trapped nanoparticle. The PSA model fits very well, considering a particle size of 200 nm for the power-dependent and 350 nm for the distance-dependent measurements. However, this approximation is only working in a transverse direction for a frequency range of 1 to 120 Hz. Also, in this case, we have found the two or more metastable positions in axial directions, are usually separated by a distance about 200 nm - 1 μm between the two peaks. Figure 4.31 (a) shows that the κ is linearly depending on light power for both methods. Their normalized $\tilde{\kappa}$ values are determined to be 69.5 and 70.6 pN·μm^{-1}·W^{-1} through BS and PSA methods, respectively, in the transverse direction. Moreover, the κ values against different distance can be observed in Figure 4.31 (b). The obtained values are listed in Table 4.7. A variation in κ values corresponding to D_{f-f} can be easily seen in the given figure. Fitting a polynomial function to measure κ, we identify the most stable trapping position found at a D_{f-f} of ~195 μm. The trapping stability of trap gradually decreases when moving away from the central position.

Considering the size of nanoparticles, which is not very well known to us, it isn't easy to accurately analyze this trapping result. However, their trapping efficiency obtained by two methods are in good agreements in the transverse direction. These trapping analysis can be seen as advantages and disadvantages of these methods, BS does not require any shape and size information to deduce the κ and PSA does not require this information. In such case, the nanoparticle size measured with PSA is significant. The observation of more than one stable trapping position in the axial direction is very straight forward here. It can be accounted using the following reasons: first, the light beams are not well

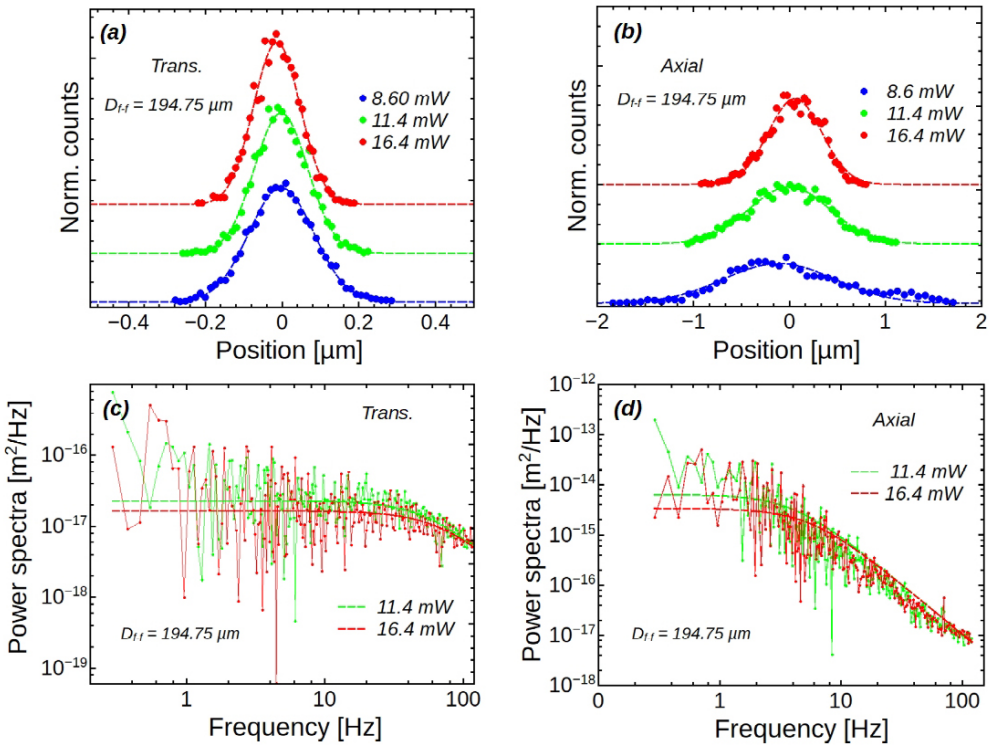

Figure 4.30: Position distribution and Gaussian fitting curve obtained applying BS method in (a) transverse and (b) axial directions. PSA fitting curves obtained in (b) transverse and (d) axial direction. The dashed lines shows the best fitting curves (Gaussian for BS and Lorentzian for PSA).

aligned, second, due to the slow mean position shift. Also, the influence of thermal scattering due to absorption of the trapping light can be neglected for these nanoparticles.

Trapping results presented here are not yet sufficient to explain the absorption feature of $Cs_{0.33}WO_3$ nanoparticles. It further requires a theoretical modeling to understand the influence of optical forces considering the absorption of 808 nm wavelength. It can also influence the plasmonic enhancement in these nanoparticle. This feature may allow us to understand the tunable plasmonic excitation in these nanoparticles based on their shape, size, and composition using a single nanoparticle (Figure 4.28 (b)).

4.4 Conclusion

In this chapter, we have presented the stable and reproducible optical trapping of dielectric particles in suspension using the fibered optical tweezers. Considering the interest of our study, this chapter focuses on two points; first, the enhancement of existing trapping efficiency using 3D printed fibers. Second, the implementation of these fibers for characterizing the anisotropic luminescent nanorods and plasmonics oxides nanoparticles.

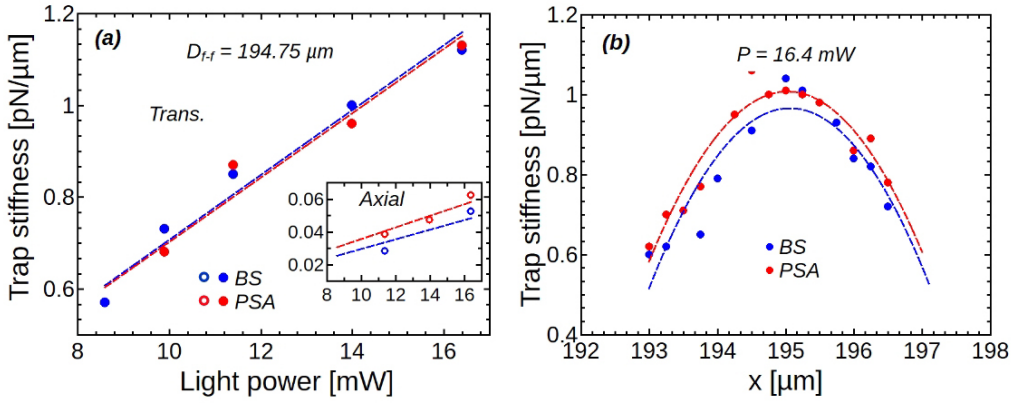

Figure 4.31: The plots of obtained κ values (a) against the used light powers at the D_{f-f} of 194.75 μm (b) at different trapping distances between the two fibers.

Table 4.7: Normalized trap stiffness $\tilde{\kappa}$ in pN·μm^{-1}·W^{-1} of $CsWO_3$ using Fresnel lens fibers obtained by BS and PSA methods. D_{f-f}: fiber-to-fiber distance

D_{f-f} (μm)	$\tilde{\kappa}$ (pN·μm^{-1}·W^{-1})			
	Transverse		Axial	
	BS	PSA	BS	PSA
194.75	69.5	70.6	2.9	3.5
193	36.6	37.8	-	-
194	48.2	-	-	-
195	63.4	61.6	-	-
196	51.2	52.4	-	-

In the first part of this chapter, we have shown the implementation of two new microstructured fibers; Fresnel lens and TIR-probe to our suspension fibered tweezers. The Fresnel lens fibers allow us to achieve very high trapping efficiency in counter-propagating geometry of their two identical fibers of the same N.A. The N.A. of 0.5 Fresnel lens fibers are measured with an excellent trapping performance ($\tilde{\kappa}$ = 1769 pN·μm^{-1}·W^{-1}) for the 1 μm spherical particles at a 195 μm fiber-to-fiber distance (D_{f-f}) in comparison with two other N.A. of 0.3 and 0.7. It also shows a good trapping performance for 0.5 μm particles at the same (D_{f-f}). Further in this part, a TIR-probe fiber is characterized with good trapping efficiency ($\tilde{\kappa}$ = ~98 pN·μm^{-1}·W^{-1}) for a 0.5 μm particles at 45 μm distance.

In the second part, we have discussed the optical trapping of anisotropic $NaYF_4$:Eu nanorods, implementing the two distinct structured fiber based tweezers: tapered fiber tips and Fresnel lens. These experimental characterizations are presented based on the different scenarios of nanorods trapping, first trapping in fiber tip contact (using tapered fiber tip) and second far-field trapping using a counter–propagating approach (using Fresnel lens). These stable nanorod trapping events are exploited to study the anisotropic Eu^{3+} PL emission based on the electric and magnetic dipole transitions. Moreover, we have characterized polarization-dependent feature of the PL emission to determine σ and π featured emissions for these two transitions. Furthermore, the high trapping sta-

bility with the Fresnel lens allows for measuring the lifetime of about 4.4 ms for Eu^{3+} PL emission. Here, we have shown that the spectroscopic investigation can be used to determine the nanorod orientation similar to the trapping video observations.

Finally, in the last part, we have discussed the optical trapping of $Cs_{0.33}WO_3$ nanoparticles, which are aimed to study their absorption properties. The counter–propagating beams of Fresnel lens fibers provided stable and reproducible trapping the 200 nm - 350 nm nanoparticles. The particle trapping at different distance shows the trapping stability can be controlled by approaching the equilibrium position. This experiment is yet not sufficient to describe overall trapping feature of $Cs_{0.33}WO_3$ nanoparticles at a single particle level. It further requires a theoretical study to understand the optical applies experienced by particle, accounting for the absorptive nature of these nanoparticles.

Conclusion and perspectives

This Ph.D. thesis aims to study the optical trapping of nanoparticles separately in air and water using fibered optical tweezers. In this context, we are developing an experimental fibered tweezers setup dedicated to particle trapping in air. For this experimental development, we have performed optical manipulations of water aerosols and polystyrene particles using a tapered fiber tip, which produces a diverging light beam. These experimental studies have shown the difficulties for particle trapping using diverging beams. Later, the particle manipulation is studied using two other fibers, negative axicon, and positive axicon fibers, having a relatively lesser diverging beams. It has been observed that manipulated particles are not moving towards the center of the light beam instead they are being pushed away from the beam center in transverse direction. Numerical simulations have been performed to confirmed the experimental measurements. Due to this influence, manipulated particles are pushed away from the beam center in the transverse direction. These results shows that the particles trapping using the fibers with a diverging beam is not possible. We are also considering developing a micro-structured fiber that can provide a stronger beam gradient to attract the particle for trapping in air.

On the other hand, a well developed experimental setup working in water allows stable trapping of suspended particles using two tapered fiber tips in counter-propagating geometry. To further enhance the trapping performance of this setup, we have employed 3D printed Fresnel lens fibers, which allow converging the light beams at a particular distance corresponding to their focal length. In a comparative study using Fresnel lens fibers of three different N.A. = 0.3, 0.5, and 0.7, we have performed a stable and reproducible optical trapping of a polystyrene particle (1 μm) at three different trapping distances corresponding to twice of their focal lengths. The fibers having an N.A. of 0.5 are found to have the highest trapping efficiency for a fiber-to-fiber distance of about 200 μm. Using the Fresnel lens fibers (N.A. = 0.5), we have achieved the highest trapping efficiency of about 1763 and 50 pN$\cdot\mu m^{-1}\cdot$W^{-1} in the transverse and axial direction, respectively, for this experimental setup. Also, we can perform an efficient particle trapping with even very low light power down to 200 μW.

We have also demonstrated a very stable particle (0.5 and 1 μm) trapping in a single fiber geometry using 3D printed TIR-probe fiber. The fiber has enabled an optical trap by focusing annular beam at distance of about 45 μm. Using a TIR-probe fiber, we have achieved high trapping stability in both, transverse and axial directions. It is highly versatile for manipulating and transporting the microscopic objects three-dimensionally.

Further, in our experimental work, we have investigated the optical trapping of anisotropic $NaYF_4$:Eu^{3+} nanorods with a high aspect ratio (1.2 μm and 120 nm in length and diameter, respectively). This nanorod trapping is one of the objectives of this thesis to characterize anisotropic Eu^{3+} PL emission. This characterization is performed in two following scenarios, first trapping with a diverging beam and second, using a converging beam. In the first case, we have studied stably trapped nanorods in tip-contact to the tapered fiber tip. In this contact-based trapping, the nanorods are preferentially aligned nearly parallel to the fiber axis. This trapping event is exploited for measuring the emission in two orthogonal directions, perpendicular and parallel to the nanorod axis. The measured spectra have allowed us to characterize the electric and magnetic dipole transitions emission. Moreover, polarization dependency of Eu^{3+} emission is observed in perpendicular direction, while the emission remains polarization-independent in the parallel direction. The measured polarization-dependent spectra have allowed determining the polarized emission in the form of σ and π-configurations for these two transitions. Using this spectroscopic investigation, we have determined a nanorod orientation of about 8° to 10° with respect to the fiber axis. These results show that the nanorod orientation can be determined by spectroscopic means, which can be much faster than using video observations.

Further, contact-free, stable nanorod trapping is studied using the Fresnel lens fibers. In this experiment, we have characterized the number of trapped nanorods inside the optical trap by observing the PL intensity. It has allowed studying the nanorod trapping as a function of the number of nanorods. The Nanorod trapping efficiency is increasing if the number of nanorods increases. Moreover, the nanorod trapping is used for studying the polarization-dependent emission, which has allowed determining the σ and π-configurations of the electric and magnetic dipole transitions and the nanorod orientation. It has allowed determining the angle between electric or magnetic dipole moments and the crystallographic axis of nanorods. Furthermore, we have measured the lifetime of PL decay on an optically trapped nanorod cluster (two or more than two nanorods) about to 4.4 ms.

Finally, in our recent work, we have demonstrated stable trapping of $Cs_{0.33}WO_3$ nanoparticles (with a size of 200 nm - 350 nm) using the Fresnel lens fibers. Their trapping efficiency is determined to be 70 and 3.5 $pN{\cdot}\mu m^{-1}{\cdot}W^{-1}$ in the transverse and axial direction. The obtained trapping efficiently are found in good agreement with two complementary models (BS and PSA) which have been used for characterizing these measurements.

To conclude this manuscript based on the experimental work, the air-tweezers setup is still developing to realize the particle trapping. It further opens the possibilities to explore these experimental studies using the new microstructured fibers. In this perspective, the theoretical characterization of fiber performance will help in designing such a fiber that allows achieving a higher attracting force in the transverse direction.

Our suspension tweezers are sufficiently matured to characterize the micro and nanoparticles using nanostructured fibers. Moreover, we are further working to enhance the trapping stability as well as the setup's flexibility by exploring microstructured optical fibers in the particle trapping experiments. Besides, it also offers the following

interesting perspectives that can be realized in the near future.

- As we have seen, the use of 3D printed fibers has provided an efficient optical tweezing technique. In the future, it can allow the integration of a microfluidic channel for the experimental characterization of nanoparticles as well as biological molecules efficiently [151]. It can also be interesting to explore optical trapping with a beam configuration other than the fundamental mode of the light beam (Gaussian beam). The use of advanced beams such as the Laguerre-Gaussian beam (which is associated with the orbital angular momentum (OAM) of light) can allow studying the influence of light OAM on the particles [152]. This kind of fibers will allow spinning or rotating a nanoparticle efficiently [153] and useful for studying spin relaxometry with optically trapped nanoparticles [154].
- Another perspective is to facilitate this experimental setup for characterizing the luminescent feature of nanoparticles based on their crystal structure, anisotropy, doping, the influence of host matrix, the polarization of the incident light beam. It can allow quantifying the influence of the local environment and orientation on their luminescent features. It can also be benefited to study the PL decay rates of particular transitions at a single molecular level [137]. Moreover, our tweezers setup can be used for optical trapping and manipulation of biological samples and other nanostructured having the PL emission.
- The optical trapping of plasmonic oxide nanoparticles is still a perspective for studying their important feature of plasmonic excitation [150]. Also, our experimental setup can be used for investigating the optical properties of noble metal nanoparticles, which have triggered wide interest in linear optics due to the existence of localized plasmon resonances [82].

Bibliography

[1] A. Ashkin, J. M. Dziedzic, J. E. Bjorkholm, and S. Chu, "Observation of a single-beam gradient force optical trap for dielectric particles," *Opt. Lett.*, vol. 11, pp. 288–290, 1986 (cited on pages - x, 2).

[2] J.-B. Decombe, S. Huant, and J. Fick, "Single and dual fiber nano-tip optical tweezers: Trapping and analysis," *Opt. Express*, vol. 21, p. 30 521, 2013 (cited on pages - xi, 15, 24, 25, 28–30, 37, 39, 41, 46, 49, 56, 64).

[3] J.-B. Decombe, F. J. Valdivia-Valero, G. Dantelle, G. Lemenager, T. Gacoin, G. Colas des Francs, S. Huant, and J. Fick, "Luminescent nanoparticle trapping with far-field optical fiber-tip tweezers," *Nanoscale*, vol. 8, pp. 5334–5342, 2016 (cited on pages - xi, 15, 49, 62).

[4] G. Leménager, K. Lahlil, T. Gacoin, G. Colas des Francs, and J. Fick, "Optical fiber tip tweezers, a complementary approach for nanoparticle trapping," *J Nanophotonics*, vol. 13, p. 012 505, 2018 (cited on pages - xi, 15, 16, 25, 62, 69).

[5] S. Kotsifaki D. G. and Nic Chormaic, "Plasmonic optical tweezersbased on nanostructures: Fundamentals, advances and prospects," *Nanophotonics*, vol. 87, pp. 1227–1245, 2019 (cited on pages - 1, 6, 8).

[6] T. H. Maiman, "Stimulated optical radiation in ruby," *Nature*, vol. 187, no. 4736, pp. 493–494, 1960 (cited on page - 1).

[7] A. Ashkin, "Acceleration and trapping of particles by radiation pressure," *Phys. Rev. Lett.*, vol. 24, pp. 156–159, 1970 (cited on page - 2).

[8] A. Ashkin and J. Dziedzic, "Optical levitation by radiation pressure," *Appl. Phys. Lett.*, vol. 19, pp. 283–285, 1971 (cited on page - 2).

[9] A. Ashkin and J. Dziedzic, "Optical trapping and manipulation of viruses and bacteria," *Science*, vol. 235, pp. 1517–1520, 1987 (cited on page - 2).

[10] O. M. Maragò, P. H. Jones, P. G. Gucciardi, G. Volpe, and A. C. Ferrari, "Optical trapping and manipulation of nanostructures," *Nat. Nanotechnol.*, vol. 8, p. 807, 2013 (cited on pages - 2, 4, 6, 8, 10).

[11] J. E. Molloy and M. J. Padgett, "Lights, action: Optical tweezers," *Contemp. Phys*, vol. 43, pp. 241–258, 2002 (cited on pages - 2–4, 8).

[12] D. G. Grier, "A revolution in optical manipulation," *Nature*, vol. 424, p. 810, 2003 (cited on pages - 2, 3, 8, 9).

[13] P. H. Jones, O. M. Maragò, and G. Volpe, *Optical tweezers: Principles and applications*. Cambridge University Press, 2015 (cited on pages - 2, 4, 5).

[14] M. D. Koch and J. W. Shaevitz, *Optical Tweezers*. Springer New York, 2016 (cited on page - 2).

[15] G. Roosen and C. Imbert, "Optical levitation by means of two horizontal laser beams: A theoretical and experimental study," *Phy. Lett. A*, vol. 59, pp. 6–8, 1976 (cited on page - 4).

[16] M. Dienerowitz, M. Mazilu, and K. Dholakia, "Optical manipulation of nanoparticles: A review," *J. Nanophotonics*, vol. 2, p. 021 875, 2008 (cited on pages - 4, 6–8).

[17] Y.-R. Chang, L. Hsu, and S. Chi, "Optical trapping of a spherically symmetric sphere in the ray-optics regime: A model for optical tweezers upon cells," *App. Opt.*, vol. 45, pp. 3885–3892, 2006 (cited on page - 5).

[18] J.-B. Decombe, "Development and application of nanostructured fibers optical tweezers," Ph.D. dissertation, Université Grenoble Alpes, Grenoble, France, 2015 (cited on pages - 7, 15, 29, 37).

[19] A. Salandrino, S. Fardad, and D. N. Christodoulides, "Generalized mie theory of optical forces," *J. Opt. Soc. Am B*, vol. 29, pp. 855–866, 2012 (cited on page - 7).

[20] R. V. Jones, "Radiation pressure of light in a dispersive medium," *Proc. R. Soc. Lond*, vol. 360, pp. 365–371, 1978 (cited on page - 8).

[21] S. M. Block, D. F. Blair, and H. C. Berg, "Compliance of bacterial flagella measured with optical tweezers," *Nature*, vol. 338, pp. 514–518, 1989 (cited on page - 8).

[22] K. Svoboda and S. M. Block, "Biological applications of optical forces," *Annu. Rev. Biophys.*, vol. 23, pp. 247–285, 1994 (cited on page - 8).

[23] S. Kawata and T. Sugiura, "Movement of micrometer-sized particles in the evanescent field of a laser beam," *Opt. Lett.*, vol. 17, pp. 772–774, 1992 (cited on page - 8).

[24] K. Svoboda and S. M. Block, "Optical trapping of metallic rayleigh particles," *Opt. Lett.*, vol. 19, pp. 930–932, 1994 (cited on page - 8).

[25] P. T. Korda, M. B. Taylor, and D. G. Grier, "Kinetically locked-in colloidal transport in an array of optical tweezers," *Physical review letters*, vol. 89, no. 12, p. 128 301, 2002 (cited on page - 8).

[26] M. P. MacDonald, G. C. Spalding, and K. Dholakia, "Microfluidic sorting in an optical lattice," *Nature*, vol. 426, pp. 421–424, 2003 (cited on page - 8).

[27] J. E. Curtis, B. A. Koss, and D. G. Grier, "Dynamic holographic optical tweezers," *Opt. Commun.*, vol. 207, pp. 169–175, 2002 (cited on pages - 8, 9).

[28] P. Bassindale, D. Phillips, A. Barnes, and B. Drinkwater, "Measurements of the force fields within an acoustic standing wave using holographic optical tweezers," *Appl. Phys. Lett.*, vol. 104, p. 163 504, 2014 (cited on page - 8).

[29] F. Hörner, R. Meissner, S. Polali, J. Pfeiffer, T. Betz, C. Denz, and E. Raz, "Holographic optical tweezers-based in vivo manipulations in zebrafish embryos," *J. Biophotonics*, vol. 10, no. 11, pp. 1492–1501, 2017 (cited on page - 8).

[30] B. Cao, L. Kelbauskas, S. Chan, R. M. Shetty, D. Smith, and D. R. Meldrum, "Rotation of single live mammalian cells using dynamic holographic optical tweezers," *Opt. Laser. Eng.*, vol. 92, pp. 70–75, 2017 (cited on page - 8).

[31] C.-Y. Li, D. Cao, C.-B. Qi, Y.-F. Kang, C.-Y. Song, D.-D. Xu, B. Zheng, D.-W. Pang, and H.-W. Tang, "Combining holographic optical tweezers with upconversion luminescence encoding: Imaging-based stable suspension array for sensitive responding of dual cancer biomarkers," *Anal. Chem.*, vol. 90, pp. 2639–2647, 2018 (cited on pages - 8, 9).

[32] M. Righini, A. S. Zelenina, C. Girard, and R. Quidant, "Parallel and selective trapping in a patterned plasmonic landscape," *Nature Physics*, vol. 3, pp. 477–480, 2007 (cited on pages - 8, 9).

[33] K. C. Toussaint Jr, B. J. Roxworthy, S. Michaud, H. Chen, A. M. Bhuiya, and Q. Ding, "Plasmonic nanoantennas: From nanotweezers to plasmonic photography," *Optics Photonics News*, vol. 26, pp. 24–31, 2015 (cited on page - 8).

[34] P. R. Huft, J. D. Kolbow, J. T. Thweatt, and N. C. Lindquist, "Holographic plasmonic nanotweezers for dynamic trapping and manipulation," *Nano Lett.*, vol. 17, pp. 7920–7925, 2017 (cited on page - 8).

[35] P. Rodrıguez-Sevilla, L. Labrador-Páez, D. Jaque, and P. Haro-González, "Optical trapping for biosensing: Materials and applications," *J. Mater. Chem. B*, vol. 5, pp. 9085–9101, 2017 (cited on page - 8).

[36] J. van Mameren, M. Modesti, R. Kanaar, C. Wyman, G. J. Wuite, and E. J. Peterman, "Dissecting elastic heterogeneity along dna molecules coated partly with Rad51 sing concurrent fluorescence microscopy and optical tweezers," *Biophys. J.*, vol. 91, pp. L78–L80, 2006 (cited on page - 8).

[37] C. Monico, M. Capitanio, G. Belcastro, F. Vanzi, and F. S. Pavone, "Optical methods to study protein-dna interactions in vitro and in living cells at the single-molecule level," *Int. J. Mol. Sci.*, vol. 14, pp. 3961–3992, 2013 (cited on page - 8).

[38] X. Gou, H. C. Han, S. Hu, A. Y. Leung, and D. Sun, "Applying combined optical tweezers and fluorescence microscopy technologies to manipulate cell adhesions for cell-to-cell interaction study," *IEEE. Trans. Biomed. Eng.*, vol. 60, pp. 2308–2315, 2013 (cited on page - 8).

[39] G. Sirinakis, Y. Ren, Y. Gao, Z. Xi, and Y. Zhang, "Combined versatile high-resolution optical tweezers and single-molecule fluorescence microscopy," *Rev. Sci. Instrum.*, vol. 83, p. 093 708, 2012 (cited on page - 8).

[40] A. A. Al Balushi, A. Kotnala, S. Wheaton, R. M. Gelfand, Y. Rajashekara, and R. Gordon, "Label-free free-solution nanoaperture optical tweezers for single molecule protein studies," *Analyst*, vol. 140, pp. 4760–4778, 2015 (cited on page - 8).

[41] A. Magazzú, D. Spadaro, M. Donato, R. Sayed, E. Messina, C. D'Andrea, A. Foti, B. Fazio, M. Iati, A. Irrera, *et al.*, "Optical tweezers: A non-destructive tool for soft and biomaterial investigations," *Rend. Fis. Acc. Lincei*, vol. 26, pp. 203–218, 2015 (cited on page - 8).

[42] S. Simmert, M. K. Abdosamadi, G. Hermsdorf, and E. Schäffer, "Led-based interference-reflection microscopy combined with optical tweezers for quantitative three-dimensional microtubule imaging," *Opt. Express*, vol. 26, pp. 14 499–14 513, 2018 (cited on page - 8).

[43] D. Choudhary, A. Mossa, M. Jadhav, and C. Cecconi, "Bio-molecular applications of recent developments in optical tweezers," *Biomolecules*, vol. 9, p. 23, 2019 (cited on pages - 8, 9).

[44] P. J. Reece, S. Paiman, O. Abdul-Nabi, Q. Gao, M. Gal, H. H. Tan, and C. Jagadish, "Combined optical trapping and microphotoluminescence of single inp nanowires," *Appl. Phys. Lett.*, vol. 95, p. 101 109, 2009 (cited on pages - 9, 10).

[45] H. Xu, Q. Li, L. Wang, Y. He, J. Shi, B. Tang, and C. Fan, "Nanoscale optical probes for cellular imaging," *Chem. Soc. Rev.*, vol. 43, no. 8, pp. 2650–2661, 2014 (cited on page - 9).

[46] R. He, J. R. V. de Aldana, G. L. Pedrola, F. Chen, and D. Jaque, "Two-photon luminescence thermometry: Towards 3d high-resolution thermal imaging of waveguides," *Opt. Express*, vol. 24, pp. 16 156–16 166, 2016 (cited on page - 9).

[47] P. Rodrıguez-Sevilla, L. Labrador-Páez, D. Wawrzyńczyk, M. Nyk, M. Samoć, A. K. Kar, M. D. Mackenzie, L. Paterson, D. Jaque, and P. Haro-González, "Determining the 3d orientation of optically trapped upconverting nanorods by in situ single-particle polarized spectroscopy," *Nanoscale*, vol. 8, pp. 300–308, 2016 (cited on page - 9).

[48] A. D. Pickel, A. Teitelboim, E. M. Chan, N. J. Borys, P. J. Schuck, and C. Dames, "Apparent self-heating of individual upconverting nanoparticle thermometers," *Nat. commun.*, vol. 9, no. 1, pp. 1–12, 2018 (cited on page - 9).

[49] F. Wang, P. J. Reece, S. Paiman, Q. Gao, H. H. Tan, and C. Jagadish, "Nonlinear optical processes in optically trapped inp nanowires," *Nano Lett.*, vol. 11, no. 10, pp. 4149–4153, 2011 (cited on page - 10).

[50] F. Wang, W. J. Toe, W. M. Lee, D. McGloin, Q. Gao, H. H. Tan, C. Jagadish, and P. J. Reece, "Resolving stable axial trapping points of nanowires in an optical tweezers using photoluminescence mapping," *Nano Lett.*, vol. 13, pp. 1185–1191, 2013 (cited on page - 10).

[51] L. P. Neukirch, J. Gieseler, R. Quidant, L. Novotny, and A. N. Vamivakas, "Observation of nitrogen vacancy photoluminescence from an optically levitated nanodiamond," *Opt. Lett.*, vol. 38, pp. 2976–2979, 2013 (cited on pages - 10, 11).

[52] K. Wei, Z. Xu, R. Chen, X. Zheng, X. Cheng, and T. Jiang, "Temperature-dependent excitonic photoluminescence excited by two-photon absorption in perovskite cspbbr 3 quantum dots," *Opt. Lett.*, vol. 41, pp. 3821–3824, 2016 (cited on page - 10).

[53] S. Drobczyński, K. Prorok, K. Tamarov, K. Duś-Szachniewicz, V.-P. Lehto, and A. Bednarkiewicz, "Toward controlled photothermal treatment of single cell: Optically induced heating and remote temperature monitoring in vitro through double wavelength optical tweezers," *ACS Photonics*, vol. 4, pp. 1993–2002, 2017 (cited on page - 10).

[54] H. Rodrıguez-Rodrıguez, M. Acebrón, F. J. Iborra, J. R. Arias-Gonzalez, and B. H. Juárez, "Photoluminescence activation of organic dyes via optically trapped quantum dots," *ACS Nano*, vol. 13, pp. 7223–7230, 2019 (cited on page - 10).

[55] F. M. Mor, A. Sienkiewicz, L. Forró, and S. Jeney, "Upconversion particle as a local luminescent brownian probe: A photonic force microscopy study," *ACS Photonics*, vol. 1, pp. 1251–1257, 2014 (cited on page - 10).

[56] C. D. Brites, X. Xie, M. L. Debasu, X. Qin, R. Chen, W. Huang, J. Rocha, X. Liu, and L. D. Carlos, "Instantaneous ballistic velocity of suspended brownian nanocrystals measured by upconversion nanothermometry," *Nat. Nanotechnol.*, vol. 11, pp. 851–856, 2016 (cited on page - 10).

[57] J. Dong, W. Gao, Q. Han, Y. Wang, J. Qi, X. Yan, and M. Sun, "Plasmon-enhanced upconversion photoluminescence: Mechanism and application," *Rev. Phys.*, vol. 4, p. 100 026, 2019 (cited on page - 10).

[58] R. Borja-Urby, L. Diaz-Torres, P. Salas, C. Angeles-Chavez, and O. Meza, "Strong broad green uv-excited photoluminescence in rare earth doped barium zirconate," *Mater Sci Eng B*, vol. 176, pp. 1388–1392, 2011 (cited on page - 10).

[59] R. Kolesov, K. Xia, R. Reuter, R. Stöhr, A. Zappe, J. Meijer, P. Hemmer, and J. Wrachtrup, "Optical detection of a single rare-earth ion in a crystal," *Nat. Commun*, vol. 3, pp. 1–7, 2012 (cited on page - 10).

[60] I. Hyppänen, N. Höysniemi, R. Arppe, M. Schäferling, and T. Soukka, "Environmental impact on the excitation path of the red upconversion emission of nanocrystalline $NaYF_4$: Yb^{3+} Er^{3+}," *J. Phys. Chem. C*, vol. 121, pp. 6924–6929, 2017 (cited on page - 10).

[61] P. Haro-Gonzalez, B. Del Rosal, L. M. Maestro, E. M. Rodriguez, R. Naccache, J. Capobianco, K. Dholakia, J. G. Sole, and D. Jaque, "Optical trapping of $NaYF_4$: Er^{3+}, Yb^{3+} upconverting fluorescent nanoparticles," *Nanoscale*, vol. 5, pp. 12 192–12 199, 2013 (cited on page - 10).

[62] P. Rodrıguez-Sevilla, H. Rodrıguez-Rodrıguez, M. Pedroni, A. Speghini, M. Bettinelli, J. G. Solé, D. Jaque, and P. Haro-González, "Assessing single upconverting nanoparticle luminescence by optical tweezers," *Nano Lett.*, vol. 15, pp. 5068–5074, 2015 (cited on pages - 10, 11).

[63] Y.-F. Kang, B. Zheng, C.-Y. Song, C.-Y. Li, Z.-L. Chen, Q.-S. Wu, Y. Yang, D.-W. Pang, and H.-W. Tang, "Evaluation of luminescence properties of single hydrophilic upconversion nanoparticles by optical trapping," *J. Phys. Chem. C*, vol. 123, pp. 10 107–10 113, 2019 (cited on page - 10).

[64] S. F. Himmelstoß and T. Hirsch, "A critical comparison of lanthanide based upconversion nanoparticles to fluorescent proteins, semiconductor quantum dots, and carbon dots for use in optical sensing and imaging," *Methods App. Fluores.*, vol. 7, p. 022 002, 2019 (cited on page - 10).

[65] S. Jones, A. A. Al Balushi, and R. Gordon, "Raman spectroscopy of single nanoparticles in a double-nanohole optical tweezer system," *J. Opt.*, vol. 17, p. 102 001, 2015 (cited on page - 10).

[66] J. F. Davies and K. R. Wilson, "Raman spectroscopy of isotopic water diffusion in ultraviscous, glassy, and gel states in aerosol by use of optical tweezers," *Analyt. Chem.*, vol. 88, pp. 2361–2366, 2016 (cited on page - 10).

[67] J. W. Black, M. Kamenetska, and Z. Ganim, "An optical tweezers platform for single molecule force spectroscopy in organic solvents," *Nano Lett.*, vol. 17, pp. 6598–6605, 2017 (cited on page - 10).

[68] R. Omori, T. Kobayashi, and A. Suzuki, "Observation of a single-beam gradient-force optical trap for dielectric particles in air," *Opt. Lett.*, vol. 22, pp. 816–818, 1997 (cited on page - 10).

[69] N. Magome, M. I. Kohira, E. Hayata, S. Mukai, and K. Yoshikawa, "Optical trapping of a growing water droplet in air," *J. Phys. Chem. B*, vol. 107, pp. 3988–3990, 2003 (cited on page - 10).

[70] D. McGloin, "Optical tweezers: 20 years on," *Philos. Trans. R. Soc. A*, vol. 364, pp. 3521–3537, 2006 (cited on page - 10).

[71] Z. Gong, Y.-L. Pan, G. Videen, and C. Wang, "Optical trapping and manipulation of single particles in air: Principles, technical details, and applications," *J. Quant. Spectrosc. Radiat. Transf.*, vol. 214, pp. 94–119, 2018 (cited on page - 10).

[72] A. van der Horst, P. D. van Oostrum, A. Moroz, A. van Blaaderen, and M. Dogterom, "High trapping forces for high-refractive index particles trapped in dynamic arrays of counterpropagating optical tweezers," *Appl Opt.*, vol. 47, pp. 3196–3202, 2008 (cited on page - 10).

[73] D. Burnham and D. McGloin, "Holographic optical trapping of aerosol droplets," *Opt. express*, vol. 14, pp. 4175–4181, 2006 (cited on pages - 11, 17, 43).

[74] M. Summers, J. Reid, and D. McGloin, "Optical guiding of aerosol droplets," *Opt. Express*, vol. 14, pp. 6373–6380, 2006 (cited on page - 11).

[75] D. R. Burnham and D. McGloin, "Modeling of optical traps for aerosols," *J. Opt. Soc. Am. B*, vol. 28, pp. 2856–2864, 2011 (cited on pages - 11, 22).

[76] J. R. Butler, J. B. Wills, L. Mitchem, D. R. Burnham, D. McGloin, and J. P. Reid, "Spectroscopic characterisation and manipulation of arrays of sub picolitre aerosol droplets," *Lab Chip*, vol. 9, pp. 521–528, 2009 (cited on page - 11).

[77] V. G. Shvedov, A. S. Desyatnikov, A. V. Rode, W. Krolikowski, and Y. S. Kivshar, "Optical guiding of absorbing nanoclusters in air," *Opt. Express*, vol. 17, pp. 5743–5757, 2009 (cited on page - 11).

[78] V. G. Shvedov, A. V. Rode, Y. V. Izdebskaya, A. S. Desyatnikov, W. Krolikowski, and Y. S. Kivshar, "Giant optical manipulation," *Phys. Rev. Lett.*, vol. 105, p. 118 103, 2010 (cited on page - 11).

[79] Y.-L. Pan, S. C. Hill, and M. Coleman, "Photophoretic trapping of absorbing particles in air and measurement of their single-particle raman spectra," *Opt. Express*, vol. 20, no. 5, pp. 5325–5334, 2012 (cited on page - 11).

[80] Z. Gong, Y.-L. Pan, and C. Wang, "Optical configurations for photophoretic trap of single particles in air," *Rev. Sci. Instrum.*, vol. 87, p. 103 104, 2016 (cited on page - 11).

[81] C. Wang, Z. Gong, Y.-L. Pan, and G. Videen, "Laser pushing or pulling of absorbing airborne particles," *Appl.Phys. Lett.*, vol. 109, p. 011 905, 2016 (cited on page - 11).

[82] L. Jauffred, S. M.-R. Taheri, R. Schmitt, H. Linke, and L. B. Oddershede, "Optical trapping of gold nanoparticles in air," *Nano Lett.*, vol. 15, pp. 4713–4719, 2015 (cited on pages - 12, 17, 92).

[83] A. Constable, J. Kim, J. Mervis, F. Zarinetchi, and M. Prentiss, "Demonstration of a fiber-optical light-force trap," *Opt lett*, vol. 18, pp. 1867–1869, 1993 (cited on page - 12).

[84] C. Liberale, G. Cojoc, F. Bragheri, P. Minzioni, G. Perozziello, R. La Rocca, L. Ferrara, V. Rajamanickam, E. Di Fabrizio, and I. Cristiani, "Integrated microfluidic device for single-cell trapping and spectroscopy," *Sci Rep*, vol. 3, p. 1258, 2013 (cited on page - 13).

[85] E. Lyons and G. Sonek, "Confinement and bistability in a tapered hemispherically lensed optical fiber trap," *Appl. Phys. Lett.*, vol. 66, no. 13, pp. 1584–1586, 1995 (cited on page - 12).

[86] R. Taylor, C. Hnatovsky, E. Simova, D. Rayner, V. Bhardwaj, and P. Corkum, "Femtosecond laser fabrication of nanostructures in silica glass," *Opt; Lett.*, vol. 28, pp. 1043–1045, 2003 (cited on page - 12).

[87] Z. Liu, C. Guo, J. Yang, and L. Yuan, "Tapered fiber optical tweezers for microscopic particle trapping: Fabrication and application," *Opt Express*, vol. 14, pp. 12 510–12 516, 2006 (cited on page - 12).

[88] S. K. Mohanty, K. Mohanty, and M. W. Berns, "Manipulation of mammalian cells using a single-fiber optical microbeam," *J. Biomed. Opt.*, vol. 13, p. 054 049, 2008 (cited on page - 12).

[89] R. S. Rodrigues Ribeiro, O. Soppera, A. G. Oliva, A. Guerreiro, and P. A. S. Jorge, "New trends on optical fiber tweezers," *Journal of Lightwave Technology*, vol. 33, pp. 3394–3405, 2015 (cited on page - 13).

[90] S. Valkai, L. Oroszi, and P. Ormos, "Optical tweezers with tips grown at the end of fibers by photopolymerization," *App Opt.*, vol. 48, pp. 2880–2883, 2009 (cited on page - 13).

[91] R. S. R. Ribeiro, R. Queirós, O. Soppera, A. Guerreiro, and P. A. Jorge, "Optical fiber tweezers fabricated by guided wave photo-polymerization," vol. 2, pp. 634–645, 2015 (cited on page - 13).

[92] X. Xu, C. Cheng, H. Xin, H. Lei, and B. Li, "Controllable orientation of single silver nanowire using two fiber probes," *Sci. Rep.*, vol. 4, p. 3989, 2014 (cited on pages - 13, 14).

[93] R. S. R. Ribeiro, P. Dahal, A. Guerreiro, P. A. Jorge, and J. Viegas, "Fabrication of fresnel plates on optical fibres by fib milling for optical trapping, manipulation and detection of single cells," *Sci. Rep.*, vol. 7, pp. 1–14, 2017 (cited on pages - 14, 33).

[94] D. Rudd, C. Lopez-Mariscal, M. Summers, A. Shahvisi, J. Gutiérrez-Vega, and D. McGloin, "Fiber based optical trapping of aerosols," *Optics express*, vol. 16, pp. 14 550–14 560, 2008 (cited on page - 14).

[95] M. Horstmann, K. Probst, and C. Fallnich, "Towards an integrated optical single aerosol particle lab," *Lab Chip*, vol. 12, pp. 295–301, 2012 (cited on page - 15).

[96] M. Horstmann, K. Probst, and C. Fallnich, "An integrated fiber-based optical trap for single airborne particles," *Applied Physics B*, vol. 103, pp. 35–39, 2011 (cited on page - 15).

[97] J.-B. Decombe, S. K. Mondal, D. Kumbhakar, S. S. Pal, and J. Fick, "Single and multiple microparticle trapping using non-gaussian beams from optical fiber nanoantennas," *IEEE J Sel Top Quantum Electron*, vol. 21, pp. 247–252, 2014 (cited on page - 16).

[98] G. Leménager, M. Thiriet, F. Pourcin, K. Lahlil, F. Valdivia-Valero, G. C. Des Francs, T. Gacoin, and J. Fick, "Size-dependent trapping behavior and optical emission study of $NaYF_4$ nanorods in optical fiber tip tweezers," *Opt. Express*, vol. 26, pp. 32 156–32 167, 2018 (cited on pages - 16, 69).

[99] D. R. Burnham, "Microscopic applications of holographic beam shaping and studies of optically trapped aerosols," Ph.D. dissertation, University of St Andrews, 2009 (cited on pages - 17, 22).

[100] R. Jones, H. M. Pollock, J. A. S. Cleaver, and C. S. Hodges, "Adhesion forces between glass and silicon surfaces in air studied by afm: effects of relative humidity, particle size, roughness, and surface treatment," *Langmuir*, vol. 18, pp. 8045–8055, 2002 (cited on page - 17).

[101] C. T. Rueden, J. Schindelin, M. C. Hiner, B. E. DeZonia, A. E. Walter, E. T. Arena, and K. W. Eliceiri, "ImageJ2 : Imagej for the next generation of scientific image data," *BMC Bioinformatics*, vol. 18, p. 529, 2017 (cited on page - 20).

[102] S. Enterprises, *Scilab: Free and open source software for numerical computation*, Scilab Enterprises, Orsay, France, 2012 (cited on page - 20).

[103] J. Fick, "Out-of-equilibrium force measurements of dual-fiber optical tweezers," *Opt lett*, vol. 41, pp. 5716–5719, 2016 (cited on pages - 23, 43).

[104] J.-B. Decombe, J. Bryche, J. Motte, J. Chevrier, S. Huant, and J. Fick, "Transmission and reflection characteristics of metal-coated optical fiber tip pairs," *Applied optics*, vol. 52, pp. 6620–6625, 2013 (cited on pages - 25, 28).

[105] J.-B. Decombe, W. Schwartz, C. Villard, H. Guillou, J. Chevrier, S. Huant, and J. Fick, "Living cell imaging by far-field fibered interference scanning optical microscopy," *Opt. Express*, vol. 19, pp. 2702–2710, 2011 (cited on page - 28).

[106] N. Chevalier, Y. Sonnefraud, J. Motte, S. Huant, and K. Karrai, "Aperture-size-controlled optical fiber tips for high-resolution optical microscopy," *Rev. Scientific Instrum.*, vol. 77, p. 063 704, 2006 (cited on pages - 28, 29).

[107] R. Stöckle, C. Fokas, V. Deckert, R. Zenobi, B. Sick, B. Hecht, and U. P. Wild, "High-quality near-field optical probes by tube etching," *App. Phys. Lett.*, vol. 75, pp. 160–162, 1999 (cited on pages - 28, 29).

[108] K. Vairagi, R. A. Minz, S. Kaur, D. Kumbhakar, S. Paul, U. Tiwari, R. K. Sinha, J. Fick, and S. K. Mondal, "Deep seated negative axicon in selective optical fiber tip and collimated bessel beam," *IEEE Photonic. Tech. L.*, vol. 29, pp. 786–789, 2017 (cited on pages - 30, 31).

[109] J. Durnin, J. J. Miceli, and J. H. Eberly, "Diffraction-free beams," *Phys. Rev. Lett.*, vol. 58, pp. 1499–1501, 1987 (cited on page - 30).

[110] R. Kanawade, A. Kumar, D. Pawar, K. Vairagi, D. Late, S. Sarkar, R. K. Sinha, and S. Mondal, "Negative axicon tip-based fiber optic interferometer cavity sensor for volatile gas sensing," *Opt. express*, vol. 27, pp. 7277–7290, 2019 (cited on page - 30).

[111] P. Gupta, K. Vairagi, U. Tiwari, A. Pandey, and S. Mondal, "Application of bessel beam from deep seated negative axicon in optical coherence tomography of tissue structure," in *Optical Coherence Tomography and Coherence Domain Optical Methods in Biomedicine XXIII*, vol. 10867, 2019, 108672N (cited on page - 31).

[112] S. K. Mondal, A. Mitra, N. Singh, S. Sarkar, and P. Kapur, "Optical fiber nanoprobe preparation for near-field optical microscopy by chemical etching under surface tension and capillary action," *Opt. express*, vol. 17, pp. 19 470–19 475, 2009 (cited on pages - 31, 32).

[113] A. Kumar, "Characterization of fiber tips and optical trapping," M.S. thesis, Université de Bourgogne, Dijon, France, 2017 (cited on page - 31).

[114] J.-B. Decombe, S. K. Mondal, D. Kumbhakar, S. S. Pal, and J. Fick, "Single and multiple microparticle trapping using non-gaussian beams from optical fiber nanoantennas," *IEEE J. Sel. Top. Quantum Electron*, vol. 21, pp. 247–252, 2014 (cited on pages - 32, 57).

[115] R. A. Minz, U. Tiwari, A. Kumar, S. Nic Chormaic, K. Lahlil, T. Gacoin, S. K. Mondol, and J. Fick, "Trapping of rare earth-doped nanorods using quasi bessel beam optical fiber tweezers," Manuscript in progress, 2020 (cited on pages - 32, 33).

[116] S. S. Pal, S. K. Mondal, P. P. Bajpai, and P. Kapur, "Optical fiber tip for field-enhanced second harmonic generation," *Opt. Lett.*, vol. 37, pp. 4017–4019, 2012 (cited on page - 32).

[117] S. K. Mondal, S. S. Pal, D. Kumbhakar, U. Tiwari, and R. Bhatnagar, "Evanescent wave assisted nanomaterial coating," *Appl. Opt.*, vol. 52, pp. 5455–5459, 2013 (cited on page - 32).

[118] T. Gissibl, S. Wagner, J. Sykora, M. Schmid, and H. Giessen, "Refractive index measurements of photo-resists for three-dimensional direct laser writing," *Opt. Mater. Express*, vol. 7, pp. 2293–2298, 2017 (cited on page - 33).

[119] K. Berg-Sørensen and H. Flyvbjerg, "Power spectrum analysis for optical tweezers," *Rev. Sci. Instrum.*, vol. 75, pp. 594–612, 2004 (cited on pages - 37, 39).

[120] E. N. Glytsis, *Introduction to gaussian beams*, Lectures notes, National Technical Univerity of Athens, Greece, 2020 (cited on page - 49).

[121] K. R. Bajgiran, J. A. Dorman, and A. T. Melvin, "Dipole-modulated downconversion nanoparticles as label-free biological sensors," *ACS Sensors*, vol. 5, pp. 29–33, 2020 (cited on page - 62).

[122] G. Chen, C. Yang, and P. N. Prasad, "Nanophotonics and nanochemistry: Controlling the excitation dynamics for frequency up- and down-conversion in lanthanide-doped nanoparticles," *Acc. Chem. Res*, vol. 46, pp. 1474–1486, 2013 (cited on page - 62).

[123] J. Kim, R. Chacon-Heiva, A. Leray, G. Colas des Francs, Z. Wang, K. Lahlil, J. Kim, and T. Gacoin, "Measuring 3D orientation of nanocrystals via polarized luminescence of rare-earth dopants," Manuscript in progress, 2020 (cited on pages - 62–64, 73, 81).

[124] J. Kim, S. Michelin, M. Hilbers, L. Martinelli, E. Chaudan, G. Amselem, E. Fradet, J.-P. Boilot, A. M. Brouwer, C. N. Baroud, *et al.*, "Monitoring the orientation of rare-earth-doped nanorods for flow shear tomography," *Nature Nanotechnol*, vol. 12, p. 914, 2017 (cited on pages - 62, 70, 73, 79).

[125] M. Kasperczyk, S. Person, D. Ananias, L. D. Carlos, and L. Novotny, "Excitation of magnetic dipole transitions at optical frequencies," *Phy Rev Lett*, vol. 114, p. 163 903, 2015 (cited on page - 62).

[126] A. Parchur and R. Ningthoujam, "Behaviour of electric and magnetic dipole transitions of Eu^{3+}, $^5D_0 \rightarrow {}^7F_0$ and Eu–O charge transfer band in Li^+ co-doped YPO_4:Eu^{3+}," *RSC Advances*, vol. 2, pp. 10 859–10 868, 2012 (cited on page - 62).

[127] K. Ge, W. Sun, S. Zhang, S. Wang, G. Jia, C. Zhang, and J. Zhang, "Europium-doped $NaYF_4$ nanoparticles cause the necrosis of primary mouse bone marrow stromal cells through lysosome damage," *RSC Adv.*, vol. 6, pp. 21 725–21 734, 26 2016 (cited on page - 62).

[128] A. Aebischer, M. Hostettler, J. Hauser, K. Krämer, T. Weber, H. U. Güdel, and H.-B. Bürgi, "Structural and spectroscopic characterization of active sites in a family of light-emitting sodium lanthanide tetrafluorides," *Angew Chem Int Ed*, vol. 45, no. 17, pp. 2802–2806, 2006 (cited on page - 62).

[129] C. Liu, Y. Hou, and M. Gao, "Are rare-earth nanoparticles suitable for in vivo applications?" *Adv Mater*, vol. 26, pp. 6922–6932, 2014 (cited on page - 62).

[130] D. Tu, Y. Liu, H. Zhu, R. Li, L. Liu, and X. Chen, "Breakdown of crystallographic site symmetry in lanthanide-doped $NaYF_4$ crystals," *Angew. Chem. In. Ed.*, vol. 52, pp. 1128–1133, 2013 (cited on page - 62).

[131] J. Kim, unpublished thesis, Ph.D. dissertation, Ecole Polytechnique, Palaiseau, France, 2017-20 (cited on pages - 62, 63).

[132] X. Wang, J. Zhuang, Q. Peng, and Y. Li, "A general strategy for nanocrystal synthesis," *Nature*, vol. 437, pp. 121–124, 2005 (cited on page - 63).

[133] L. Wang and Y. Li, "$Na(Y_{1.5}Na_{0.5})F_6$ single-crystal nanorods as multicolor luminescent materials," *Nano letters*, vol. 6, pp. 1645–1649, 2006 (cited on page - 63).

[134] O. Marago, P. Jones, F. Bonaccorso, V. Scardaci, P. Gucciardi, A. Rozhin, and A. Ferrari, "Femtonewton force sensing with optically trapped nanotubes," *Nano Lett.*, vol. 8, pp. 3211–3216, 2008 (cited on page - 68).

[135] P. J. Reece, W. J. Toe, F. Wang, S. Paiman, Q. Gao, H. H. Tan, and C. Jagadish, "Characterization of semiconductor nanowires using optical tweezers," *Nano Lett.*, vol. 11, pp. 2375–2381, 2011 (cited on page - 68).

[136] P. B. Roder, B. E. Smith, E. J. Davis, and P. J. Pauzauskie, "Photothermal heating of nanowires," *J. Phys. Chem. C*, vol. 118, pp. 1407–1416, 2014 (cited on page - 68).

[137] F. T. Rabouw, P. T. Prins, and D. J. Norris, "Europium-doped $NaYF_4$ nanocrystals as probes for the electric and magnetic local density of optical states throughout the visible spectral range," *Nano Lett.*, vol. 16, pp. 7254–7260, 2016 (cited on pages - 69, 70, 83, 92).

[138] R. Chacon-Heiva, A. Leray, J. Kim, K. Lahlil, S. Mathew, A. Bouhelier, J. Kim, T. Gacoin, and G. Colas des Francs, "Measuring the magnetic dipole transition of single nanorods by fourier microscopy," Manuscript in progress, 2020 (cited on pages - 73, 79, 81).

[139] M. Y. Berezin and S. Achilefu, "Fluorescence lifetime measurements and biological imaging," *Chem. Rev.*, vol. 110, pp. 2641–2684, 2010 (cited on page - 81).

[140] G. Jia and P. A. Tanner", "Energy transfer between UO_2^{2+} and Eu^{3+} in β-$NaYF_4$," *J. Alloys Compd.*, vol. 471, pp. 557–560, 2009 (cited on page - 81).

[141] N. Yaiphaba, R. Ningthoujam, N. S. Singh, R. Vatsa, N. R. Singh, S. Dhara, N. Misra, and R. Tewari, "Luminescence, lifetime, and quantum yield studies of redispersible Eu^{3+}-doped $GdPO_4$ crystalline nanoneedles: Core-shell and concentration effects," *J. Appl. Phys.*, vol. 107, p. 034 301, 2010 (cited on page - 81).

[142] K. Manthiram and A. P. Alivisatos, "Tunable localized surface plasmon resonances in tungsten oxide nanocrystals," *Journal of the American Chemical Society*, vol. 134, pp. 3995–3998, 2012 (cited on page - 84).

[143] Y. Guo, X. Quan, N. Lu, H. Zhao, and S. Chen, "High photocatalytic capability of self-assembled nanoporous WO3 with preferential orientation of 002 planes," *Environ. Sci. Technol.*, vol. 41, pp. 4422–4427, 2007 (cited on page - 84).

[144] S. L. Gibbs, C. M. Staller, and D. J. Milliron, "Surface depletion layers in plasmonic metal oxide nanocrystals," *Acc. Chem. Res.*, vol. 52, pp. 2516–2524, 2019 (cited on page - 84).

[145] F. Shi, J. Liu, X. Dong, Q. Xu, J. Luo, and H. Ma, "Hydrothermal synthesis of $CsxWO_3$ and the effects of N2 annealing on its microstructure and heat shielding properties," *J. of Mater. Sci. Technol*, vol. 30, pp. 342–346, 2014 (cited on page - 84).

[146] J. X. Liu, X. J. Wang, F. Shi, Z. J. Peng, J. Y. Luo, Q. Xu, and P. C. Du, "Hydrothermal synthesis of cesium tungsten bronze and its heat insulation properties," vol. 531, 2012, pp. 235–239 (cited on page - 84).

[147] G. Liu, F. Kong, R. Li, *et al.*, "Novel synthesis of 0D, 1D and 2D nano-$CsxWO_3$ and their tunable optical-thermal response performance," *J. Mater. Chem. C*, 2020 (cited on page - 84).

[148] Y. Cheref, "Plasmonic oxide nanocrystals for near-infrared devices," unpublished thesis, Ph.D. dissertation, Ecole Polytechnique, Palaiseau, France, 2017-20 (cited on pages - 84, 85).

[149] A. Enferadi-Kerenkan, A. S. Ello, and T.-O. Do, "Synthesis, organo-functionalization, and catalytic properties of tungsten oxide nanoparticles as heterogeneous catalyst for oxidative cleavage of oleic acid as a model fatty acid into diacids," *Ind. Eng. Chem. Res.*, vol. 56, pp. 10 639–10 647, 2017 (cited on page - 84).

[150] P.-S. Hu, N. Tomasovicova, H.-J. Chou, M.-C. Li, M. Vojtko, K. Zakutanska, J. Majorosova, S.-J. Chen, and P. Kopcansky, "Hyperthermia induced by near-infrared laser-irradiated csWO$_3$ nanoparticles disintegrates preformed lysozyme amyloid fibrils," *Nanomaterials*, vol. 10, p. 442, 2020 (cited on pages - 84, 92).

[151] A. Bertoncini, S. P. Laptenok, V. P. Rajamanickam, and C. Liberale, "3D nanoprinted high NA ultra-compact catadioptric lens for efficient collection in forward detection configuration microscopy," in *The European Conference on Lasers and Electro-Optics*, 2019, cl_2_5 (cited on page - 92).

[152] K. Weber, F. Hütt, S. Thiele, T. Gissibl, A. Herkommer, and H. Giessen, "Single mode fiber based delivery of oam light by 3D direct laser writing," *Opt. Express*, vol. 25, pp. 19 672–19 679, 2017 (cited on page - 92).

[153] Y. Ma, G. Rui, B. Gu, and Y. Cui, "Trapping and manipulation of nanoparticles using multifocal optical vortex metalens," *Sci. Rep.*, vol. 7, pp. 1–9, 2017 (cited on page - 92).

[154] L. W. Russell, S. G. Ralph, K. Wittick, J.-P. Tetienne, D. A. Simpson, and P. J. Reece, "Manipulating the quantum coherence of optically trapped nanodiamonds," *ACS Photonics*, vol. 5, pp. 4491–4496, 2018 (cited on page - 92).

Spectroscopic characterization of optically trapped nanoparticles

Abstract

Since the past few decades, optical tweezers have emerged as a tool for contactless trapping and manipulating nanoparticles. The optical trapping using optical fibers is a complementary and versatile approach that allows easy integration of other experimental techniques such as spectroscopy. In this context, we have studied the optical trapping of nanoparticles using two distinct fiber tweezers setups in air and water, respectively. The particle trapping in air has been observed as challenging, using a diverging beam produced by nanostructured fibers, since it could not pull the particles towards the center of the light beam. In contrast, the particle trapping in water has appeared to be very efficient, which has been realized using two counter-facing tapered fiber tips. To further enhance the trapping efficiency and flexibility of this setup, we have implemented two different 3D printed fibers: Fresnel lens and total internal reflection (TIR)-probe fibers. This experimental setup has been used for optical trapping and spectroscopic characterization of europium-doped nanorods by employing two different fiber types. Firstly, we have studied the stable nanorod trapping in tip-contact using a diverging beam producing beam fiber. Secondly, the efficient nanorod trapping has been realized using the counter-propagating converging beams of two Fresnel lens fibers at about 200 µm distance between these fibers. These nanorod trapping experiments have been exploited for measuring the direction and polarization-resolved Eu^{3+} photoluminescence emission. A polarization-dependent emission has been studied in a perpendicular direction with respect to the nanorod axis, which allowed the determination of σ and π-polarization of emission electric and magnetic dipole transitions. We have precisely determined the orientation of optically trapped nanorods using trapping videos and spectroscopic means. It further motivates us for faster spectroscopic analysis of these nanorods from the perspective of microrheologic experiments. In the last experiment, we have trapped plasmonic oxide nanoparticles in the aspect of studying their light absorption feature for bio-sensing applications.

Keywords: Optical tweezers, fiber optics, Eu^{3+}-doped nanorods, spectroscopy, photoluminescence.

Résumé

Depuis quelques décennies, les pinces optiques sont devenues un outil de piégeage et de manipulation sans contact de nanoparticules. Le piégeage optique à l'aide de fibres optiques est une approche complémentaire et polyvalente qui permet l’intégration aisée d'autres techniques expérimentales telles que la spectroscopie. Dans ce contexte, nous avons étudié le piégeage optique de nanoparticules à l'aide de deux configurations de pinces distinctes dans l'air et l'eau, respectivement. Le piégeage des particules dans l'air a été observé comme difficile, en utilisant un faisceau divergent produit par des fibres nanostructurées, car il ne pouvait pas attirer les particules vers le centre du faisceau lumineux. En revanche, le piégeage des particules dans l'eau s'est avéré très efficace, ce qui a été réalisé en utilisant deux pointes de fibres coniques opposées. Pour améliorer encore l'efficacité et la flexibilité de piégeage de cette configuration, nous avons implémenté deux fibres imprimées en 3D différentes: une lentille de Fresnel et des fibres à réflexion interne totale (TIR). Cette configuration expérimentale a été utilisée pour le piégeage optique et la caractérisation spectroscopique de nanobâtonnets dopés à l'europium en employant deux types de fibres différents. Dans un premier temps, nous avons étudié le piégeage stable de nanobâtonnts en contact vaec la pointe à l'aide d'un faisceau divergent. Deuxièmement, le piégeage efficace de nanbâtonnets a été réalisé en utilisant les faisceaux convergents à contre-propagation de deux fibres à lentille de Fresnel à une distance d'environ 200 µm entre ces fibres. Ces expériences de piégeage de nanorod ont été exploitées pour mesurer la direction et l'émission de photoluminescence Eu^{3+} résolue en polarisation. L’émission dépendant de la polarisation a été étudiée dans une direction perpendiculaire par rapport à l'axe de la nanobâtonnet, ce qui a permis de déterminer la polarisation σ et π des transitions dipolaires électriques et magnétiques. Nous avons déterminé avec précision l'orientation des nanorbâtonnets piégés optiquement à l'aide de vidéos de piégeage et de moyens spectroscopiques. Cela nous motive en outre pour une analyse spectroscopique plus rapide de ces nanobâtonnets du point de vue des expériences microrhéologiques. Dans la dernière expérience, nous avons piégé des nanoparticules d'oxyde plasmonique dans le but d'étudier leur d'absorption optique pour des applications de bio-détection.